

MULTI-FIDELITY AND MULTI-DISCIPLINARY DESIGN
OPTIMIZATION OF SUPERSONIC BUSINESS JETS

A DISSERTATION

SUBMITTED TO THE DEPARTMENT OF AERONAUTICS AND ASTRONAUTICS

AND THE COMMITTEE ON GRADUATE STUDIES

OF STANFORD UNIVERSITY

IN PARTIAL FULFILLMENT OF THE REQUIREMENTS

FOR THE DEGREE OF

DOCTOR OF PHILOSOPHY

Seongim Choi

December 2005

© Copyright by Seongim Choi 2006
All Rights Reserved

I certify that I have read this dissertation and that, in my opinion, it is fully adequate in scope and quality as a dissertation for the degree of Doctor of Philosophy.

Juan J. Alonso
(Principal Advisor)

I certify that I have read this dissertation and that, in my opinion, it is fully adequate in scope and quality as a dissertation for the degree of Doctor of Philosophy.

Ilan M. Kroo

I certify that I have read this dissertation and that, in my opinion, it is fully adequate in scope and quality as a dissertation for the degree of Doctor of Philosophy.

Antony Jameson

Approved for the University Committee on Graduate Studies.

Abstract

Supersonic jets have been drawing great attention after the end of service for the Concorde was announced on April of 2003. It is believed, however, that civilian supersonic aircraft may make a viable return in the business jet market. This thesis focuses on the design optimization of feasible supersonic business jet configurations. Preliminary design techniques for mitigation of ground sonic boom are investigated while ensuring that all relevant disciplinary constraints are satisfied (including aerodynamic performance, propulsion, stability & control and structures.) In order to achieve reasonable confidence in the resulting designs, high-fidelity simulations are required, making the entire design process both expensive and complex. In order to minimize the computational cost, surrogate / approximate models are constructed using a hierarchy of different fidelity analysis tools including PASS, A502/Panair and Euler/NS codes. Direct search methods such as Genetic Algorithms (GAs) and a non-linear SIMPLEX are employed to find optimum designs in searches of large and noisy design spaces. A local gradient-based search method can be combined with these global search methods for small modifications of candidate optimum designs. The Mesh Adaptive Direct Search (MADS) method can also be used to explore the design space using a solution-adaptive grid refinement approach. These hybrid approaches, both in search methodology and surrogate model construction, are shown to result in designs with reductions in sonic boom and improved aerodynamic performance.

Dedicated to my family
Stanford, California, December 2005

Acknowledgment

My graduate student life has been a rather long but enjoyable journey, and I wish to complete with the following remarks. First of all, I would like to give my warmest gratitude to Professor Juan Alonso. His patient guidance was an immense help for me during the course of my doctoral studies. He himself is a model of a hard-working scholar and a cheerful colleague.

I was also very happy and fortunate to work with Professor Ilan Kroo who has been a tremendous help in our optimization work. He gave us practical insight into aircraft design and much inspiration. He also allowed me to use the software PASS, which helped make our design feasible. I am also indebted to Professor Antony Jameson for letting me use some of the many high-fidelity analysis tools that have originated from his research over the past decades. With the help of these tools, my design work developed from conceptual and preliminary to detailed design. I express my gratitude to Mathias Wintzer for running PASS optimization cases for me despite his busy schedule, and to Dr. Edwin van der Weide for providing the flow solver AirplanePlus.

I have met such great and amazing people in Stanford: Friday beer friends and labmates from the Aerospace Computing Lab & the Aerospace Design Lab, the Korean mafia in Aero/Astro, and the Bongo club friends. My friends in Korea were also an endless source of energy over the years and are precious pieces of my memory. Without all of these people, my life at Stanford would have been far less enjoyable.

I consider myself lucky to have met Dr. Young Yu and Dr. Chee Tung from NASA Ames Research Center, who both have been very supportive and caring. I owe so much to them and I will try to be worthy of their help and concern.

Finally I would like to express my sincerest love for my family. My mother and father have been my managers and sponsors throughout my life, and I wish to dedicate this thesis to them as a small token of gratitude. I wish from my heart that they will always be with me, as happy and healthy as ever. My brothers and sister-in-law, Dongzin, Moonsuk and Hyejin, have always been my best friends, and I'd like to also thank my lovely nephew and niece, Seohyun and Yehyun. I believe this period now is opening the door to another wonderful future world and I'm marching with all of them.

Contents

Abstract	iv
Acknowledgment	vi
1 Introduction	1
1.1 Civil Supersonic Flight and Sonic Boom	1
1.1.1 Sonic Boom Phenomenon and Environmental Effects	2
1.1.2 Efforts on Sonic Boom Minimization	3
1.2 Multi-Disciplinary Optimization	4
1.2.1 Problem Specification	5
1.2.2 Importance of Mission Constraints and Program for Aircraft Synthesis Study (PASS)	5
1.2.3 Variable-Fidelity Aerodynamic Analysis Tools	7
1.2.4 Multi-Fidelity Response Surface	9
1.2.5 Two-Level Optimization: Global and Local Optimization	11
1.3 Organization of Thesis	12
2 Sonic Boom	13
2.1 Sonic Boom Analysis	13
2.1.1 Formation of Sonic Boom: Boom Carpets	13
2.1.2 Brief Historical Review of Sonic Boom Analysis	15
2.2 F-function Method	17
2.2.1 Whitham F-function	17
2.2.2 Propagation Through the Real Atmosphere	19

2.3	Waveform Parameter Method	22
2.3.1	Waveform Parameters	22
2.3.2	Linear, Nonplanar Wave	23
2.3.3	Nonlinear, Planar Wave	23
2.3.4	Nonlinear, Nonplanar Wave	24
2.4	Sonic Boom Minimization	25
2.5	Sonic Boom Noise Metrics	25
2.5.1	Weighting Networks	26
2.5.2	Shock Rise Time and Turbulence in Atmosphere	28
3	Automated Boom/Performance Analysis	31
3.1	BOOM-UA	33
3.1.1	Geometry Representation Using CAD/Capri/Aerosurf	35
3.1.2	Unstructured Tetrahedral Mesh Generation	36
3.1.3	Unstructured Flow Solver and Solution Approach: AirplanePlus	38
3.1.4	Solution-adaptive Mesh Refinement	39
3.1.5	Near-field Pressure Extraction	43
3.2	Validation: Comparison of Wind-tunnel Data	45
3.2.1	Configurations of Interest	45
3.2.2	Experimental Conditions	46
3.2.3	Solvers and Flow Conditions	48
3.2.4	Results	48
3.2.5	Comparison of Near-field Pressures with Experimental Data .	50
3.2.6	Ground Boom Signature and Weighted Sound Levels	52
4	Variable-Fidelity Aerodynamic Analysis Tools	63
4.1	PASS	66
4.1.1	Geometry	67
4.1.2	Drag Estimation	67
4.1.3	Weights and CG	67
4.1.4	Static Stability and Trim	68
4.1.5	Propulsion	68

4.1.6	Low-Speed Analysis	68
4.1.7	High-Lift Systems	68
4.1.8	Loads	69
4.1.9	Operating Cost	69
4.1.10	Mission Analysis	69
4.1.11	Optimization	70
4.1.12	Design Configurations	70
4.2	Linear Panel Method: A502/Panair	70
4.3	Comparison of A502 and AirplanePlus Results	71
4.3.1	Comparison of aerodynamic performance	72
4.3.2	Comparison of results for ground boom loudness	79
4.4	SYN87-SB and SYN107-MB	82
4.4.1	Validation with Unstructured Code	85
5	Response Surface and Optimization	89
5.1	Characteristics of Design Space	90
5.2	Approximation Methods	91
5.2.1	Sampling technique	91
5.2.2	Least-squares regression response surface modeling	93
5.2.3	Kriging Model	94
5.2.4	Neural Network	96
5.3	Multi-Fidelity Response Surface	102
5.3.1	Number of Sample Points	106
5.4	Gradient-free Optimizer	106
5.4.1	Nonlinear SIMPLEX Method	108
5.4.2	Genetic Algorithms	108
5.5	Gradient-based Optimizer	110
5.5.1	Finite difference method	111
5.5.2	Complex-step method	113
5.5.3	Adjoint method	113

5.5.4	NPSOL Sequential Quadratic Programming Optimizer with Adjoint Solver	114
6	Optimization Results	115
6.1	Baseline Configuration	116
6.1.1	Standard-PASS Optimization	116
6.1.2	Design Variables	117
6.1.3	Mission Profile	121
6.2	Design I	126
6.2.1	Multi-Fidelity Response Surface	127
6.2.2	Minimum Boom Loudness (dBA) Optimization : Modified PASS Optimization	130
6.2.3	Minimum TOGW Optimization: Modified PASS Optimization	132
6.2.4	High-Fidelity Validation of Optimization Results	133
6.3	Design II	139
6.3.1	Modifications to Baseline Configuration	142
6.3.2	Multi-Fidelity Response Surface	144
6.3.3	Minimum MTOGW Optimization: Gradient-Free Global Optimization Using Modified PASS	146
6.3.4	High-Fidelity Validation of Optimization Results	147
6.3.5	Minimum Drag Optimization: Adjoint Local Optimization . .	151
7	Conclusions and Future Work	154
7.1	Future Work	155
	Bibliography	157

List of Tables

1.1	Sonic boom overpressure from several vehicles	2
3.1	Number of mesh nodes through all the adaption cycles	49
3.2	C-weighted sound level and perceived loudness from experimental data. Complete configuration.	53
3.3	C-weighted sound level and perceived loudness from experimental data. Configuration without nacelles.	54
3.4	C-weighted sound level and perceived loudness from experimental data. Configuration without nacelles and tail.	54
3.5	Error in C-weighted sound level and perceived loudness between ex- periment and computation. Complete configuration.	54
3.6	Error in C-weighted sound level and perceived loudness between ex- periment and computation. Configuration without nacelles.	54
3.7	Error in C-weighted sound level and perceived loudness between ex- periment and computation. Configuration without nacelles and tail.	55
4.1	Comparison of different fidelity analysis tools	64
4.2	Summary of geometric and performance design variables for PASS- optimized configuration	73
4.3	Some mission constraints for PASS-optimization	73
4.4	Summary of geometries and flight condition for boom baseline	74
4.5	Comparison of values of C_D for varying $Mach_{\perp}$ for full configuration	79

5.1	Accuracy of VARPRO and quadratic response surface given by the sum of the errors in different output functionals	101
5.2	Error in prediction of response between VARPRO and Quadratic fit .	102
6.1	Optimization problem definition for Designs I and II.	115
6.2	Input and Output parameters for PASS mission analysis	118
6.3	Geometric design parameters for the baseline configuration.	119
6.4	Some of mission constraints goal (details are in Table 6.5.)	119
6.5	Mission analysis values for the baseline and bounds for optimization runs.	120
6.6	Bounds for geometric design variables and for sample distribution for response surface generation.	123
6.7	Results of PASS + Euler surface analysis of the baseline configuration.	126
6.8	Results of PASS + response surface optimization for boom minimization.	132
6.9	Results of PASS + response surface optimization for boom-constrained optimization with small manual modifications.	135
6.10	Results of PASS + response surface optimization for TOGW optimization.	139
6.11	Results of validation of minimum boom and minimum TOGW designs.	139
6.12	Comparison of mission profile for modified baseline (analyzed by PASS + Euler)	143
6.13	Results of PASS + response surface optimization for boom minimization.	147
6.14	Comparison of performance between baseline and optimized configuration	153

List of Figures

1.1	Schematic of boom propagation	3
1.2	N ground wave propagated from SR-71. From [2]	4
1.3	Comparison of shape: baseline(bottom) and optimized(top)	7
1.4	Comparisons of boom performance between baseline and optimized configuration.	8
2.1	Ground boom phenomena. From [26]	14
2.2	Mach cone and ray cone in supersonic flight. From [26]	15
2.3	Evolution and steepening of sonic boom signature. From [26]	20
2.4	Rectangular ray tube outlined by four rays. From [26]	21
2.5	Frequency response characteristics of various weighting networks [48].	27
2.6	Ground boom signature with/without rise time modification.	30
3.1	Schematic of the aerodynamic analysis tool, BOOM-UA	33
3.2	Geometry representation by parametric, CAD-interfaced AEROSURF	35
3.3	Surface mesh for NASA SBJ configuration	38
3.4	Mesh adaption process	41
3.5	Schematic of Sonic Boom Minimization Setup with Nomenclature. . .	43
3.6	Three-View drawing of NASA SBJ configuration.	46
3.7	View of the model mounted in the wind tunnel. From [72]	47
3.8	Surface pressure distributions: complete configuration SBJ.	56
3.9	Surface pressure distributions: SBJ without nacelles.	56
3.10	Surface pressure distributions: SBJ without nacelles and empennage.	56

3.11	Near-field pressure distributions for all adaption cycles. Complete configuration.	57
3.12	Near-field pressure distributions for all adaption cycles. Configuration without nacelles.	57
3.13	Near-field pressure distributions for all adaption cycles. Configuration without nacelles and tail.	58
3.14	Comparison of near-field pressure with experiments. Complete configuration.	59
3.15	Comparison of near-field pressure with experiments. Configuration without nacelles.	59
3.16	Comparison of near-field pressure with experiments. Configuration without nacelles and tail.	60
3.17	Plot of near-field pressure distributions along symmetry plane.	60
3.18	Ground boom comparisons. Complete configuration.	61
3.19	Ground boom comparisons. Configuration without nacelles.	61
3.20	Ground boom comparisons. Configuration without nacelles and tail.	62
4.1	Different views of the configuration within PASS.	66
4.2	Surface grids for wing-body standard-PASS optimized configuration	75
4.3	Comparison of drag polars for standard-PASS optimized wing-body configuration between A502 and AirplanePlus	76
4.4	Surface grids for the standard-PASS optimized configuration	77
4.5	Comparison of drag polars for full configuration between A502 and AirplanePlus	78
4.6	Comparison of values of C_D for varying $Mach_{\perp}$ for full configuration	79
4.7	Surface grids for the boom baseline configuration	81
4.8	Symmetry plane mesh before and after solution-adaptive refinement	82
4.9	Comparison of near-field pressure and ground boom signature between A502 and AirplanePlus when $AOA = 3^{\circ}$	83
4.10	Comparison of near-field pressure and ground boom signature between A502 and AirplanePlus when $C_L=0.1$	83

4.11	Near-field pressure comparisons between A502/Panair and the Euler computations for increasing free stream Mach numbers and corresponding normal Mach numbers.	84
4.12	Comparison of grid between unstructural and structural system . . .	87
4.13	Comparison of drag polars between SYN107-MB and AirplanePlus . .	88
5.1	Two dimensional design spaces analyzed by FLO107-MB	92
5.2	The schematic of Neural Network system	97
5.3	The schematic of Neural Network system for VARPRO	99
5.4	The effect of number of the samples on the relative error	107
5.5	Pareto front from multi-objective optimization without constraints. From [92]	111
5.6	Pareto front from multi-objective optimization with simple constraints. From [89]	112
6.1	Three-view drawing of baseline PASS-optimized configuration	121
6.2	Summary of baseline configuration.	122
6.3	Mission profile (analyzed by standard PASS) of baseline configuration	124
6.4	Design variables for wing planform	125
6.5	Database of A502/Panair results.Green dots: A502-analyzed points. Red dots: A502-analyzed points with large errors.	128
6.6	A502/Panair and CE results. Green dots: A502-analyzed points. Red dots: A502-analyzed points with large errors. Blue dots: CE-reanalyzed points	129
6.7	CE and FE results: Blue dots: CE-analyzed points. Yellow dots: CE-analyzed points with large errors. Magenta dots: FE-reanalyzed points	129
6.8	Summary of boom optimized configuration (Design I).	131
6.9	Mission profile (analyzed by standard PASS+RS) of boom optimized configuration (Design I)	133
6.10	Euler comparison for optimized and baseline designs.	134
6.11	Convergence history of boom constraint function.	135

6.12	Summary of boom optimized configuration with small manual modifications (Design I).	136
6.13	Summary of TOGW optimized configuration (Design I).	137
6.14	Mission profile (analyzed by standard PASS+RS) of TOGW optimized configuration (Design I)	138
6.15	Inviscid drag coefficients at various wing tip twist angles.	143
6.16	Database of PASS (green) and A502/Panair (red) results.	145
6.17	Database of PASS (green), A502/Panair (red) and FE (blue) results.	146
6.18	Summary of optimized configuration (Design II).	148
6.19	Mission profile (analyzed by standard PASS+RS) of optimized configuration (Design II)	149
6.20	Comparison of shapes of baseline and optimized configuration (blue:baseline, red:optimized).	150

Chapter 1

Introduction

1.1 Civil Supersonic Flight and Sonic Boom

The Concorde was both a beautiful plane with its renowned looks and a technological marvel. It represented a big improvement in flight technology by cutting hours off transatlantic trips. Unfortunately it was never a commercial success. It carried one quarter of the passengers of a Boeing 747 but consumed twice the amount of fuel resulting in prohibitive ticket costs for most passengers. The other major problem was created by environmental concerns related to engine noise and sonic boom on the ground. The FAA noise regulation (FAR, part 36) does not allow supersonic flight over the populated land [1] and only several airports were equipped to accommodate the Concorde. These problems ended the three-decade-old supersonic service in October 2003. Furthermore, a successor to the Concorde has never been developed.

However the pursuit of civilian supersonic flight has never faded and the current market, industry and technology trends make the return of supersonic jets likely. It is currently believed that civilian supersonic aircraft may make a viable return only in the smaller business jet market. Aerion and SAI (Supersonic Aerospace International) unveiled two distinctive business jet designs at the National Business Aviation Association meeting on Oct. 2004. Gulfstream is also developing concepts for its own supersonic business jet. However all the key players are moving cautiously: a substantial time and money investment will be required. Moreover, somewhat relaxed

Vehicle	Mach number	Altitude (<i>ft</i>)	Sonic boom overpressure (psf)
SR-71	3	80,000	0.9
Concorde SST	2	52,000	1.94
F-104	1.93	48,000	0.8
Space shuttle	1.5	60,000 (landing)	1.25

Table 1.1: Sonic boom overpressure from several vehicles

noise regulations may also be needed.

1.1.1 Sonic Boom Phenomenon and Environmental Effects

Sonic boom is an acoustic phenomenon related to supersonic flight. A pressure disturbance is generated by the aircraft. This disturbance propagates through an atmosphere that has gradients in its properties corresponding to the variations in altitude. During the propagation the disturbance experiences nonlinear distortion and steepening, and ultimately coalesces into a well-known N-wave by the time it reaches the ground. The simple schematic of wave propagation and the classical N wave at the ground are shown in Figures 1.1 and 1.2 respectively: the bow shock created by the nose of the aircraft is followed by a linear expansion to a negative pressure and then by a second shock associated with the recompression at the tail of the configuration. Figure 1.2 shows the experimental measurement of ground boom propagated from an SR-71 flying at a freestream Mach number of 1.5 and a flight altitude of 48,000*ft*. Details of the sonic boom phenomenon are presented in Chapter 2. The strength of the sonic boom is usually measured in pounds per square foot of overpressure of the initial shock wave. This is the amount of the pressure increase above normal atmospheric pressure (2,116 psf/14.7 psi). The sonic boom signature has been one of the main reasons preventing the acceptance of supersonic flight over populated areas. The importance of minimizing the environmental impact cannot be understated. Recently there has been a wide range of studies about the human responses on the sonic boom and its effects on the environment. Details can be found in references [3, 26, 5]. Sonic boom measurements from different aircraft are compared in Table 1.1.

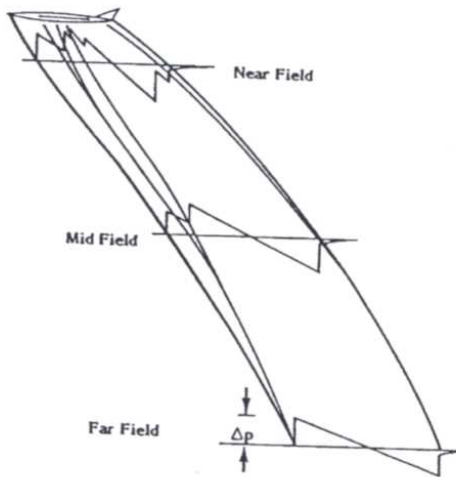


Figure 1.1: Schematic of boom propagation

1.1.2 Efforts on Sonic Boom Minimization

Sonic boom minimization efforts have concentrated mainly on shaping of the N-wave at the ground. From scaling laws based on Whitham's theory [7], it can be shown that longer, slender and lighter aircraft that have relatively small lifting surfaces can reduce the maximum overpressure significantly [13, 40, 7]. However, the resulting configurations are not practical considering the cabin size, limited aircraft weight, and fuel capacity. Jones [14, 15] suggested that a delta function-like behavior of near-field pressure signature is optimal regarding ground boom signature. McLean [13] was the first to point out that the boom from a real aircraft at typical flight conditions may not achieve far-field conditions (N-wave), and the ground boom may in fact really be the mid-field boom signature. He suggested that tailoring the shape of the mid-field signature could lead to results different from an N-wave that may be beneficial.

A significant achievement in sonic boom minimization was accomplished when George [45] combined Jones's delta function with an isentropic compression. The F-function of the delta function followed by a plateau resulted in a smaller shock at the ground compared to a pure delta function. George and Seebass [41, 42] developed a full theory for minimization of both front and rear shocks. It became a fundamental

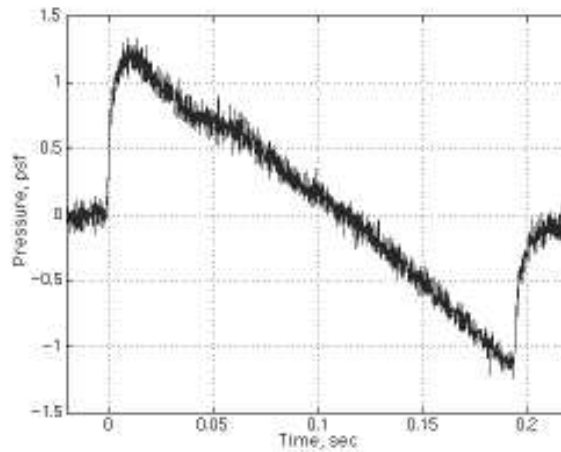


Figure 1.2: N ground wave propagated from SR-71. From [2]

theory for current and recent sonic boom research such as the NASA High Speed Civil Transport (HSCT) program, the DARPA Quiet Supersonic Platform (QSP) program and the F-5 Shaped Sonic Boom Demonstrator (SSBD) also sponsored by DARPA.

The fundamental strategy in our study in minimizing the sonic boom follows the conventional approach of shaping the boom signature by aerodynamic shape optimization (ASO). However, two fundamental differences exist: we will work directly with the shape of the aircraft (rather than its F -function) and we will use high-fidelity non-linear tools (instead of linearized theories) to account for effects that may have been missed by classical theory.

1.2 Multi-Disciplinary Optimization of Supersonic Business Jets

The purpose of this study is the multi-disciplinary shape and mission optimization of a supersonic design with careful consideration of both the strength of the ground boom and the aerodynamic performance of the vehicle throughout the cruise condition. The development of a viable business jet involves a great deal of detailed work in areas such as inlet integration, cabin design, gear design, stability & control, high

lift design that have not been considered here. This thesis work focuses instead on the development of a multi-fidelity design method that is able to account for some of the fundamental aspects of supersonic aircraft and design. As such, the results of this thesis are not meant to represent actual realizable designs but, instead, the demonstration of a design procedure that may be used to produce such designs.

1.2.1 Problem Specification

$$\begin{aligned} & \min_{\mathbf{x} \in X} f(\mathbf{x}) \\ \text{s.t.} \quad & C_i(\mathbf{x}) \leq 0, \quad i = 0, 1, \dots, p \quad \text{and} \quad \mathbf{x}_l \leq \mathbf{x} \leq \mathbf{x}_u \end{aligned} \tag{1.1}$$

where $\mathbf{x} \in \mathcal{R}^n$ is the input vector with lower and upper bounds, \mathbf{x}_l and \mathbf{x}_u .

The geometry and mission of a configuration of interest are represented with a set of design parameters/variables. The problem then becomes a n dimensional constrained nonlinear optimization problem, where n is the number of design variables. Some parameters are related to the mission/flight condition such as the flight altitude, or the design C_L . Using an objective function, $f(\mathbf{x})$ for either sonic boom loudness or aerodynamic performance, the problem also becomes a simulation-based optimization problem. The allowable variations of the design variables of the problem can be restricted by upper and lower bounds (\mathbf{x}_l and \mathbf{x}_u) or by more complicated linear or non-linear functions of the design variables.

The supersonic jets we try to optimize have a Mach number range between 1.6 and 2.0 and can carry 6-8 passengers. The cruise range is typically about 4,000 nmi and the T/O field length is required to be shorter than 6,500 ft for a feasible design.

1.2.2 Importance of Mission Constraints and Program for Aircraft Synthesis Study (PASS)

Shape optimization studies for the cruise condition (often called traditional single-point optimization) have been done previously [92, 89]. These optimizations improve the performance at the design condition but often lead to poor performance at other

stages of the mission: longer field lengths for take-off and landing, insufficient climb gradients at the initial and final portions at the cruise condition and inadequate stability & control requirements. The entire mission profile is closely related to the performance of other disciplines as well: boom, structures, stability & control, and propulsion, etc. Therefore a single-discipline optimization or a single-point design tend not to be very useful, since the optimized design is typically not feasible or leads to worse performance in other disciplines.

One example of an optimization result that did not include mission constraints is illustrated below. This optimization was done at an early stage of our design studies [89]. The baseline configuration is shown in Figure 1.3 in yellow. A total of 17 design variables were used to parameterize the wing planform and the fuselage (camber and radius). Comparisons of near-field pressure and ground boom signatures are shown in Figure 1.4. The cruise C_D is reduced by 17.5% from 0.011298 to 0.0093134, and the initial pressure rise in the ground boom by 13.74% from 0.633 to 0.546 psf. Correspondingly, the perceived noise level reduction is 2 pldB from 94 to 92 pldB (detailed noise metrics will be discussed in the next Chapter). Despite this significant amount of reduction in the boom and coefficient of drag, the optimized configuration has unreasonably small wing area (as shown in Figure 1.4), and without significant consideration of mission requirements this configuration turned out to be infeasible when simplified constraints for trim, longitudinal stability and fuel volume (detailed calculations can be found in reference [89]) were accounted for.

Therefore, realistic constraints which require the design to be able to fly the entire mission profile become critical in viable design optimization. One of the major contributions of this thesis over previous work is the fact that a relatively complete set of mission requirements are considered in the design procedure. In addition, two objectives are employed: MTOW (Maximum Take-Off Weight) and ground boom loudness.

PASS (Program for Aircraft Synthesis Study) [83, 85] is an aircraft preliminary design tool that has been developed at both the Aircraft Design Group at Stanford University and Desktop Aeronautics Inc. This tool is based on a combination of McDonnell-Douglas methods, DATCOM correlations, and new analyses developed

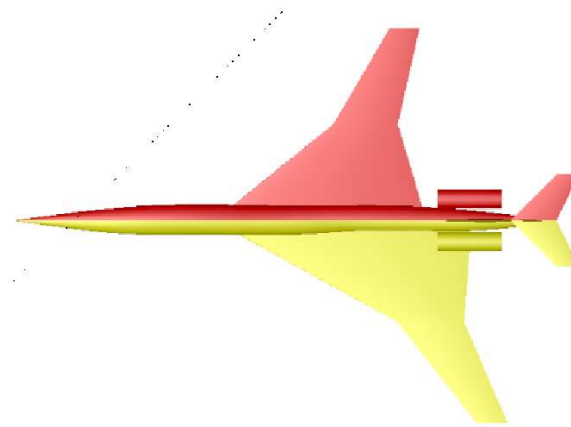
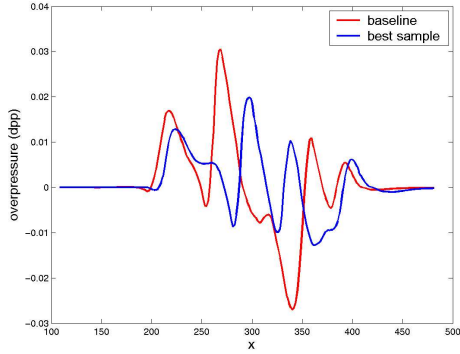


Figure 1.3: Comparison of shape: baseline(bottom) and optimized(top)

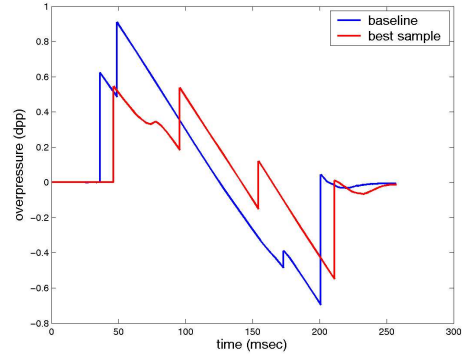
specifically for conceptual design. Over the years it has been successfully used in and perfected through various aircraft design studies in both academia and industry. PASS has separate modules for mission analysis, aerodynamic performance prediction, and a SIMPLEX optimization algorithm. The aerodynamic analysis module is based on classical and fundamental theories and estimates several drag components while the mission analysis tool includes estimation of weight build-ups, range, CG location, a propulsion deck, low-speed stability and trim considerations, etc. The outputs of the mission analyses done with PASS can be provided to an optimizer that is able to handle nonlinearly constrained optimization problems. It must be noted that the version of PASS used in this work has undergone more than 5 years of development by Prof. Ilan Kroo and his collaborators and that it is a fairly refined tool that can be used for conceptual design of viable aircraft. In this thesis work, the optimization runs that used PASS were carried out by Mr. Mathias Wintzer (Desktop Aeronautics, Inc.) using information provided from our multi-fidelity response surface fits.

1.2.3 Variable-Fidelity Aerodynamic Analysis Tools

Many physical phenomena in aerodynamic design require high-fidelity simulations (such as the solution of the nonlinear Euler/Navier-Stokes equations), that are accurate but very expensive even with massively-parallel computing resources. On the



(a) Near-field pressure comparison



(b) Ground boom signature comparison

Figure 1.4: Comparisons of boom performance between baseline and optimized configuration.

other hand, low-fidelity analysis tools such as linear panel methods or analytical classical aerodynamics can predict phenomena fairly well in the regions where appropriate assumptions and simplifications are valid, and can still provide the trends or directions where improvements can take place. These complementary properties of high- and low-fidelity tools suggest that they may be combined effectively into an integrated tool.

The basic idea is that not every portion of the multi-disciplinary analysis of these aircraft must be carried out with high-fidelity: simpler models can often provide very good approximations to such problems as stability & control, propulsion, and basic estimations of aerodynamic performance. In situations where high-fidelity methods are necessary, one may actually benefit from the combined use of low- and high-fidelity models in order to obtain identical solutions to those provided by the high-fidelity model, but with a lower computational cost [80, 81].

Recently such a hybrid approach using both the low- and high-fidelity tools has been drawing interest and many variable-fidelity approximations have been introduced and analyzed [80, 82, 87, 88, 81]. Our optimization problem requires simulation-based direct search methods due to the particular nature of the boom responses for a design space. A variable-fidelity approach can decrease the computational burden by

building surrogate models of the real design space: a combination of low-fidelity tools that are enhanced by multi-fidelity analysis in the areas where accuracy is needed. Our work, however, is based on the inexpensive construction of response surfaces using multi-fidelity tools, rather than on using the various fidelity models directly in the optimization process. In this thesis, PASS has been used to provide the low-fidelity mission and aerodynamic analysis module. The A502/Panair linear panel code provides the mid-/high- fidelity analyses, while an inviscid Euler solver can be used for the highest-fidelity analyses.

1.2.4 Multi-Fidelity Response Surface

Information about the characteristics of the design space is very useful in understanding the nature of the optimization problem we are solving, and can help us select the appropriate type of optimization method to be used. The design spaces for the objectives of the cruise C_D (at fixed C_L) and ground boom loudness have been studied in reference [52]. The sonic boom design space is found to be noisy, discontinuous and multi-modal with multiple local extrema. Thus gradient information may not be available over the entire domain, even though gradients may be found over locally continuous regions. Thus traditional gradient-based optimization methods cannot be employed for this reason: direct search methods with global scope are better suited for this type of problem. A direct search method has various advantages over gradient-based local search methods in that it does not require derivative information or complex mathematical formulas, and is independent of the problem type.

In addition, at a minimum, high-fidelity simulation-based optimization requires high-fidelity CFD analysis of the aerodynamic performance and ground boom during the cruise conditions. CFD-based evaluations of both the performance and the loudness of the ground boom of the aircraft have proven to be expensive [70, 92, 52] and our mesh resolution study [90] in Chapter 2 shows that very high resolution is required to predict accurate near-field pressure signatures. The fundamental problem arises in that the combination of the high-fidelity CFD analyses with a direct search method may incur prohibitive computational costs. Multi-disciplinary aspects make

the problem even more complicated and difficult to handle.

As an alternative, the use of approximate/surrogate models for expensive high-fidelity analysis tools has been drawing great attention in recent studies [110, 111] and has been successfully used in various fields. If the accuracy of the response surface is guaranteed to be close to that of the high-fidelity CFD analyses, then the computational burden can be reduced dramatically. The simplest and most popular surrogate models are based on least-squares regression using low-order polynomials [115], and they have great advantages in handling a large number of sampling points because of the low computational cost. However the multi-modal properties of the design spaces we are interested in can make the use of quadratic models questionable and a global model which can handle multiple local minima/maxima should be considered. One such model derived in deterministic computer experiments is the Kriging method which originates from geo-statistics and has been used in previous work as an accurate approximation model. Earlier work has shown [113, 153, 92, 89] the successful use of the Kriging approximation model when combined with Evolutionary Algorithms (EAs). Although Kriging is an excellent model for dealing with multi-modal design spaces, it has limitations related to the number of interpolating sampling points. Considering the complimentary characteristics of low-order polynomial-based least-squares regression and of the Kriging model, a hybrid model for multi-fidelity response surfaces is constructed in this thesis. The number of analyses with each tool decreases with increasing fidelity (and cost). A large number of low-fidelity analyses were performed and used to construct the quadratic fit. Then a moderate/small number of high-fidelity analyses were carried out in the region where low-fidelity analyses cannot provide the required level of accuracy. The Kriging fit was then constructed for the error in the solution. The combination of these two response surface becomes the multi-fidelity response surface that is used directly by the optimizer.

1.2.5 Two-Level Optimization: Global and Local Optimization

It has been mentioned that due to the particular properties of our noisy objective functions an efficient gradient-based optimization is not likely to locate a global optimum. For this reason computationally expensive direct search methods must be used in the optimization process. The situation only worsens as we include more design variables. On the other hand, local optimization methods can have an advantage in smooth design spaces by using gradient sensitivity information and driving the descent direction to accelerate convergence. These gradient-based methods require fewer function evaluations and show better convergence and scaling behavior. If gradient information can be obtained and used, the adjoint method [94, 95, 96, 97] is an efficient way of obtaining gradient values in a single run by solving an auxiliary adjoint equation. Its cost is independent of the number of design variables.

We can infer that the global and local search methods have complementary properties regarding the number of function evaluations required and the feasible number of design variables. There have recently been several efforts on combining those two different search methods. A new optimization method [119] which allows the designer to have the necessary freedom to explore the design space using a reasonably large number of design variables has been sought in this thesis under the name of Two-level optimization. It combines the sequential application of a global search step (using multi-fidelity response surfaces) followed by a local gradient-based search in a single optimization process. During the global optimization, a moderate number of design variables is introduced with rather large allowable variations and a direct search method locates a near-optimum design point. Then a local gradient-based optimization method performs a local search around the design site identified by the global search step. In this second step, large numbers of design variables are introduced and further improvement can be achieved. We employ the nonlinear SIMPLEX and GAs (Genetic Algorithms) as global optimizers, and the NPSOL SQP (Sequential Quadratic Programming) solver combined with an adjoint solver as a local optimizer.

The SQP solver is particularly well-suited for the local search step due to its well-known ability to efficiently locate the local optima of optimization problems with general constraints [118].

1.3 Organization of Thesis

In Chapter 2, the sonic boom phenomenon for real flight involving flight maneuvers and atmospheric gradients is explained. A historical review of sonic boom analysis is also briefly described. A proper measure of ground boom noise level is also introduced. Detailed descriptions of our high-fidelity boom analysis tool, BOOM-UA, are given in Chapter 3. The tool is validated by comparing the near-field pressure distribution and the ground boom signature with wind-tunnel experimental data. Chapter 4 shows our various-fidelity analysis tools, from low-, to mid- and high-fidelity. The similarities and discrepancies in the predictions of aerodynamic performance and ground boom between different analysis tools are compared. In Chapter 5, the characteristics of the design space are illustrated and the necessity of using surrogate models and direct search methods is explained. Various types of surrogate models are introduced and are compared. A multi-fidelity response surface composed of various-fidelity analysis tools and two different surrogate models is constructed. Finally, Chapter 6 presents results from two different design optimization cases: Designs I and II. In Design I, a nonlinear SIMPLEX-based global optimization is performed using the full hierarchy of various-fidelity analysis tools. Design II was performed using the two-level optimization idea. Since an adjoint-solver was involved for gradient information at the second level, the boom objective was not considered, as a full adjoint for the ground boom problem is not yet available and may present some difficulties since once the ground signature is fully coalesced, it is not possible to determine a unique corresponding near-field signature.

Chapter 2

Sonic Boom

This chapter briefly describes the sonic boom phenomenon during the entire mission of supersonic flight. The concepts and methodologies used in sonic boom analysis are based on two fundamental methods, the F-function method and waveform parameter method, which are investigated in sections 2.2 and 2.3. A historical review of sonic boom minimization efforts is also presented. Several methods to quantify the loudness of ground boom signatures are also discussed.

2.1 Sonic Boom Analysis

2.1.1 Formation of Sonic Boom: Boom Carpets

Pressure disturbances from aircraft in supersonic flight propagate through the inhomogeneous atmosphere and distort ultimately generating N-waves as is shown Figure 1.1. The N-wave moves during continuous supersonic flight and given its spanwise extent results in a sonic boom *carpet* on the ground, whose width depends on vehicle and atmospheric conditions, spanning out under the full length of a supersonic flight [23].

The boom carpets associated with supersonic flight from landing to take-off are shown in Figure 2.1 from [26]. The primary boom carpet shows a typical N-wave resulting from the wave propagation through only the part of the atmosphere below

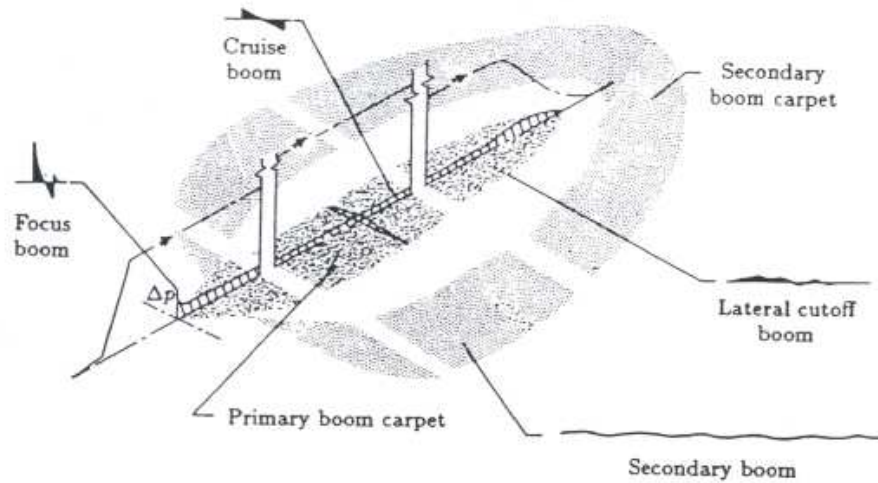


Figure 2.1: Ground boom phenomena. From [26]

the aircraft. The intensity typically ranges from 1 to 3 psf with a duration of 0.1 to 0.3 sec. Secondary boom carpets came mostly from wave refraction through the atmosphere above the aircraft, and they are located farther from the ground track. The overpressure level is not as high as in the primary carpet, ranging from about 0.02 to 0.2 psf for longer periods of time. If the aircraft accelerates, the width of the boom carpet increases and its shape changes. Overlapping of the boom carpets cause a *caustic* and this focused sonic boom is called *superboom* [24]. In this study, we focused on the primary sonic boom signature at the cruise condition.

There are several factors that can influence the shape, location, and strength of sonic booms: weight, size, and shape of the aircraft or vehicle, attitude and flight path, and weather or atmospheric conditions. Of all the factors influencing sonic booms, increasing altitude is the most effective method of reducing sonic boom intensity.

Geometric acoustics, isentropic wave theory and ray theory are well suited to explain the nonlinear wave propagation through the stratified atmosphere, although the theories will fail around the region of the caustic. The concept of waves and rays is shown in Figure 2.2. A wavefront is a geometric entity, and a ray is the trajectory of a signal point, hence a rather kinematic entity.

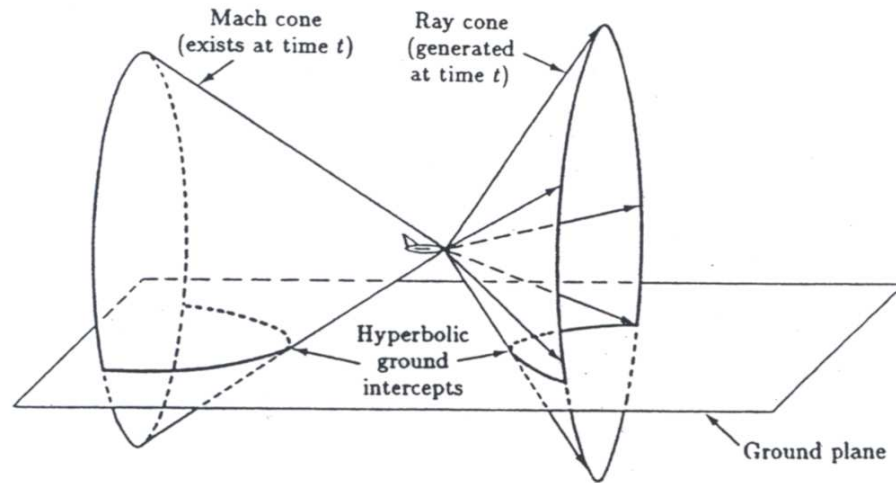


Figure 2.2: Mach cone and ray cone in supersonic flight. From [26]

According to the theories, the signal which contains the Blokhintsev energy invariant related to the F -function [32, 33], which is explained in section 2.2.2, propagates along rays. However in a stratified atmosphere, the physical variables are a function of altitude and vary along the ray. This change in properties can result in the refraction of the ray and in significant changes in ray tube area. Geometric acoustics can account for those phenomena [34]. For more details the reader is referred to [21]. The *F-function method* and *waveform parameter method* have been used to investigate these nonlinear phenomenon.

2.1.2 Brief Historical Review of Sonic Boom Analysis

Sonic boom analysis dates back to the classical sonic boom theory developed by Whitham in the 1950's. Whitham analyzed the flow pattern of a supersonic projectile. Despite restrictive assumptions in geometry (such as slender and axisymmetrical body) and uniform atmosphere, he suggested some basic corrections to the failure of linearized theory in predicting the sonic boom. Whitham considered only the volume contribution to the sonic boom, which often underpredicts the boom amplitude. The supersonic area rule theory [6, 8] was introduced by Whitcomb to add the effect of the wing, and Walkden [38] applied that theory to wing-body configurations. George [9]

generalized the first order approximation of Walkden’s far-field approximation by extending it to higher order terms, which play an important role in advanced source methods developed in the 1980s and 90s. His analysis can be applied to conventional supersonic aircraft. The underpredicted amplitude issue was corrected by applying a factor of $\sqrt{\frac{p_g}{p_a}}$, where p_g and p_a are the ground and altitude static pressure, to Whitham’s original uniform atmosphere results. The Whitham/Walkden theory adjusted for altitude was successful in predicting sonic boom phenomena in the 1960s and 1970s. Carlson [10, 11] validated the theory with wind-tunnel experiments. The effects of maneuvers as well as of winds in a horizontally stratified atmosphere were considered in the first computer model by Hayes et al [17]., known as the ARAP model. In the late 1960s, Thomas [34] proposed a new algorithm, the *waveform parameter method*, where ray tracing was accomplished by numerically integrating a set of ray paths through the atmosphere rather than evaluating a set of closed-form quadratures in Hayes’ method. Plotkin et al. performed very extensive research into the effects of aircraft maneuvers on the sonic boom [21, 23, 24, 25]. In the late 1970s, Carlson [12] proposed a simplified prediction method that reduces to a manual calculation of the N-wave based on a set of “shape factors” that represent the sonic boom source strengths for various aircraft types. Area-rule and wind-tunnel data [36] were the main source of near-field data, which is the initial data for calculating far-field propagation using the F-function method. However wind tunnel data is expensive to obtain and the F-function method can be complicated for complex geometries. A nonlinear Euler analysis with the aid of rapid development in CFD was used to obtain near-field data by Cheung and Siclari [27, 29] in the early 1990’s. The work in this thesis follows this approach with more sophisticated numerical and meshing techniques.

2.2 F-function Method

2.2.1 Whitham F-function

In 1952, Whitham [7] modified the supersonic flow linearized theory to predict the flow pattern around a supersonic projectile. This theory is based on the geometrical assumptions of a slender and axi-symmetric body or of a large distance from the non-axisymmetrical slender body, which ensures small disturbances.

In the well-known linearized theory [162], the disturbance propagates along straight and parallel characteristics $x - r\sqrt{(M^2 - 1)}$, where x is the radial distance along the axis from the nose, r the distance from the axis and M the freestream Mach number. However, the characteristics around the projectile follow a curved path with the region of disturbed flow spreading out because of the nonlinear phenomena, and ultimately diverging. The approximate characteristic variable $x - r\sqrt{(M^2 - 1)}$ was replaced by the exact one $y(x, r)$ such that $y = \text{constant}$. Although this correction is valid only for a solution far away from the aircraft, Whitham introduced an important concept in sonic boom analysis, the F-function, which is determined from the geometrical details of the aircraft configuration and is a starting point to apply geometric acoustics. Given

$$x = \beta\gamma + y - \frac{\sqrt{\gamma}(\gamma + 1)M^4}{\sqrt{2\beta^3}}F(y), \quad (2.1)$$

where $\beta = \sqrt{M^2 - 1}$ and $F(y)$ is a Whitham F-function.

For the smooth body,

$$F(y) = \frac{1}{2\pi} \int_0^y \frac{S''(t)}{\sqrt{y-t}} dt, \quad (2.2)$$

where $S(x)$ is the cross sectional area for the body. If the body has a discontinuous slope, $S(x)$, then

$$F(y) = \int_0^\infty \left(\frac{2}{\beta R(t)} \right)^{1/2} h \left(\frac{y-t}{\beta R(t)} \right) \frac{dS'(t)}{2\pi}, \quad (2.3)$$

where $h(x) = \sqrt{\frac{\pi}{2p}} \frac{1}{K_1(p)} H(x)$ and K_1 is the Bessel function and $H(x)$ is the heavyside

function. The limit of Whitham's formula is that the body should be axisymmetric and it is valid only at a large distances from the body.

For a general case of a nonaxisymmetric body, provided that $x - \beta r \ll r$, at distances which are large compared with the body length, the asymptotic solution from linearized theory can be generally expressed as follows [39, 19]:

$$\frac{\Delta p(x, r; \theta)}{\gamma p M^2} = \frac{1}{2} C_p \cong \frac{1}{\sqrt{2\beta r}} F(t; \theta), \quad (2.4)$$

where the function $F(t; \theta) = \frac{1}{2\pi} \int_0^t \frac{A'(x; \theta)}{\sqrt{r^2 t^2 - x^2}} dx$ is the Whitham F-function. $A(x)$ stands for an equivalent area which is a function of the azimuthal angle (θ) about an x axis of the flight direction. The equivalent area consists of two components; the actual area cut by a plane tangent to the Mach cone at the particular azimuth, θ , and the effective area directly proportional to the axial distribution of lift in that direction [16, 18, 37, 38, 39].

Walkden [38] extended Whitham's theory to analyze the sonic boom in terms of volume-induced and lift-induced components corresponding to different contributions of equivalent area. Seebass [39] gave very good representation of the two components.

$$S(x; \theta) = S_V(x; \theta) + S_L(x; \theta), \quad (2.5)$$

where $S_V(x; \theta)$ is the same as the area cut by the fore Mach cone projected on to an $x = \text{const}$ plane, and $S_L(x; \theta) = \beta \int_0^x L(t; \theta) \frac{dt}{\rho U^2}$. Here L is the component of force perpendicular to the freestream that lies in the $\theta = \text{const}$ plane.

If the near-field pressure distribution is available, either by wind-tunnel experiment or by high-fidelity CFD analysis, the F-function can be obtained easily by using the relation in the equation 2.4. By inputting C_p or a pressure disturbance at some distance away, the F-function can be obtained without considering the source and lift distributions equivalent to the aircraft configuration. However the computation should be implemented beyond some radius r at which pressure disturbance is sufficiently small such that Whitham's far-field assumptions are nearly satisfied.

2.2.2 Propagation Through the Real Atmosphere

The propagation of a near-field pressure disturbance to the ground can be explained using geometric acoustics where the concept of wavefront and ray are critical concepts and defined in Figure 2.2. A *wavefront* is a geometric shape that moves through space. A *ray* is defined by the normals to the acoustic wavefronts and it is a kinematic point trajectory along which an acoustic signal propagates. The velocity of a signal along a ray is termed the ray velocity,

$$c = a + u = a_0 \left(1 + \frac{\gamma + 1}{2\gamma} \frac{\delta p}{p_0} \right), \quad (2.6)$$

where a_0 is the undisturbed speed of sound, and u is the wind velocity (velocity perturbation). In an uniform atmosphere a_0 and u are constant and the rays are straight and parallel. However the rays are usually curved paths due to existing gradients in a and u . Ray tracing is the first step in the calculation of the sonic boom and can be done only if the aircraft trajectory and the atmospheric properties are known. However the calculation of rays does not provide any description of the acoustic signals.

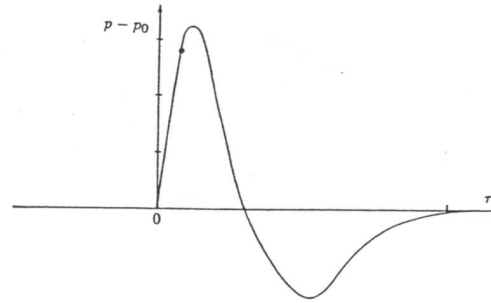
An acoustic signal is described in terms of the pressure signature as a function of a phase, $\delta p(\xi)$, which can be chosen as the time $t - t_0$ measured by a fixed observer from the time t_0 when a wave front passes by. According to the modified conservation law [44, 33, 32], the Blokhintsev energy invariant is constant along a ray tube for each value of the phase and is defined as follows:

$$V(\xi)^2 = \frac{\delta p^2}{\rho a^2} \frac{c_n}{a} \mathbf{c} \cdot \mathbf{A}, \quad (2.7)$$

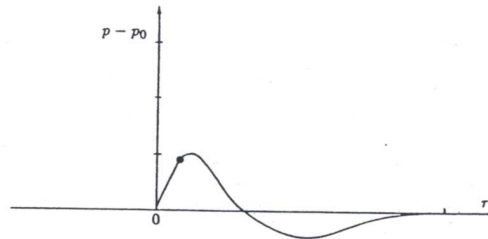
where c_n , \mathbf{A} , ρ and a are functions only of altitude with the assumption of a stratified (layered) atmosphere, and vary along the ray tube. From equations 2.6 and 2.7, the age variable τ can be defined as follows [17, 34]:

$$\tau = -\frac{\gamma + 1}{2c_0^{3/2}} \int_{z_1}^{z_2} \frac{1}{\rho_0 a_0^2 A_h \sin^3 \theta \cos^3 \theta^{1/2}} dz, \quad (2.8)$$

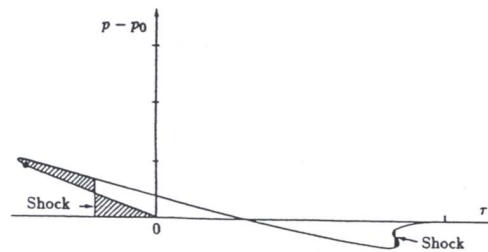
where A_h is the ray tube area given by the area cut by a horizontal plane.



(a) Signature near aircraft (*F*-function shape).



(b) Far-field acoustic amplitude change (*F*-function shape).



(c) Far-field steepened (*aged*) signature.

Figure 2.3: Evolution and steepening of sonic boom signature. From [26]

Equation 2.2.2 is the fundamental equation of the *F*-function method and accounts for the atmospheric effects on both the waveform shape and waveform amplitude. Nonlinear effects are due to the differences in propagation speed, c , from the speed of sound in the ambient atmosphere, a . Thus the changed signal speed changes the linear phase ξ and results in a distortion of the signal. In the definition of the age variable, only the ray tube area is important. Due to the ray tube area factor, the amplitude of the wave undergoes changes. The ray tube is outlined in Figure 2.4,

where t is time and ϕ is the azimuth angle.

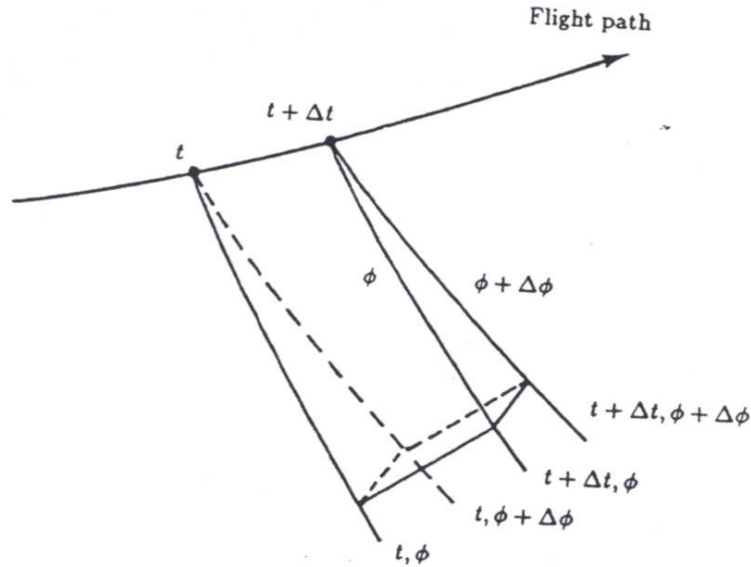


Figure 2.4: Rectangular ray tube outlined by four rays. From [26]

The calculation of the ray path and ray tube area can be implemented by solving a set of differential equations called the derived ray equations [20]. The variation of a ray tube area in a stratified atmosphere with winds and caused by a maneuvering aircraft is available as well [17].

Because of the nonlinear distortion and steepening, the final acoustic signature can have multi-values in pressure. This phenomenon is physically impossible. This problem can be solved by locating the *shock* according to the *area-balancing rule*. The area-balancing rule is a consequence of the fact that the propagation speed of a weak shock is equal to the average of the propagation speeds $u + a$ just ahead of and just behind the shock. Figure 2.3 shows the process of shock evolution and steepening and the area-balancing rule.

When the sonic boom arrives at a rigid surface such as the ground, it is reflected and local pressures on the surface are double what they would be in free air. This phenomenon is accounted for by multiplying the sonic boom ground signature by reflection factor of 1.9.

2.3 Waveform Parameter Method

The waveform parameter method [34, 35] is another method to carry out the extrapolation of near-field signatures to the far field. Although a proper mathematical derivation of this method does not seem to have been published, it is simpler and more intuitive, as it handles the signature itself rather than the F-function. This approach approximates the waveform by an arbitrary number of linear segments and defines three waveform parameters for each segment as a function of time. Then, coupled ordinary differential equations for these waveform parameters are derived from conservation laws along the rays, and solved with given initial and boundary conditions. The corresponding solutions for the waveform parameters determine the physical variables at any point along the ray paths. One of the great advantages of the waveform parameter method over the F-function method is that it is fairly easy to implement on a computer, since the problem can be reduced to the solution of coupled ordinary differential equations. Therefore it can be applied to any shape signature and provides a continuous evolution of the shape as the signature is propagated. It does not use age variables to account for nonlinear distortion, and does not require an area-balancing criterion to locate the shock waves.

2.3.1 Waveform Parameters

For each linear segment on the waveform, the waveform parameters, $\Delta p_i, m_i, \lambda_i$ are defined as follows: Δp_i is the pressure rise across the shock at the juncture of segments i and $i - 1$, m_i is the slope of segment i , which can be positive or negative, and λ_i is the length of segment i . These waveform parameters are corresponding to a waveform (i.e. ray) perpendicular to the wavefront.

It is assumed that the waveform parameters can be obtained by superposition of the rate of change obtained assuming the wave propagates as if it were a linear, nonplanar wave and the rate of change assuming the wave propagates as a nonlinear,

planar wave.

$$\left(\frac{dE_i}{dt}\right)_{\text{nonlinear nonplanar}} = \left(\frac{dE_i}{dt}\right)_{\text{linear nonplanar}} + \left(\frac{dE_i}{dt}\right)_{\text{nonlinear planar}}, \quad (2.9)$$

where E can be any of Δp or m_i , or λ_i . The second term in the right hand side accounts for the nonlinear distortion of the waveform.

2.3.2 Linear, Nonplanar Wave

The first term in right hand side of equation 2.9 accounts for the effects of changing ray tube area and changing atmospheric properties. As in the F-function method, from the equation 2.7 and from the constant segment length conservation relation [44], $\frac{\lambda_i}{c_n} = \text{constant}$ along a ray tube, the following equations are derived:

$$\frac{dm_i}{dt} = \frac{m_i}{2} \left[\frac{3}{a_0} \frac{da_0}{dt} + \frac{1}{\rho_0} \frac{d\rho_0}{dt} - \frac{4}{c_n} \frac{dc_n}{dt} - \frac{1}{A} \frac{dA}{dt} \right] \quad (2.10)$$

$$\frac{d\Delta p_i}{dt} = \frac{\Delta p_i}{2} \left[\frac{3}{a_0} \frac{da_0}{dt} + \frac{1}{\rho_0} \frac{d\rho_0}{dt} - \frac{2}{c_n} \frac{dc_n}{dt} - \frac{1}{A} \frac{dA}{dt} \right] \quad (2.11)$$

$$\frac{d\lambda_i}{dt} = \frac{\lambda_i}{c_n} \frac{dc_n}{dt}, \quad (2.12)$$

where $c_n = a_0 + \mathbf{V}_0 \cdot \mathbf{N}$ and \mathbf{V}_0 is wind velocity and \mathbf{N} is the waveform normal vector.

2.3.3 Nonlinear, Planar Wave

The second term in the right hand side of equation 2.9 is obtained from the assumption that the wave propagates as a finite-amplitude, isentropic wave. If the shock in the sonic boom is reasonably weak, then it propagates at a speed equal to $u + a$ as in equation 2.6. Using these results, the waveform parameter rates of change for a nonlinear, planar wave can be stated as follows [35]:

$$\frac{dm_i}{dt} = km_i^2 \quad (2.13)$$

$$\frac{d\Delta p_i}{dt} = \frac{1}{2}k\Delta p_i(m_i + m_{i-1}) \quad (2.14)$$

$$\frac{d\lambda_i}{dt} = -\frac{1}{2}k(\Delta p_i + \Delta p_{i+1}) - km_i\lambda_i, \quad (2.15)$$

where $k = \frac{\gamma+1}{2\gamma} \frac{a_0}{p_0}$. The effect of the atmosphere is included in the parameter k in equation 2.13

2.3.4 Nonlinear, Nonplanar Wave

The total waveform parameter rates of change for a nonlinear, nonplanar wave are simply the addition of equations 2.10 and 2.13 under the assumption of equation 2.9. The unknowns are the fractional rates of change of the ambient properties, a_0 , ρ_0 and c_n , and those can be determined if a ray path is calculated by the method described in reference [35]. The fractional rate of change of ray tube area is also needed along the ray path and it can be calculated by the theoretical method [17] or directly determined by the bounded area of four neighboring rays. With the waveform near the aircraft known, the solutions for the waveform parameter can be used to determine the waveform at any point along the ray. In the special case of a uniform atmosphere, closed-form expressions can be obtained [34].

A shock is introduced where the value of λ_i goes to zero and the corresponding Δt can be obtained. Then the new waveform parameters are redefined to introduce the shock.

All procedures can be automated with the aid of computer programming and the effects of aircraft acceleration and atmospheric temperature, pressure and wind gradients can be easily included in the ray path calculation.

2.4 Sonic Boom Minimization

Most efforts directed towards sonic boom mitigation have been based on the tailoring (or *shaping*) of the sonic boom signature so that the magnitude of the front and rear shock waves in an N-wave are minimized [40]. In fact, it has often been the approach to alter the boom signature such that ramps, flattops and multi-shock shapes are created [43]. The accurate and efficient computation and propagation of such *shaped booms* is a much more challenging task than for N-waves; to date, there have only been a few studies relating to the ability of CFD-based sonic signature methods to predict the phenomenon accurately [28, 30, 31], and none of them has particularly focused on the propagation of shaped booms.

Our earlier research on low-boom aircraft design was mainly focused on the reduction of the magnitude of only the initial peak of the ground boom signature [51]. This requirement, which had been suggested as the goal of the DARPA-sponsored Quiet Supersonic Platform (QSP) program ($\Delta p_0 < 0.3$ psf), hides the importance of the rest of the signature, which often arises from the more geometrically complex aft portion of the aircraft where empennage and engine nacelles and diverters create more complicated flow patterns. Moreover, such designs often have two shock waves very closely following each other in the front portion of the signature [52, 31], a behavior that is not robust and is therefore undesirable. Therefore, instead of minimizing certain portions of the entire sonic boom signature, noise loudness metrics which involve the entire pressure signature and are directly related to the human hearing system are more suitable objectives to minimize sonic boom. The next section describes the details of noise metric definitions.

2.5 Sonic Boom Noise Metrics

The efforts to minimize the sonic boom are closely related to the way in which sonic boom loudness is measured. Several options for measuring sonic boom loudness include:

1. Seebass and George defined a “figure of merit (FM)” to characterize the sonic

boom levels of various aircraft. FM is proportional to the aircraft weight divided by three-halves of the aircraft length, $FM = W/(2/3L) = 2W/3L$. Aircraft with a lower value of FM generate a less intensive sonic boom. Based on their calculation, they found the Concorde has $FM=1.4$ and the Boeing 2707 concept had $FM=1.9$.

2. The initial shock pressure rise of the ground wave has often been the objective of sonic boom minimization work, as was explained in section 2.4. It was pointed out that the reduction of the initial rise often leads to ignoring the tail shock strength.
3. Sonic boom loudness in dB can provide measures more related to the human hearing system, and loudness metrics are calculated using the entire pressure signature.

The loudness metric in dB was selected as the measure of sonic boom noise level for this thesis work. This kind of loudness metric is a more reliable measure of the disturbances due to sonic booms than the sonic boom overpressure level. The human hearing system does not directly respond equally to all the frequencies in the pressure signature while the purpose of sonic boom minimization is closely related to human perception. A variety of calculation procedures are used which attempt to quantify the complex characteristics of human hearing and human psychology. They are all based on the decibel scale (dB). The range of frequencies that the human ear can hear is about 20 Hz to about 20,000Hz, with the range of 1,000 to 4,000 Hz being the most sensitive. Therefore when measuring community response to the noise, it is common to adjust the frequency content of the measured sound to correspond to the frequency sensitivity of the human ear. This procedure is called weighting.

2.5.1 Weighting Networks

Weighting networks are implemented by electronic filters and are built into sound level meters to provide a meter response that tries to approximate the way the human ear

responds to the loudness of pure tones. Frequency response characteristics corresponding to several weighting networks, which are derived from the Fletcher/Munson equal loudness contours [48], are shown in Figure 2.5. The most common weights are the following, see Figure 2.5:

1. A-approximation of 40 phon line (filters low frequencies)
2. B-approximation of 70 phon line
3. C-approximation of 100 phon line (almost flat)
4. D-developed for aircraft flyover noise (penalizes high frequencies)

Higher frequency sounds that are most noticeable to human hearing are generally measured using the so-called A-weighted scale(dBA). A-weight is the most common scale since it correlates reasonably well with hearing damage, and it is easy to implement in a filter network. It is a simple measure and is used in most regulations. But lower frequencies are not accurately reflected by the A-weighted scale.

A C-weighted scale can more accurately measure low frequency sounds than the A-weighted noise level. For impulsive noise being followed by secondary noise from structural vibration, the C-weighted scale is more appropriate. This is due to the fact that C-weighting is nearly flat throughout the audible frequency range as in Figure 2.5 and can emphasize the low-frequency components of the noise.

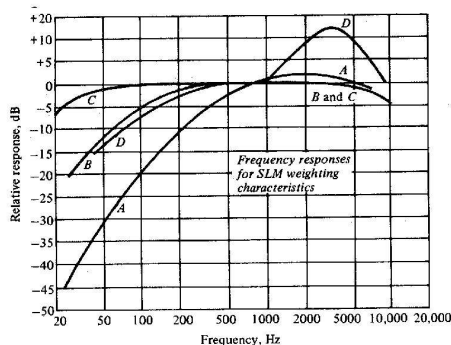


Figure 2.5: Frequency response characteristics of various weighting networks [48].

Other weighting networks have been developed to correspond to the sensitivity and perception of other types of sound, such as “B” and “D” filters. D-weighted sound level (dBD) filters low-frequency noise to recognize annoyance with high-frequency noise and is often used as an approximation to the Perceived Noise Level (PNL). PNL is almost exclusively used for aircraft noise assessment. PNL is computed from sound

pressure levels measured in octave or one-third octave frequency bands. This rating is most accurate in estimating the perceived noisiness of broadband sounds of similar time durations which do not contain strong discrete frequency components. Effective Perceived Noise Level (EPNL) can be derived from PNL and provide a single quantitative measure of complex aircraft flyover noise which approximates human annoyance responses.

In this study, A-weighted sound levels (dBA) are mostly used, since they have been adopted as the basic measure of community environmental noise by the U.S. EPA (Environmental Protection Agency) and most other organizations concerned with aircraft noise in the U.S. A C-weighted sound level and PNL are also used in some of the design cases (validation with experiments in Chapter 3).

2.5.2 Shock Rise Time and Turbulence in Atmosphere

In theory, a shock is a discontinuous jump in physical state over infinitesimally short time periods. However, in a real standard atmosphere the shock occurs over finite time period, called the *rise time*. The inner shock structure of a sonic boom propagating through the atmosphere is affected by dispersion and dissipation associated with physical phenomena such as classical absorption, thermoviscosity, molecular relaxation, and turbulence scattering. Accurate prediction of the rise time is important, as the sonic boom loudness level depends primarily on it.

Molecular relaxation [46] due to internal vibration energies of polyatomic molecules (N_2 and O_2) causes dispersion/diffraction in the atmosphere and absorbs sound. Stratification of the atmosphere leads to significant variation of the relaxation process with altitude, and the shock profile can adjust very quickly to changes in attenuation so that it always appears to be in steady state. Reference [46] showed that the augmented Burgers's equation and the relaxation equation are reduced to equations which can be solved by numerical integration. However, a study [74] shows that the consideration of relaxation only is not enough to explain the shock rise time phenomenon and turbulence effects should be included.

The effects of turbulence intensity and propagation distance through turbulence

are investigated in reference [47, 75]. Turbulence is known to distort sonic booms in several ways. Turbulence scatters the ray-paths, which may focus or de-focus the magnitude of the sonic boom at any point. Turbulence can also increase the length of scattered ray-paths and delay the scattering process. This distortion affects the high-frequency content of a boom, and is therefore important to loudness [73]. Average rise time increases with turbulence intensity and propagation distance, and average peak pressure decreases slowly correspondingly .

In this study, two types of rise time modification are considered: the $1/\Delta P$ type and the TanH type.

Firstly, if only the thermoviscous effects are considered, the following TanH equation can be used to represent the pressure rise P , within a shock as a function of time [75, 76]:

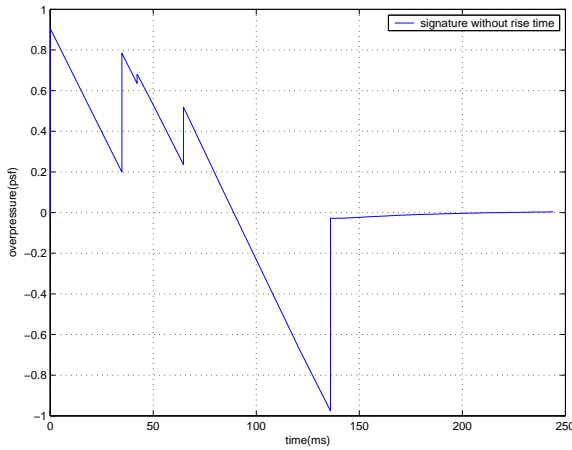
$$P(t) = \frac{1}{2}P_{sh} \left[1 + \tanh \left(\frac{2t}{L} \right) \right], \quad (2.16)$$

where L is the thickness parameter and P_{sh} is the shock amplitude. Nominal values of $2.089\text{e-}5$ seconds for pressure units in Pascals, 90.001 seconds for pressure units in psf) are typically used for L . This shock thickening process is applied to the entire waveform.

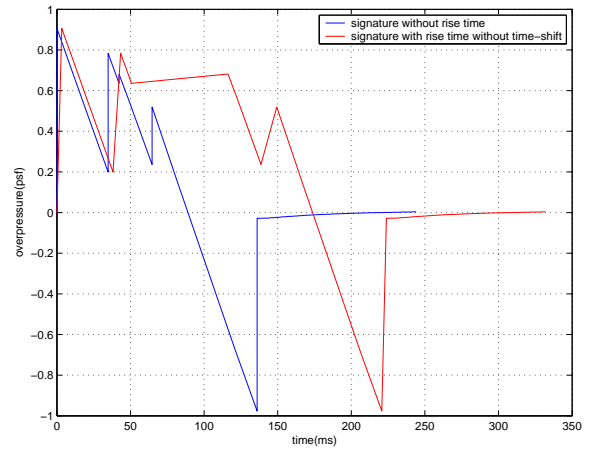
The second model is an empirical model of rise time modification, and this model is employed in this thesis. It is a fit through experimental data. See references [77, 31], which include both the effects of molecular relaxation and turbulence

$$T = \frac{0.3}{\Delta P}, \quad (2.17)$$

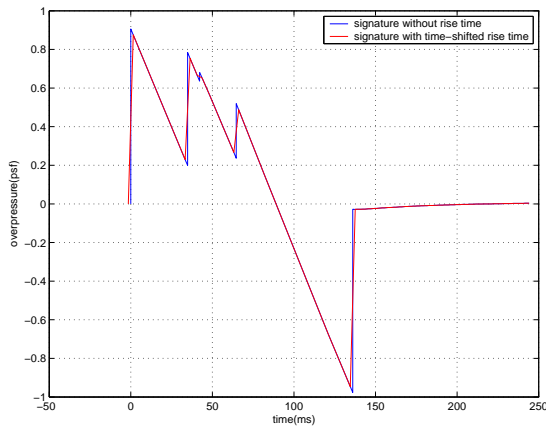
where T is the rise time in seconds and ΔP the shock amplitude in pounds per foot. If a time shift is not considered in this simple form of rise time modification, the total duration of ground boom increases as shown in Figure 2.6 (b). Figure 2.6 shows three ground boom signatures of the baseline configuration used in section 6.1. The boom signatures without rise time modification, with rise time modification with no time shift, and time-shifted rise time modification are shown respectively. Loudness metrics corresponding to each of these signatures are named as dBA0, dBA1 and dBA3, respectively.



(a) signature without rise time



(b) signature with rise time without time shift



(c) signature with rise time with time shift

Figure 2.6: Ground boom signature with/without rise time modification.

Chapter 3

Automated Boom and Aerodynamic Performance Prediction

The propagation of N-wave signatures to the ground has been pursued in the past with some degree of success [71, 70, 157] but without a clear understanding of the numerical requirements for the CFD portion of the problem. This has been mainly due to the lack of computational power necessary to carry out credible mesh refinement studies.

There have been many difficulties in analyzing sonic boom signatures with CFD methods. These problems are associated with issues of mesh resolution, artificial dissipation formulation, two-dimensional versus three-dimensional signature propagation methods, and the actual formulation of the propagation procedures. Detailed studies are needed to establish minimum requirements for the accurate analysis and design of low-boom aircraft.

Especially regarding the mesh resolution issue, no actual guidelines have been issued yet as to the mesh element size and distribution required for accurate off-body pressure computation. This mesh resolution/distribution issue is tightly coupled with the fact that complex geometry representation (full configurations including nacelles, diverters, etc.) is typically necessary in the shaping of low sonic boom aircraft.

Complete configurations also require higher mesh resolution for capturing shock and expansion waves around the aircraft.

Unstructured meshes are ideally suited to address the issues of automatic meshing around complete aircraft configurations and mesh resolution/distribution [53, 65]. In fact, unstructured meshes have more flexibility for adding or deleting points arbitrarily from the computational domain. They can be easily refined and coarsened adaptively with information provided by the flow solutions. This adaptive mesh refinement strategy can improve computational efficiency in the presence of finite computing resources. Depending on the resulting flow field and possible error estimates in the numerical solution, isotropic or anisotropic refinement may be more appropriate.

In this section, we demonstrate the validity and accuracy of the BOOM-UA sonic boom computation framework which has been developed at Stanford by comparing the results directly with experimental data. We analyze a supersonic business jet (SBJ) configuration, which we call NASA SBJ, designed and tested at the NASA Langley Research Center that produces near N-waves at the ground plane. Basic variations of the original configuration are made by removing the nacelles and vertical tail to investigate their effects on the near field and ground boom signatures. In BOOM-UA, the analyses of aerodynamic performance and sonic boom are carried out using a tetrahedral unstructured adaptive flow solver and the PCBoom3 acoustic propagation software of Plotkin [71]. The details are shown in the next section.

Solution adaptive meshes are generated through several flow solution and adaption cycles. Using these meshes, near-field pressure distributions are extracted at distances of 9.5in, 12in and 18in below the aircraft for each configuration (corresponding to R/L values of 0.59375, 0.75, and 1.125 respectively) and are compared with the existing wind-tunnel data.

Once the near-field data has been validated, signatures are propagated to the ground to determine the variations in signature shape and perceived loudness caused by disagreements in the near-field information. Additional comparisons with the results obtained with a linearized, supersonic panel method are made in order to illustrate the differences that result from the use of high-fidelity CFD.

The objective of this validation work is to simply establish a minimum set of

requirements that must be met by all computations of sonic boom phenomena. For that purpose, as the results are analyzed, we suggest typical mesh and element sizes that may be required in order to produce ground boom signatures with a level of error less than 5%.

3.1 BOOM-UA

BOOM-UA is a nonlinear integrated tool for both sonic boom prediction and aerodynamic performance analysis based on fully nonlinear CFD. This tool couples a three-dimensional solver for unstructured tetrahedral meshes to a CAD-based geometry kernel for efficient surface mesh regeneration, to the Centaur [59] mesh generation and adaption system, and to the PCBoom3 software (developed by Wyle [71] Associates) for far-field signature propagation and noise and loudness computation. Figure 3.1 shows the graphical flow chart for the BOOM-UA analysis procedure.

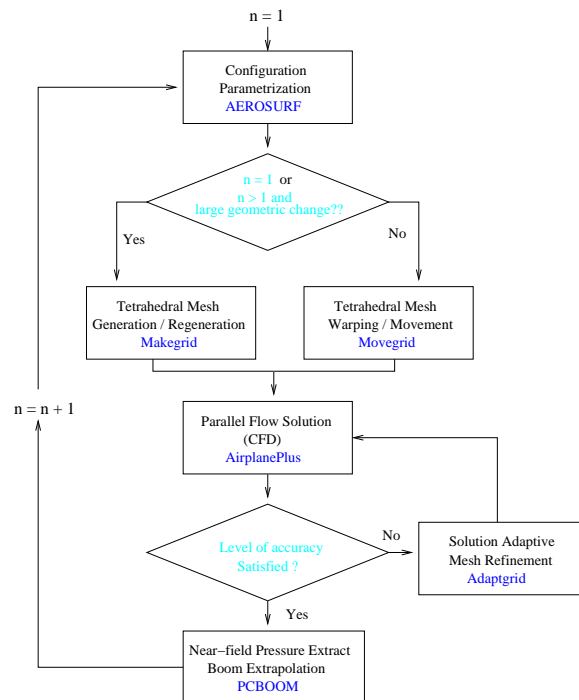


Figure 3.1: Schematic of the aerodynamic analysis tool, BOOM-UA

The unstructured adaptive mesh generation/perturbation/regeneration capability of BOOM-UA is based on the Centaur mesh generation family of tools [59]. Given the CAD definition of the geometry and a set of explicitly constructed far-field boundaries, Centaur uses an advancing-front method to generate both surface and volume meshes. Once a suitable mesh has been generated, the flow solution is carried out using the AirplanePlus solver [64] which uses an agglomeration multigrid strategy and MPI-based parallelization to solve the Euler and Reynolds-Averaged Navier-Stokes (RANS) equations on unstructured tetrahedral meshes. Although the software is able to solve the RANS equations, all calculations in this work have been carried out using the Euler equations since the phenomena that result in ground boom signatures (shock waves and expansions) are largely of an inviscid nature, and no regions of separated flow were observed in the experiments.

The flow solution follows several levels of solution-based isotropic adaption until the near-field signatures are deemed to be fully converged. Once such a solution is obtained, the near-field pressure signature is extracted and handed over to the PCBoom3 software which propagates it to the ground plane subject to a pre-specified flight altitude, atmospheric temperature profile, and horizontally stratified winds (if any, although none were used in this work). Although various ground boom noise loudness levels were available with proper rise time modifications, for the validation of BOOM-UA with experimental data, the perceived loudness (pLdB) of the ground signatures and the C-weighted noise level are used without the addition of a finite rise time. Later on in the design results, rise time modifications are indeed accounted for. For the SBJ configuration in question, the addition of the rise time modification is seen to simply shift the noise levels down by a constant increment.

The whole computation from geometry description to ground boom signature and ground boom noise level computation is fully automated as in Figure 3.1 so that optimization loops can be wrapped around the BOOM-UA system. Typical complete solution times (including all mesh generation and adaption) are on the order of 30 minutes using 16 processors of a Beowulf cluster made up of Athlon 2100XP processors for an adapted mesh with about $3 \sim 4$ million nodes.

3.1.1 Geometry Representation Using CAD/Capri/Aerosurf

High-fidelity MDO requires a consistent high-fidelity geometry representation. In general, the geometric shape of an aircraft can be defined by an appropriate parameterization of the geometry. This parametric geometry kernel is available to all of the participating disciplines in the design so that both cost functions and constraints can be computed using the same geometry representation.

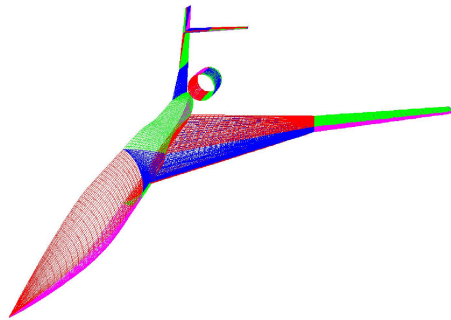


Figure 3.2: Geometry representation by parametric, CAD-interfaced AEROSURF

generates watertight surface geometry patches. AEROSURF can be executed in parallel and uses a distributed geometry server to expedite the generation of a large number of different design alternatives, thus reducing the cost of running geometry regenerations in the CAD package. Using a master/slave approach and PVM for distributed computing, arbitrary numbers of slaves can be started simultaneously while a master program maintains a queue of geometry regeneration requests and keeps slaves busy doing CAD re-generations. Figure 3.2 shows a representative aircraft with 46 surface patches which is generated directly in ProEngineer by providing the values of 108 design variables.

In our work, a CAD-based geometry kernel has been used to provide this underlying geometry representation. Baseline shapes has been developed in a CAD-package (ProEngineer, in our case) and constitute our parametric master model: they uniquely define the parameterization of a configuration given a particular design intent. Our geometry kernel (AEROSURF) is coupled with a parametric CAD description through the CAPRI interface of Haimes [61, 158, 137], such that it automatically gener-

3.1.2 Unstructured Tetrahedral Mesh Generation

In this thesis we focus on the use of unstructured tetrahedral meshes for the solution of the Euler equations around complete aircraft configurations. There are many methods available for the generation of tetrahedral meshes [54, 55, 56] and they are typically based on either advancing front or Delaunay triangulation ideas. In our work, an automatic advancing-front method is used for mesh generation. Advancing-front methods [57] involve the simultaneous generation of mesh points and their connectivity. The idea is to build the mesh element by element, adding new elements to previously generated ones, thus sweeping out a front across the entire domain. They usually rely on an explicitly defined element-size distribution function, which is most often constructed using a background grid [58]. The success of the advancing-front technique relies on the existence of a smoothly varying field function.

The Centaur software [59] has been used in this thesis work to construct meshes for all aircraft configurations and to enhance grid quality through automatic post processing and adaption. Only the fine meshes need to be explicitly constructed since our multigrid algorithm is based on the concept of agglomeration and, therefore, coarser meshes do not need to be generated directly. As mentioned above, Centaur is based on the advancing front model and consists of various different modules that are used by BOOM-UA.

The traditional approach to mesh generation using Centaur is an interactive one: a geometry import and preparation module (*setupgrid*) is used to retrieve the surface of the aircraft configuration (usually in IGES format). This geometry representation nearly always has to be cleaned up significantly within *setupgrid* before mesh generation can proceed due to imperfections in the imported geometry definition. Once the geometry is ready for mesh generation, a surface mesh generator (*makegrid*) is used to produce the initial surface mesh on which the volume mesh will be based. Note that the IGES geometry representation is retained in the form of analytic patches so that posterior mesh adaption is allowed to introduce nodes on the true surface of the configuration.

As mentioned above, the volume mesh is then constructed (with the same *makegrid* program) using the advancing front method. The mesh generation process includes

various procedures to ensure mesh quality, including mesh smoothing.

Once a complete mesh has been created, a flow solution can be computed and the features of this flow solution can be used to add/remove nodes and elements to/from the mesh. This process of isotropic mesh adaption is also carried out automatically by the Centaur module *adaptgrid*. The flow solution and mesh adaption procedures are repeated as many times as necessary until a converged flow solution is reached, or until the memory resources of the available supercomputer have been exhausted.

The process of generating a suitable mesh for sonic boom computation seems, at first, relatively user-involved. Since the requirement for user involvement can prevent the full automation of the whole BOOM-UA process (which is absolutely necessary for design) we have taken steps to ensure that no user interaction is necessary for repeated evaluation of multiple variations of a baseline configuration. This automation is not fundamental to the work presented in this section, but is essential for the design efforts that will be presented in later sections.

For this purpose, we can create parametric aircraft models [60] which can be easily regenerated when any of the shape parameters is altered. The regeneration of this CAD parametric model is driven by the CAPRI API of Haines [62]. Once a new geometry has been constructed, the necessary information can be generated to automatically construct a volume mesh using the Centaur software modules described above and, possibly, a mesh perturbation module called *perturbgrid*. The CAPRI CAD interface also has the capability of generating surface triangulations of high quality that can be used in lieu of the ones generated internally by Centaur [63].

Figure 3.3 shows a typical triangular surface mesh around a proposed NASA supersonic business jet (SBJ) configuration, which is the subject of the validation studies discussed in Section 3.2. The figure contains only the triangles on the surface of the aircraft and it has been substantially coarsened for visualization purposes. Notice that the sting used for the wind-tunnel test has also been gridded.

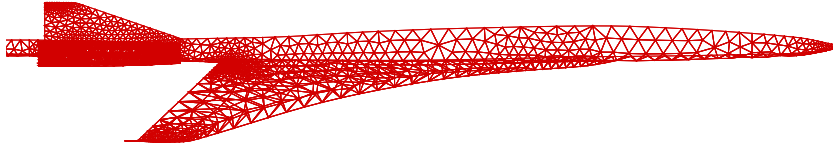


Figure 3.3: Surface mesh for NASA SBJ configuration

3.1.3 Unstructured Flow Solver and Solution Approach: AirplanePlus

The three-dimensional AirplanePlus flow solver of van der Weide [64] is used in this thesis. AirplanePlus is a C++ implementation of the original AIRPLANE flow solver of Jameson [65] developed by van der Weide at EADS in Munich. AirplanePlus contains substantial enhancements to the baseline algorithm including the agglomeration multigrid strategy, parallelization (of both the solver and pre-processor), load balancing algorithm, and the solution of the Reynolds-Averaged Navier-Stokes (RANS) equations.

An edge-based discretization is used to minimize the computational and memory requirements of the solver. The usual 4-stage Runge-Kutta method is modified with appropriately tailored coefficients to speed up the convergence rate by allowing high CFL numbers, aided by multigrid, residual smoothing and enthalpy damping for better convergence properties. Several options for artificial dissipation and the block-Jacobi preconditioning method are all available in the solver and can be used as needed.

An efficient, MPI-based, parallelization has been shown to produce linear scalability up to 32 processors in even small meshes with around 600,000 nodes. For the type of calculations that we have done in this work, much larger meshes are required and, therefore, our flow solver could scale linearly up to more than 512 processors. Typical calculations for this work have been run using 16 or 32 processors and therefore, near-linear scalability was obtained. The number of processors used was only limited by the availability of additional computational resources.

AirplanePlus has been validated on a number of configurations during its earlier use at EADS and was used to calculate accurate near-field pressure distributions for each of three configurations in this section. In addition, the flow solver from which it derives, AIRPLANE, has also undergone substantial validation studies over the years. Figures 3.8, 3.9 and 3.10 show the surface pressure distributions obtained by the AirplanePlus flow solver on each of the three configurations of interest in this section. Notice that each successive set of figures presents the configuration with fewer components (nacelles and empennage) removed. The accuracy of the flow solutions can be seen in the level of detail present in the shock structure caused by the presence of the nacelles and diverters in the aft portion of the geometry.

Again, it must be noted that all the calculations in this section have been made using the Euler equations since they are suitable to the physical phenomena we are trying to predict here. However, neither the mesh generation/adaption procedure, nor the flow solver, are limited to the Euler equations: the Reynolds-Averaged Navier-Stokes equations could also be solved at additional expense due to the increased mesh size requirements resulting from the resolution of boundary layers, shear layers, and wakes.

3.1.4 Solution-adaptive Mesh Refinement

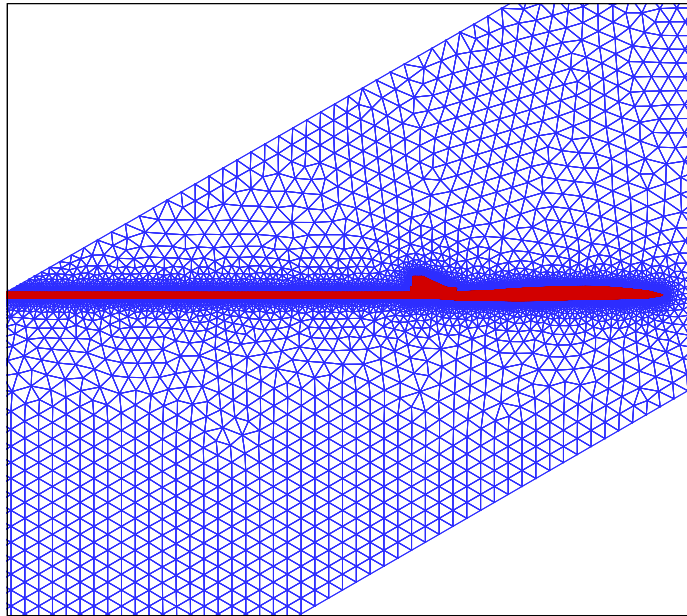
Once an initial solution has been computed on a tetrahedral mesh, the grid needs to be locally adapted to better capture specific features with higher accuracy at lower cost (than that obtained with either multiblock structured approaches [92] or uniform refinement of the grid.) This can be achieved through an improved distribution of grid points for each computed solution [66, 67, 68]: unstructured tetrahedral elements are well suited for cell adaption. For the cases that we have studied, coarsening has only a minor performance benefit in steady-state calculations and was omitted.

The adaption procedure utilizes h-refinement or subdivision techniques. For each edge that is flagged by the error estimation technique, new mesh nodes are inserted at the midpoint. For boundary edges, these points are repositioned onto the spline patch

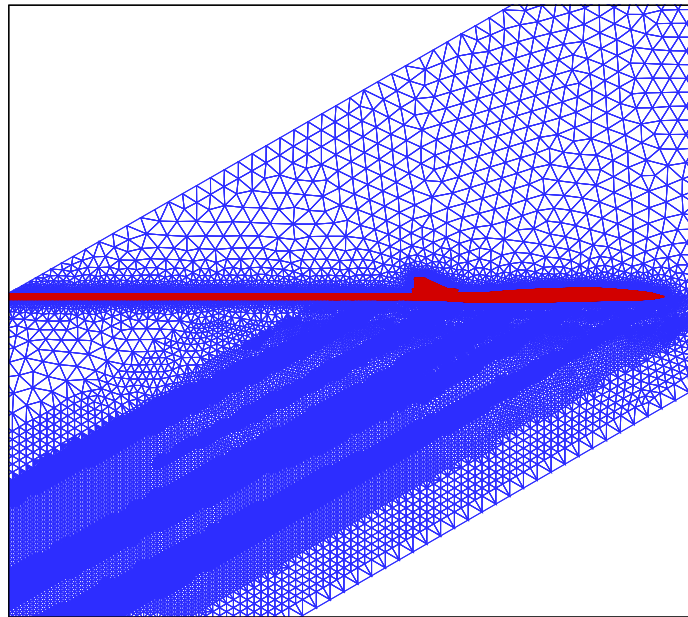
surfaces which define the original geometry from the CAD package. The current post-adaption grid-improvement scheme employs face and edge swapping. Undesirable shape measures are investigated and new local tetrahedra configurations with more desirable shape measures are selected.

The adaption procedure is, of course, recursive, and it proceeds until a certain level of error has been achieved or a maximum number of refinement levels have been accomplished. Figure 3.4 below shows the initial mesh around the configuration before any adaption has taken place. The selection of the initial mesh resolution is important to capture the underlying pressure gradients which will later be enhanced in the adapted meshes. Since the presence of shock waves and expansions are the driving features to be captured in this study and since the average shock angle is relatively predictable, our approach consists of performing two uniform local adaptations (mainly in the region under the aircraft) followed by several cycles (typically two or three) of solution-based adaption. Note that in the current study we are only interested in the effect of the primary boom carpet, and, therefore, no attempt is made to capture the shock waves that emanate from the upper surface of the configuration (which may be refracted down to the ground due to atmospheric effects.) Figure 3.4 shows the solution-adapted mesh after three adaption steps. Typically, four or five consecutive adaption cycles are performed automatically (starting with the initial mesh) to reach the necessary solution quality. These meshes become too fine for display purposes, but exhibit the same features represented in Figure 3.4.

An appropriate choice of refinement criterion is very important to capture desired flow features and to obtain higher solution accuracy. The most popular refinement options for fluid-flow problems are heuristically-derived gradient-based criteria, which involve a single or multiple physical flow variables. The gradient of pressure can be used to identify inviscid flow features. But in sonic boom prediction problems the pressure gradient in the near-field is as important as in the neighborhood of the aircraft. In addition, the direction of the gradient should be taken into account as well. In this study, a pre-specified range of velocity gradient magnitudes which are projected onto the direction of the local pressure gradient work successfully to predict shock locations and to capture small pressure gradients in near-field. Since the initial



(a) Original mesh without adaptation. Mesh nodes=607,787



(b) Mesh after three adaptations with mesh nodes=1,893,110

Figure 3.4: Mesh adaptation process

mesh resolution is essential to capture the presence of the small pressure gradients in the near-field, an initial mesh that is too coarse is avoided. In addition, the initial steps of local uniform refinement underneath the aircraft are helpful to resolve the final solution with highest accuracy. The initial uniform refinements were done in an area under the aircraft that is between the Mach cones of the initial and final shock waves of the fuselage of the configuration (the initial portion of the sting is also included.)

Our adaption criteria is based on the local value of an adaption function (ϵ or ϵ') and a prescribed region of space that is eligible for adaption. If the value of the function is higher than a specified threshold value ($\epsilon = 10^{-4}$ has been used in our calculations) and the edge to be adapted is within the allowable region, the mesh is subdivided. Initially, we had focused on the following expression to represent a good indicator of the need to adapt for sonic boom computation, where \mathbf{V} is the velocity vector, c is local speed of sound and Δx is a local mesh length scale:

$$\epsilon' = \frac{\mathbf{V}}{c} \cdot \frac{\nabla p}{|\nabla p|}. \quad (3.1)$$

However, experiments [69] by other investigators indicate that the modification of the previous equation to include a local mesh length scale such as:

$$\epsilon = \frac{\mathbf{V}}{c} \cdot \frac{\nabla p}{|\nabla p|} \Delta x \quad (3.2)$$

produces a more effective refinement criterion. This is partially due to the fact that while the simple gradient-based criteria decreases in magnitude as the mesh is refined in smooth regions of flow, it remains approximately constant in the vicinity of shock waves, since the shock wave profile steepens as the mesh is refined, and the jumps remain almost constant. However, even in regions of smooth flow, the additional length scale (in the ϵ measure) weights larger ones more heavily than small cells, and drives the adaption process closer toward global refinement. In all of our computations, we have used the ϵ criterion for adaption using Centaur's *adaptgrid*.

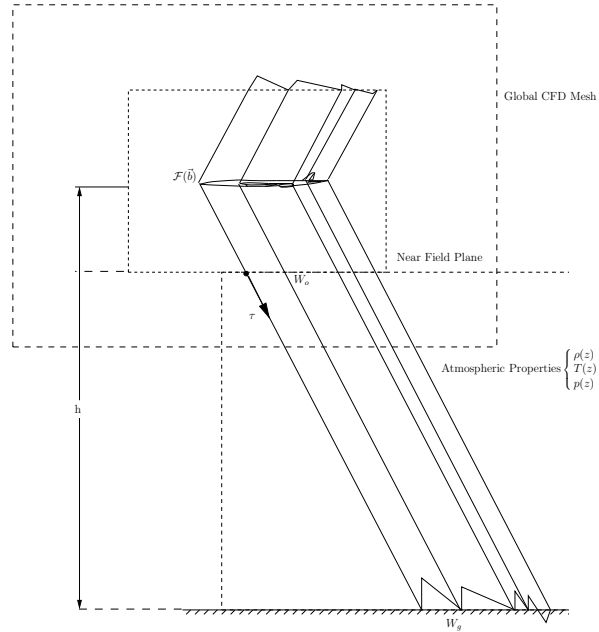


Figure 3.5: Schematic of Sonic Boom Minimization Setup with Nomenclature.

3.1.5 Near-field Pressure Extraction

The basic strategy for the computation of ground boom signatures can be seen in Figure 3.5 below. A solution adaptive mesh using the criteria described above is constructed around the aircraft. It extends a certain distance away from it, but not to the ground plane as it would be computationally prohibitive to do so with appropriate resolution from the cruise altitude. At the near-field plane location, the pressure signature created by the aircraft is extracted, and it is propagated down to the ground using extrapolation methods based on geometric acoustics.

The far-field boundaries of the CFD mesh must be located close enough so that the resulting mesh size is computationally manageable, but, at the same time, they must be located far enough so that the near-field flow field is axisymmetric and there are no remaining diffraction effects which cannot be handled by the extrapolation schemes. This fact embodies one of the fundamental difficulties of the computation of accurate sonic boom signatures: the near-field must be taken sufficiently far away

for the aircraft and there must be adequate mesh resolution so that the near-field signatures are properly captured. It must be noted that more refined procedures for signature propagation that allow the near-field signature to be taken closer to the aircraft have been developed [70] but were not available for this thesis work.

In this study, the pressure field at the symmetry plane 0.59, 0.75 and 1.125 body lengths below the fuselage centerline, is obtained and provided as an initial condition to the boom extrapolation software. The pressure extraction algorithm (for the unstructured tetrahedral mesh) is based on advanced octree data structures and therefore incurs very little computational cost.

In this study, we have used both the Sboom [35] and PCBoom3 [71] extrapolation methods inside the BOOM-UA to convert near-field signatures into ground booms. Although the PCBoom3 software is far more capable than Sboom, we have only computed ground booms created by the aircraft in a steady-state cruise condition and, therefore, both codes are nearly equivalent. If ground booms caused by maneuvering aircraft were to be computed, the capabilities of the PCBoom3 software would have to be used.

Although the capability of extracting the signature on a cylinder around the aircraft is available in BOOM-UA, in this study we have chosen to extract and propagate information only under the flight track, since experimental near-field pressure data was only available on the symmetry plane.

Earlier research on low-boom aircraft design was mainly focused on the reduction of the magnitude of only the initial peak of the ground boom signature [51]. This requirement, which had been suggested as the goal of the DARPA-sponsored Quiet Supersonic Platform (QSP) program ($\Delta p_0 < 0.3$ psf), hides the importance of the rest of the signature, which often arises from the more geometrically complex aft portion of the aircraft where empennage and engine nacelles and diverters create more complicated flow patterns. Moreover, such designs often have two shock waves very closely following each other in the front portion of the signature [52, 31], a behavior that is not robust and is therefore undesirable.

For this reason, we have chosen to make comparisons based on the perceived loudness of the complete signature. In addition to computing the perceived loudness,

another weighting, which is useful in estimating the attenuated noise when personal hearing protectors are used, the C-weighted sound level, is also obtained and compared with the perceived loudness.

3.2 Validation: Comparison of Wind-tunnel Data

3.2.1 Configurations of Interest

We now focus our studies on a supersonic business jet (SBJ) configuration that was tested in the Langley Unitary Plan Wind Tunnel (UPWT), and which was used to extract near-field pressure information at various distances from the aircraft model. Variations of the baseline configuration are created by the removal of the nacelles and vertical tail in order to investigate their effect on both the near-field pressure distributions and the ground boom signature.

The original configuration was developed by R. J. Mack and was tested by Wilcox and Coen [72] and consists of a wing with large outboard dihedral/winglet, fuselage, vertical tail, and aft-fuselage mounted nacelles with diverters attached to the fuselage. They also tested a second configuration (proprietary to the Lockheed Martin company), but neither the geometry nor the results were available for comparisons. Therefore this configuration was not used in this study. The top, front, side and perspective views of the configuration as analyzed (including the rear sting mount) can be seen in Figure 3.6. More details of the experimental model and the testing procedure can be found in reference [72].

For purposes of computing the ground boom signatures, the wind-tunnel models were scaled up by a factor of 100 (as suggested by the wind-tunnel test report) and were flown at a (somewhat arbitrarily chosen) cruising altitude of 50,000 ft on a U.S. Standard Atmosphere with no winds. For a target lift coefficient $C_L = 0.1$ based on a scaled reference area of $S_{ref} = 1560 \text{ ft}^2$ these conditions result in an aircraft cruise weight of 105,790 lbs. The model length is 16 in without the sting and 42 in with the sting included. The case with nacelles included uses what are referred to as *big nacelles* in the wind-tunnel report.

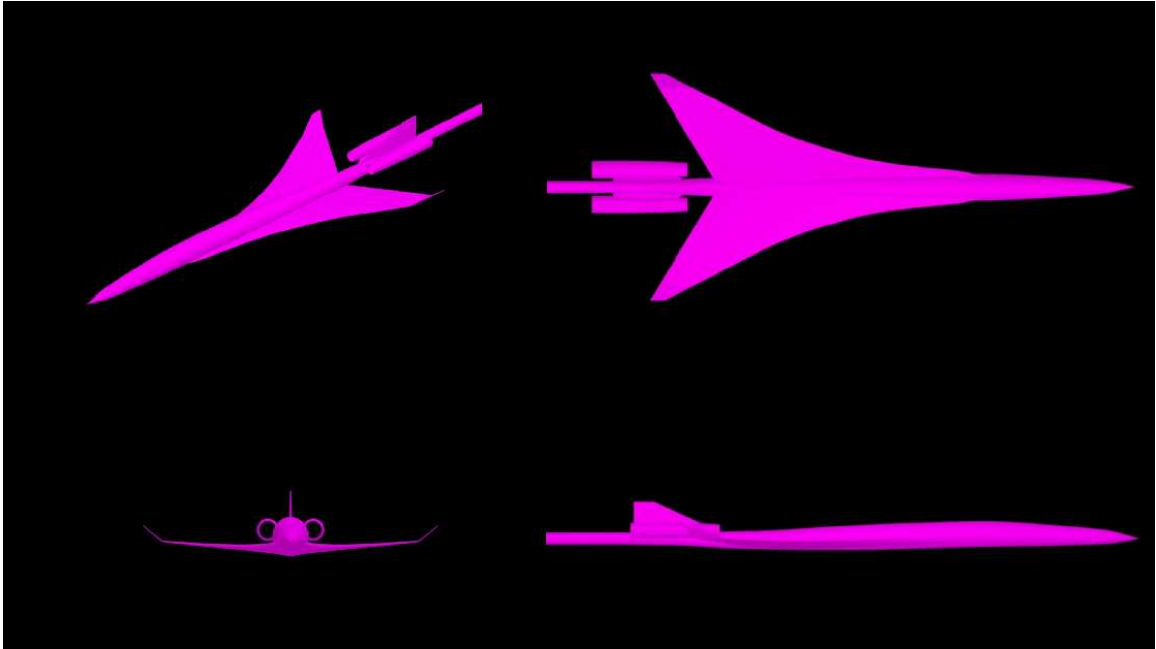


Figure 3.6: Three-View drawing of NASA SBJ configuration.

BOOM-UA is applied to all three configurations to extract the near-field overpressures and to predict accurate ground boom signatures. The near-field overpressures are extracted at three distances from the aircraft model (9.5in, 12 in, and 16 in) corresponding to the locations where experimental data was taken. This allows us to compare the CFD predictions directly with experiment and to compute ground signatures extrapolated from these distances. In theory, if all three pressure signatures were sufficiently far from the aircraft the computed ground boom signatures would fall on top of each other. As will be shown later, this is not the case, although the differences in both the ground boom signatures and the perceived loudness are relatively small.

3.2.2 Experimental Conditions

The wind tunnel test was conducted in the Langley Unitary Plan Wind Tunnel (UPWT) which is a continuous flow, variable pressure supersonic wind tunnel. The tunnel contains two test sections which are approximately 4 ft² and 7 ft long. The

Mach number for the relevant experiments was set 2.0, while Reynolds number was 2.0×10^6 per ft.

The model and sting combination were pinned together and connected to an angle of attack mechanism and tunnel model support system. The angle of attack mechanism was used to vary the model angle of attack and the tunnel model support system had the capability to move the model longitudinally and laterally within the test section so that near-field pressure signatures could be extracted at varying distances from the model. The survey and reference probes were mounted on a track to measure the difference between the static pressure of each probe. The near-field pressure was measured at three different locations for each configuration with different angles of attack.

Figure 3.7 below is reproduced from the experimental report [72] and shows a brief view of the experimental model mounted in the wind tunnel.



Figure 3.7: View of the model mounted in the wind tunnel. From [72]

3.2.3 Solvers and Flow Conditions

BOOM-UA was used to simulate the results from the wind-tunnel experiments. As mentioned earlier, the flow solver portion of BOOM-UA was used in inviscid mode only. In all of these computations, small discrepancies may therefore exist due to the lack of viscous effects, although these discrepancies are expected to be small, as viscosity only plays a minor role in the generation of the pressure signatures that we are interested in.

In addition, the angle of attack was set to match the experimental values for each of the configurations and varies from 2.54° to 2.89° . No attempt was made to match the experimental lift coefficients exactly. As expected, the computed lift coefficients (at the matched angles of attack) are approximately 1% higher than the experimental values obtained. The lift coefficients are very close to $C_L = 0.1$ in all cases. As mentioned earlier the cruising altitude is set at 50,000 ft.

3.2.4 Results

Pressure Distributions vs. Mesh Resolution

In order to assess the mesh resolution requirements for accurate near-field signature extraction, solution-adaptive computations were carried out for each of the three configurations in question (c1 = full configuration, c2 = configuration without nacelles, c3 = configuration without nacelles and tail). For each of these configurations, 5 flow solutions and 4 adaption cycles were carried out starting from relatively fine initial meshes.

Table 3.1 shows the number of mesh nodes in each mesh, for each adaption cycle, and for each configuration (c1 through c3.) As mentioned earlier, the resolution of the initial mesh is very important to ultimately capture all of the phenomena we intend to observe. This is particularly true of the small pressure gradients in the near field (compared to those in a close neighborhood of the body) which tend to be missed if the initial mesh resolution is not sufficiently fine (the adaption criterion explained before focuses on the flow features near the aircraft and disregards the near-field flow features.) For this reason, all initial meshes contained between 500,000 and 600,000

nodes. The first two levels of adaption are purely geometric and simply add mesh nodes in the area between the expected location of the front and rear shocks of the configuration. The third and fourth adaption cycles are solution-based.

After four adaption cycles and five flow solutions, it can be seen from Figures 3.11, 3.12, and 3.13 that the near-field pressure distributions appear to have converged. In the case of the configuration without nacelles and tail (c3) a further attempt to an additional adaption level failed due to *adaptgrid* exceeding the memory resources of our Origin300 computer (16 Gbytes maximum). Note that all of the final meshes, whose solutions will be used for experimental comparison, have between 7×10^6 and 8×10^6 nodes. This large number of nodes is necessary to obtain reasonable comparisons that capture all of the flow features of the experiment. This mesh size (on an adaptive mesh) is in contrast with our earlier work (using multiblock structured meshes which had been biased along the direction of the front and rear shocks) which used on the order of 3×10^6 nodes.

	Initial	1 st adpt	2 nd adpt	3 rd adpt	4 th adpt
c1	607,787	690,239	933,192	2,749,606	7,698,731
c2	543,201	591,056	854,781	2,737,821	7,973,972
c3	523,954	572,467	838,612	2,736,989	8,100,624

Table 3.1: Number of mesh nodes through all the adaption cycles

Figures 3.11 through 3.13 show the evolution of the near-field pressure distributions through the various adaption cycles for all three configurations. For each configuration, we present computational results for each of the three near-field distances at which (at least for the complete configuration) data was taken in the wind tunnel. The locations at which computational data was collected are lines on the symmetry plane located at distances of $r = 9.5$ in, $r = 12$ in, and $r = 18$ in under the aircraft. As expected, the finest mesh for each configuration resolves the pressure signatures with most detail: the pressure rise across the shock is largest at each location and some of the minor features of the signature are present, while for the coarser meshes these do not appear.

The differences in the near-field pressure distributions of all three configurations are obvious in the Figures. The front portion of the signatures are almost identical as nothing has changed in the geometry in that area and the removal of the tail and nacelle are unable to affect the pressure distributions upstream in a supersonic flow. The rear portion of the signature is rather different. The omission of the nacelles results in a sharp decrease in strength of second-to-last shock in the distribution. This can be appreciated from Figures 3.8 and 3.9 where the complex system of shock waves in the aft portion of the fuselage has disappeared. The effect of the removal of the tail (see Figure 3.10) is not as dramatic, but does cause an alteration in the pressure signature: the strength of the last shock wave in the signature is reduced to a $|\Delta p/p| < 0.02$.

Note that the pressure distributions that result from the mesh after three adaption cycles (with around 3×10^6 nodes do not necessarily capture all the details of the signature and certainly miss the peak values of all of the shocks in the signature. From these observations we conclude that tetrahedral unstructured adaptive meshes in the neighborhood of 10×10^6 nodes are necessary to ensure that the near-field pressure signatures are computed without numerical error. Ultimately, what matters most to a designer is not the level of error in the near-field pressure signature, but the resulting errors once the near-field signature has been propagated to the ground. As we will see later on, due to the process of shock coalescence (as the signature ages) if the ground boom has an N-wave character, the need for the absolutely highest resolution in the near field may not be justified. However, for cases where the signature is such that it is *shaped* the resolution we have discussed here is needed.

3.2.5 Comparison of Near-field Pressures with Experimental Data

From the results of the mesh resolution study, the solution from the finest mesh (after four or five solution adaptive refinements) was chosen for comparison with the near-field pressures obtained in the wind tunnel. These comparisons are presented in Figures 3.14 to 3.16 . Note that for the cases without nacelles and tail, experimental

data was not collected at the $r = 12$ in location and, therefore, a direct comparison is not available. Note also that since the reference pressure during the experimental runs was not necessarily p_∞ , the signatures do not start and end at values of $\Delta p/p = 0$. For this reason, the experimental signatures have been biased (no scaling applied) in such a way that $\Delta p/p = 0$ was obtained at the front and rear of the signatures.

In general, good agreement between the experiment and computations is found, despite the fact that all computations were carried out using the Euler equations and viscous effects were neglected. Furthermore, the reader is reminded that all computations were carried out at the experimentally determined angle of attack (no attempt to match C_L was made.) In addition, the computations simulated the aircraft embedded in a free stream and did not enclose the model within the wind-tunnel walls.

The number and magnitude of all pressure peaks in the experimental near-field signatures are captured by the simulations for all three configurations. Some small details in the aft portion of the signatures, particularly for the configuration without nacelles and without tail are missing from the computations, however, denoting that an initially finer mesh in the back end of the aircraft may be necessary for the adaption procedure to capture these features. However, these features have very small magnitude and are absorbed by the aging of the signature as it propagates down to the ground.

There is a slight tendency to overpredict the absolute length of the signature (from initial to final shock) in comparison with the experiment, which indicates that either the angles of the leading and trailing shocks were not predicted exactly, or that the effect of the expansions on the shock angles in the near field were slightly off. Again, these slight discrepancies do not appear to translate into significant ground perceived loudness changes as we will see later.

Some of these effects can be seen in the symmetry-plane pressure plots shown for all three configurations in Figure 3.17. The effects of both the nacelles and tail on the near-field pressure can be seen by comparing the three symmetry-plane pressure plots. The shocks that emanate from the tail region in the cases without nacelles and/or tail weaken considerably in comparison with the wave pattern present for the full configuration.

3.2.6 Ground Boom Signature and Weighted Sound Levels

Finally, in this section we present the results of the propagation of both computed and experimentally-determined near-field signatures to the ground. As mentioned earlier, the wind-tunnel model was scaled up by a factor of 100 for the full-scale aircraft. In addition, the cruise altitude for the full-scale aircraft was chosen to be 50,000 ft, and a Standard US Atmosphere with no winds was setup for propagation purposes. The cutoff angle for acoustic disturbances that reach the ground turns out to be $\pm 54^\circ$, although only signatures underneath the flight track are considered here. All ground boom signatures are computed using the PCBoom3 software.

The ground boom signatures obtained starting from both experimental and computational near-field pressure distributions are presented in Figures 3.18, 3.19 and 3.20. From these Figures we can see that the ground signatures for these configurations result in pressure distributions that are very close to an N-Wave, except for the fact that a small shock persists in the middle of the signature (that has not yet been absorbed by either the front or rear shocks.) The computationally determined signatures exhibit an additional shock (in the front of the signature) that is not present in the experimentally derived ground booms: it appears that the small differences in the computational and experimental near-field pressure (after the initial pressure rise) are such that they are delaying the final coalescence of the front two shocks (when compared to the experimental results). Additional propagations of the same computational signatures from 55,000 ft show a fully coalesced front shock.

The differences in character between the computational and experimental ground boom signatures are not very large. In fact, in this case where the ground signature is nearly an N-wave, even the coarser meshes result in ground signatures that match the shape of the experiment well. The most obvious trend, however, is that as the number of mesh adaption levels is increased, the peak overpressures in the ground signatures increase, sometimes by up to 20%. These peak overpressures are consistently 5-7% lower than the experiment. Therefore, in order to predict the actual values of the peak overpressures, it is necessary to use the finest meshes in the sequence, if not even slightly finer. Figures 3.18, 3.19 and 3.20 show the results of boom propagation for near-field pressure from experiment and from computations after one and five

adaption cycles in order to highlight the differences that derive from the use of much smaller meshes.

A more quantitative measure of the differences in the ground booms is presented below. Both C-weighted sound level (a measure that is useful to determine human perceived noise when wearing protective equipment) and perceived loudness were calculated for both the computations and experiments. Tables 3.2, 3.3 and 3.4 show the two sound level representations for the boom signature derived from the experimental near-field data. Each table corresponds to each of the different configurations studied in this work. The errors in the two sound level representations between ground signatures obtained from the finest meshes and from experimental data are shown in Tables 3.5, 3.6 and 3.7. For all three configurations and at all three different near-field locations, the sound levels of the propagated ground boom produce only small errors. In fact, the average error is around 2% for the dBC weighting, and slightly larger (around 3.5%) for the perceived loudness.

Given the good agreement in the near-field pressure signatures and the acceptably small errors in the ground boom loudness, it can be concluded that BOOM-UA can be used for a design work with satisfactory accuracy and validity. Relatively fine meshes (> 8 million nodes) may be needed to obtain ground boom shapes and intensities that closely resemble the experiment. However in the case of N waves, it was shown that coarser meshes can be tolerated, and $3 \sim 4$ million node meshes can be used in later design work.

location	C-weighted level (dBC)	perceived loudness (pldB)
r=9.5	101.60	95.70
r=12	101.80	96.15
r=18	102.25	95.46

Table 3.2: C-weighted sound level and perceived loudness from experimental data. Complete configuration.

location	C-weighted level (dBC)	perceived loudness (pldB)
r=9.5	100.27	93.38
r=18	100.78	91.87

Table 3.3: C-weighted sound level and perceived loudness from experimental data. Configuration without nacelles.

location	C-weighted level (dBC)	perceived loudness (pldB)
r=9.5	99.96	93.55
r=18	100.57	93.58

Table 3.4: C-weighted sound level and perceived loudness from experimental data. Configuration without nacelles and tail.

location	C-weighted level (%)	perceived loudness (%)
r=9.5	1.9587	4.1152
r=12	1.9205	3.7600
r=18	1.9810	5.0030

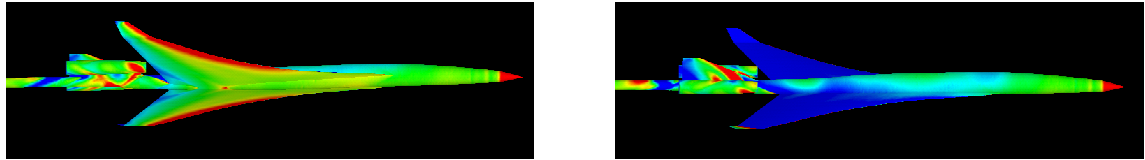
Table 3.5: Error in C-weighted sound level and perceived loudness between experiment and computation. Complete configuration.

location	C-weighted level (%)	perceived loudness (%)
r=9.5	2.4038	5.4846
r=18	2.3016	7.3211

Table 3.6: Error in C-weighted sound level and perceived loudness between experiment and computation. Configuration without nacelles.

location	C-weighted level (%)	perceived loudness (%)
r=9.5	1.2558	0.2642
r=18	2.1959	5.0967

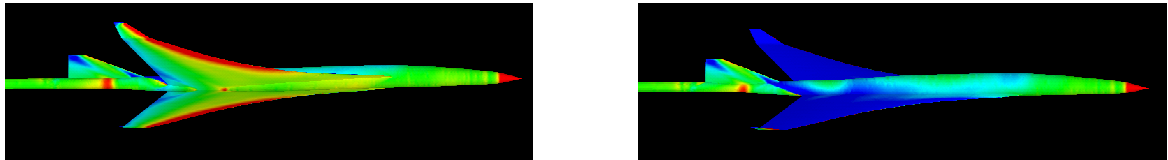
Table 3.7: Error in C-weighted sound level and perceived loudness between experiment and computation. Configuration without nacelles and tail.



(a) Lower surface.

(b) Upper surface.

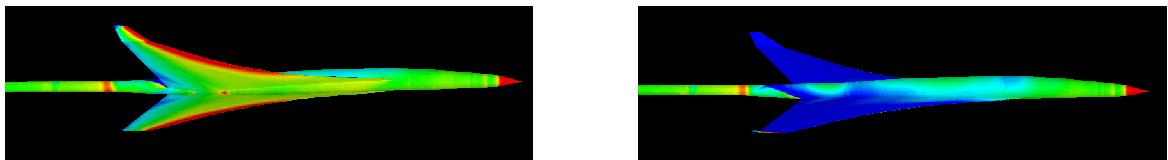
Figure 3.8: Surface pressure distributions: complete configuration SBJ.



(a) Lower surface.

(b) Upper surface.

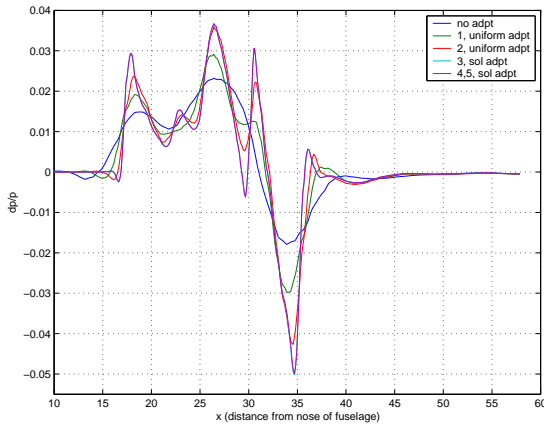
Figure 3.9: Surface pressure distributions: SBJ without nacelles.



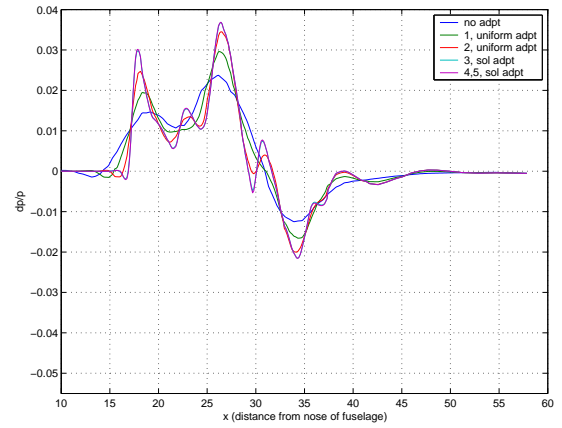
(a) Lower surface.

(b) Upper surface.

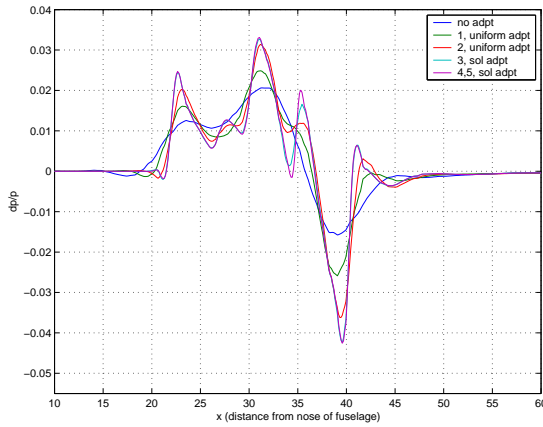
Figure 3.10: Surface pressure distributions: SBJ without nacelles and empennage.



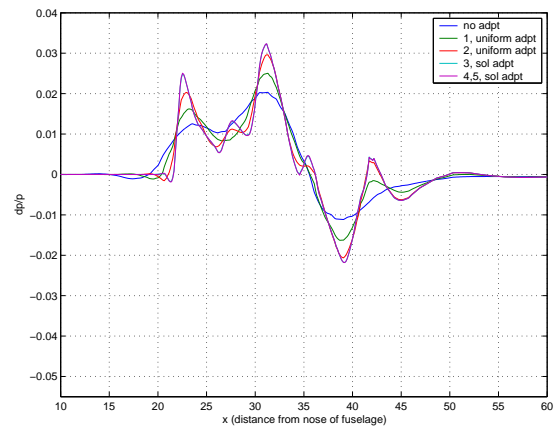
(a) Pressure distribution at $r=9.5$ in



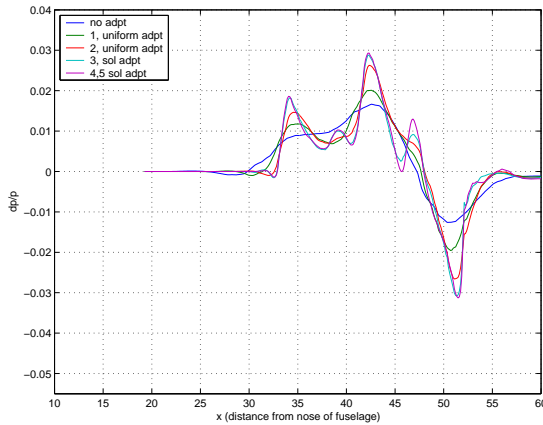
(a) Pressure distribution at $r=9.5$ in



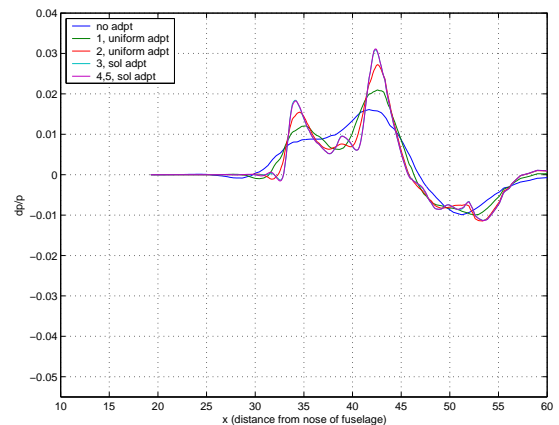
(b) Pressure distribution at $r=12$ in



(b) Pressure distribution at $r=12$ in



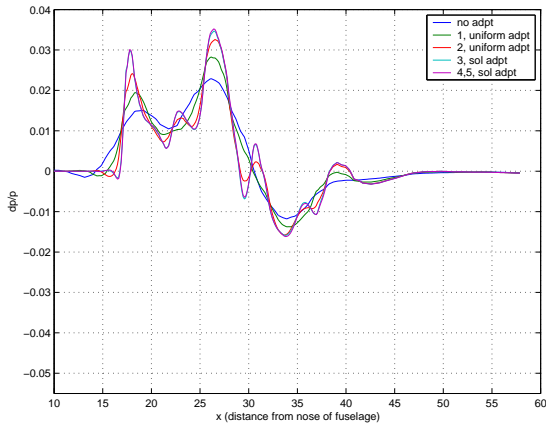
(c) Pressure distribution at $r=18$ in



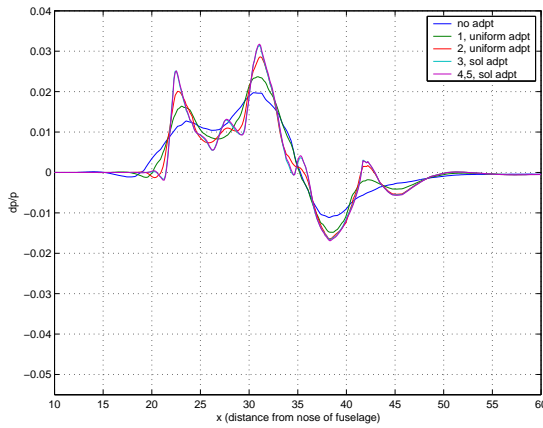
(c) Pressure distribution at $r=18$ in

Figure 3.11: Near-field pressure distributions for all adaption cycles. Complete configuration.

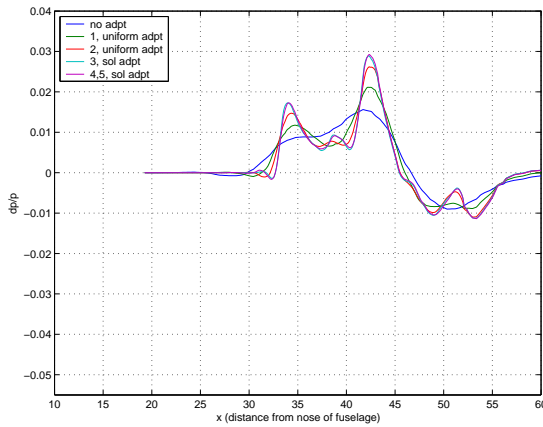
Figure 3.12: Near-field pressure distributions for all adaption cycles. Configuration without nacelles.



(a) Pressure distribution at $r=9.5$ in

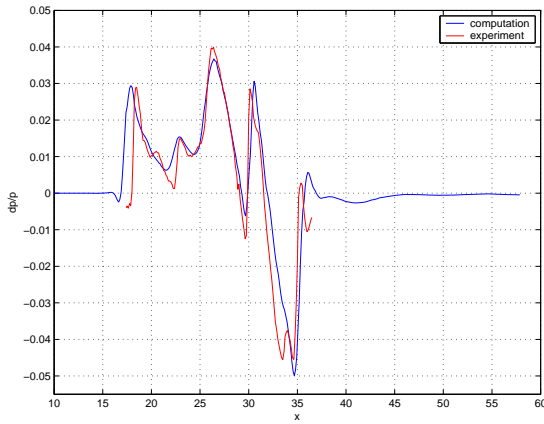


(b) Pressure distribution at $r=12$ in

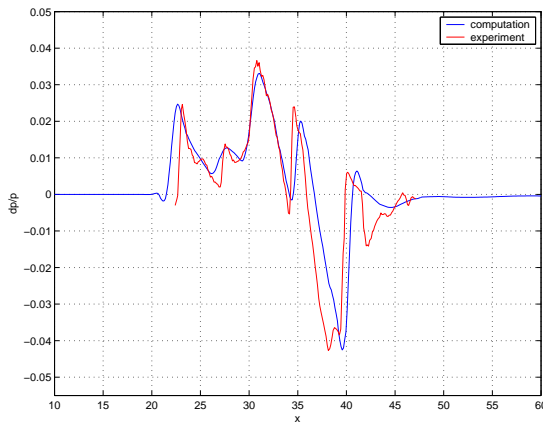


(c) Pressure distribution at $r=18$ in

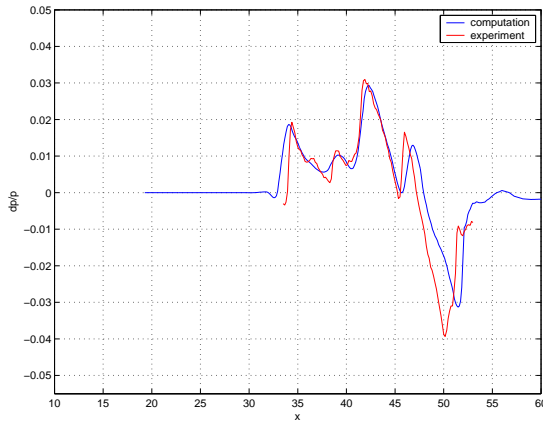
Figure 3.13: Near-field pressure distributions for all adaption cycles. Configuration without nacelles and tail.



(a) Pressure distribution at $r=9.5$ in

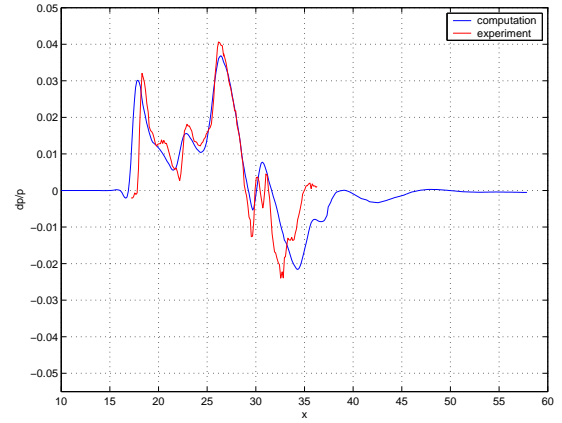


(b) Pressure distribution at $r=12$ in

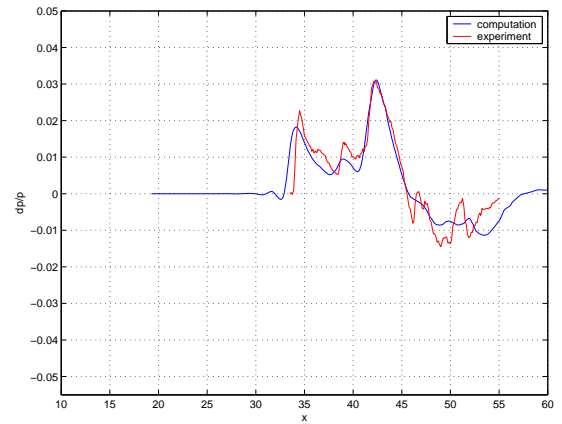


(c) Pressure distribution at $r=18$ in

Figure 3.14: Comparison of near-field pressure with experiments. Complete configuration.

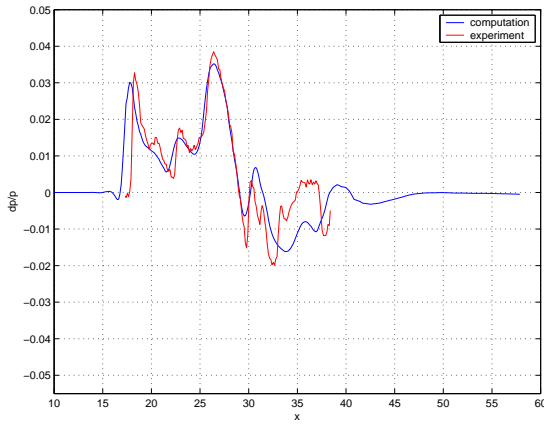


(a) Pressure distribution at $r=9.5$ in

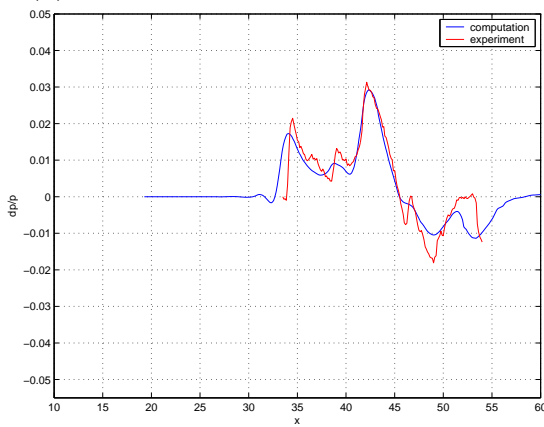


(b) Pressure distribution at $r=18$ in

Figure 3.15: Comparison of near-field pressure with experiments. Configuration without nacelles.

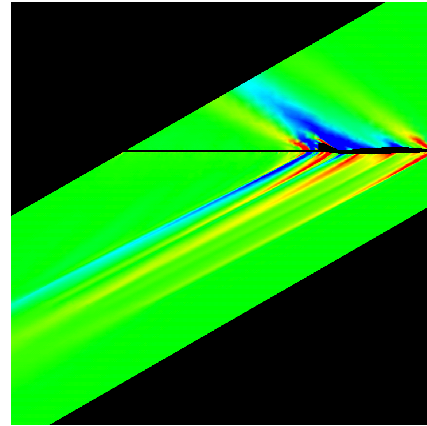


(a) Pressure distribution at $r=9.5$ in

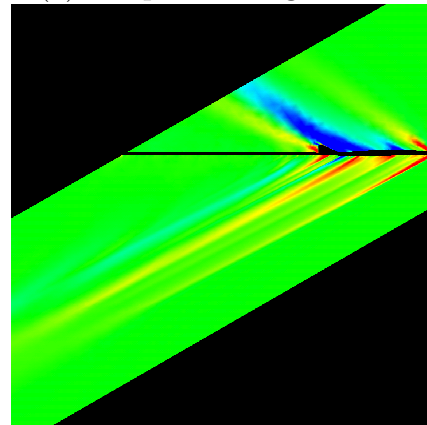


(b) Pressure distribution at $r=18$ in

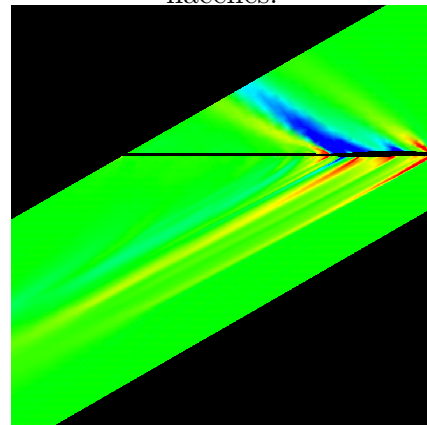
Figure 3.16: Comparison of near-field pressure with experiments. Configuration without nacelles and tail.



(a) complete configuration.

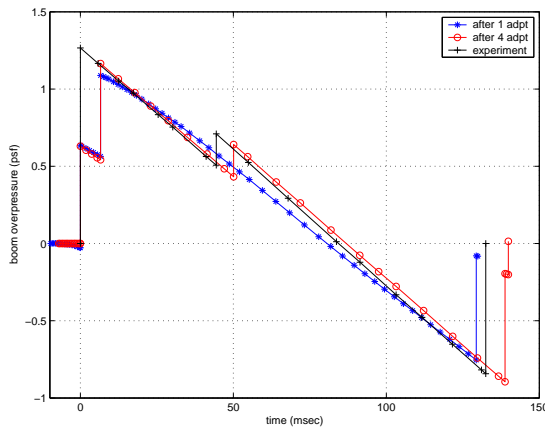


(b) configuration without nacelles.

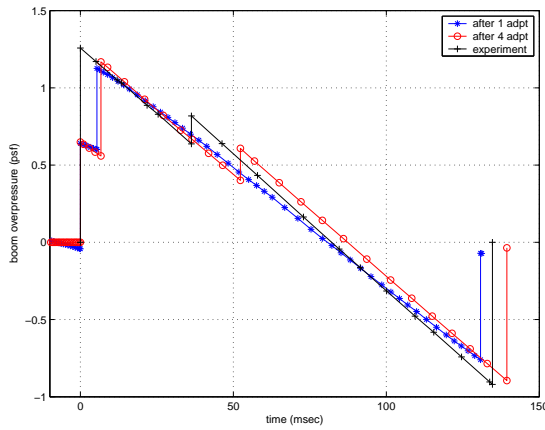


(c) configuration without nacelles and tail.

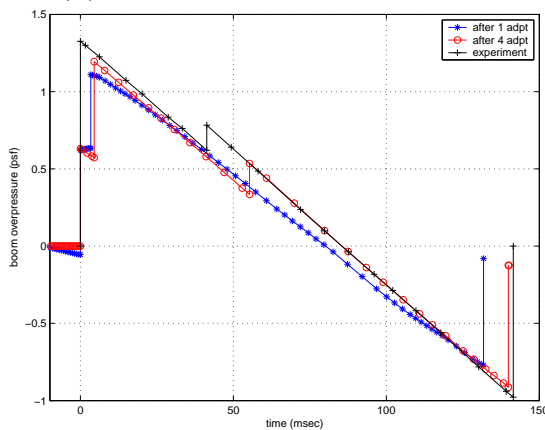
Figure 3.17: Plot of near-field pressure distributions along symmetry plane.



(a) Ground boom from $r=9.5$ in.

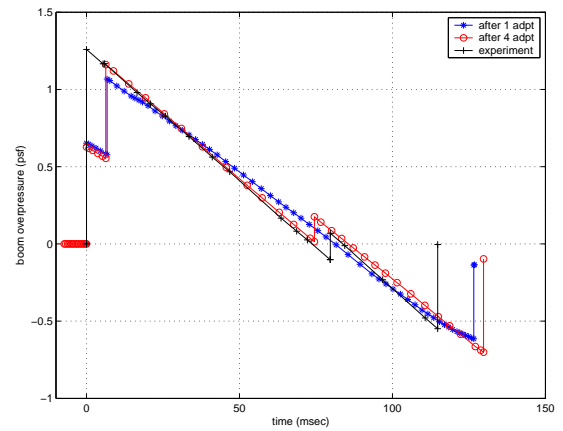


(b) Ground boom from $r=12$ in.

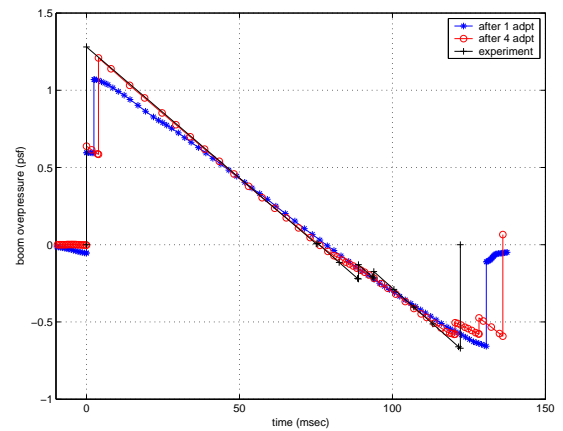


(c) Ground boom from $r=18$ in.

Figure 3.18: Ground boom comparisons. Complete configuration.

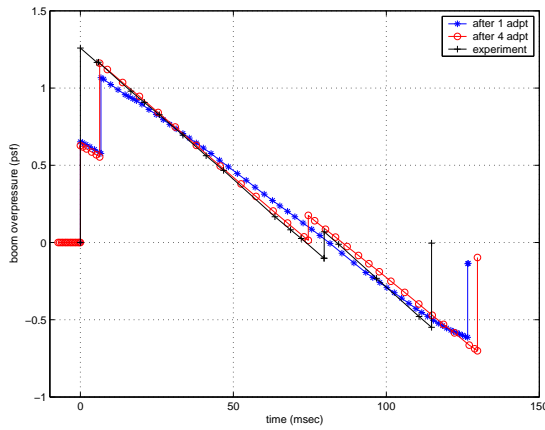


(a) Ground boom from $r=9.5$ in.

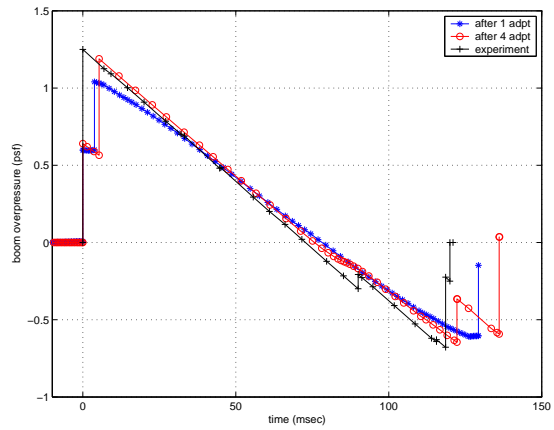


(b) Ground boom from $r=18$ in.

Figure 3.19: Ground boom comparisons. Configuration without nacelles.



(a) Ground boom from $r=9.5$ in.



(b) Ground boom from $r=18$ in.

Figure 3.20: Ground boom comparisons. Configuration without nacelles and tail.

Chapter 4

Variable-Fidelity Aerodynamic Analysis Tools

Single-minded efforts to reduce the boom loudness typically result in aerodynamic performance shortcomings that translate into reduced range or payload, longer balanced field length, and stability & control problems that need to be resolved to make these aircraft viable. Therefore successful and realistic design methods must carefully consider the balance between all of the performance measures, constraints, and requirements of the problem, while providing results that are sufficiently accurate to be believable. In addition, they must allow the designer the necessary freedom to explore the design space using reasonably large numbers of design variables. These basic requirements embody the fundamental dilemma of high-fidelity, multi-disciplinary design: how can one produce results that are highly accurate in a reasonable time with limited resources? [104, 105, 106, 107] This is one of the fundamental ingredients of the approach that we have followed here: a combination of low-fidelity tools that are enhanced by multi-fidelity analyses *only* in the areas where the increase in accuracy is needed, thus limiting the use of the expensive, high-fidelity tools to a minimum.

In this thesis, we attempt to combine a number of different fidelity analysis tools that include:

1. The Program for Aircraft Synthesis Studies (PASS): a multi-disciplinary design tool that incorporates carefully tuned fast models for the various disciplines

Analysis Tool	Level of Fidelity	Computation Time	Grid Topology	Boom Prediction
PASS	low	< 1 sec	structural panel	no
A502/Panair	mid/high	~7 sec	surface panel	yes
AirplanePlus	high	~10 min	unstructured tetrahedra	yes
SYN107-MB	high	~7 min	multi-block structured	yes

Table 4.1: Comparison of different fidelity analysis tools

in the design and is able to deal with all the major objective functions and constraints in typical aircraft synthesis problems. It includes low-fidelity aerodynamic analysis tool based on classical aerodynamics, and it does not have boom loudness prediction capability.

2. A linearized supersonic panel code (A502/Panair): higher-order linearized potential flow solution method using variable source and doublet strength over the curved panels with higher-order quadratic splines. Due to the limitations in the nonlinear transonic flow regime, it is used where it can predict similar results to the Euler analysis.
3. Automated tools based on a common geometry database to drive the analysis tools (BOOM-UA): This CAD-to-solution procedure is based on the CAPRI CAD-interface, the Centaur mesh generation system, and unstructured adaptive Euler solver (AirplanePlus), and the PCBoom3 software for propagation of the acoustic signatures.
4. Multi-block Euler/RANS solver (SYN107-MB): high-fidelity Euler/RANS solver using multi-block structured grid topology. It includes an adjoint solver so that gradient sensitivity information can be directly used with the NPSOL SQP optimization algorithm.

The hierarchy of our various-fidelity analysis tools is summarized in Table 4.1.

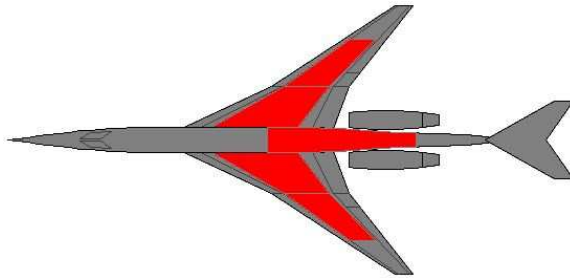
The approximate computation time is strongly dependent on the size of the computational grid and the computing platform. The values in Table 4.1 were obtained for the finest grid used with each tool. The analyses for PASS and A502/Panair

were performed on a modern workstation (Pentium 4, 3.2 GHz), and AirplanePlus and SYN107-MB were run in parallel using 16 Athlon AMD2100+ processors of a Linux Beowulf cluster. The number of nodes in the structured/unstructured grids was about 4-5 million, and the number of surface panels for the A502 calculation was about 2,000. The computation time for mesh generation for either the structured or unstructured grid and adaption is not included in these estimates.

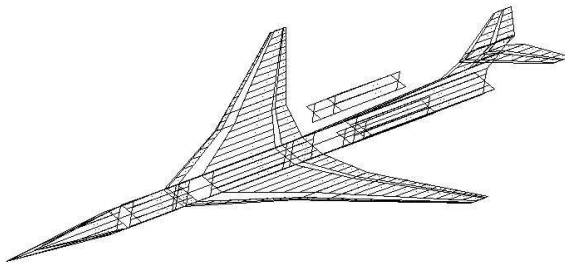
In the following sections we describe the various components of the multi-fidelity analysis tools. We start with the description of the PASS tool for conceptual multi-disciplinary design, its capabilities and the optimization algorithm used. We then provide details of the automated analyses for both the linearized supersonic panel code (A502/Panair) and the Euler/Navier-Stokes solver AirplanePlus, including all of the pre- and post-processing modules required to produce the necessary information.

To highlight the similarities and disparities between low- and high-fidelity tools, Panair/A502 and AirplanePlus results are compared in two aspects: drag polars for aerodynamic analysis, and near-field pressure and ground overpressure levels for boom analysis. Although AirplanePlus and SYN107-MB are based on the same nonlinear Euler flow solution technique, they use completely different grid topologies: unstructured and structured grids respectively. A comparison of the results from two different high-fidelity tools is also compared.

4.1 PASS



(a) Fuel tank layout.



(b) Vortex-lattice model.

Figure 4.1: Different views of the configuration within PASS.

In addition, the same interface can be used to define the design optimization problem. Design variables, objective functions and constraints can be setup using any of the relevant parameters and functions that are used in each of the disciplinary modules. A view of two of the various aircraft models (fuel tank arrangement and vortex lattice mesh) that are used by PASS can be seen in Figure 4.1. Incorporating PASS into the analysis allowed for the evaluation of all aspects of mission performance, thus providing a balanced configuration not just limited to meeting some singular performance goal, but also capable of achieving field length, climb gradient, and cabin

PASS (Program for Aircraft Synthesis Studies) [85, 86], an aircraft preliminary design tool created by Desktop Aeronautics, Inc., was used to generate all of the designs presented in this work. It has been successfully applied [85, 86] to several commercial and military supersonic aircraft studies for industry. PASS also has been the basis of a aircraft design course [83] for the graduate students at Stanford University.

PASS uses a simplex method and an integrated set of predictive modules for all of the relevant disciplines in the design (including mission performance) to generate optimized designs that satisfy a number of imposed constraints.

PASS uses a graphical user interface to explore the results of each of the participating disciplines in a design. In ad-

constraints (for example) required for a realistic aircraft design. Some of the most relevant capabilities of PASS for this work are briefly summarized below. Other various capabilities such as maximum elevator rotation, CG management, structural weight modeling, rotation constraints are explained in detail in [86].

4.1.1 Geometry

The fuselage geometry is determined by a cross-section layout which is a function of seat and aisle width, the seating arrangement, and the floor height. Because of the pressurization and flow separation problems, a circular cross-section is considered. The cabin length calculation to determine the fuselage length is based on the number of passengers and seat layouts. Additional considerations related to the wave drag computation are included in the layout of the fuselage. The wing geometry is extracted from the following design parameters: wing reference area, span, quarter-chord sweep, taper, and leading and trailing edge extensions.

4.1.2 Drag Estimation

Lift- and volume-dependent wave drag, induced drag and viscous drag are evaluated at key mission points. Inviscid drag is estimated using linearized methods. The viscous drag computation is sensitive to Reynolds number and Mach number, and is based on an experimentally derived fit. Special attention is paid to the transonic drag rise, with numerous points being sampled up to and through Mach 1. The analysis detail is of a level that allows configuration tailoring to minimize drag during supersonic cruise (i.e. the use of the area rule is contemplated.)

4.1.3 Weights and CG

Component weights are based on available data for modern business-jet class aircraft. Wing weight is estimated based on a bending index that is related to the fully stressed bending weight of the wing box, coupled with a statistical correlation. The weights of tail surfaces are similarly determined. Fuselage weight is based on both the gross

fuselage wetted area and the use of a pressure-bending load parameter.

The CG location is computed based on typical placements and weights of the various aircraft components; CG movement during the mission due to fuel burn is also computed based on the fuel tank layout and the ability to transfer fuel between tanks is also used to aid in the trimming of the configuration throughout its mission.

4.1.4 Static Stability and Trim

The change in pitching moment about the CG must be negative as the lift is increased. The lift curve slope for the isolated tail (lift curve slopes for wing and horizontal tail are determined using a DATCOM correlation) is adjusted to account for wing and fuselage effects of download on the tail. Trim is achieved by setting the incidence of the tail surface to obtain a zero pitching moment.

4.1.5 Propulsion

Engines are modeled by sampling a manufacturer's deck at numerous Mach numbers and altitudes and constructing a fit. For this study, a generic deck was created and hand-tuned to give performance of a level achievable by currently available, mature technology, low-bypass turbofan engines.

4.1.6 Low-Speed Analysis

Low-speed stability and trim are computed using a discrete-vortex-lattice method. This data is then used to predict such things as the balanced field length (BFL) for the aircraft, stability derivatives and estimates for tail incidences at critical low-speed points (take-off rotation, for example.)

4.1.7 High-Lift Systems

Increasing the maximum lift coefficient of the wing is very important in order to achieve good take-off and landing characteristics by reducing the stalling speed. Estimating the maximum lift coefficient ($C_{L_{max}}$) is not trivial and actually involves

simultaneous work of sizing the aircraft and accurately computing the aircraft field performance. In the method used here, firstly the maximum lift coefficient of the airfoil and clean wing are estimated at the outer-panel and the corrected for the detailed geometry of the wing, including taper ratio and sweep effects using correlations.

The slat (if present) increases the section lift coefficient, suppressing the leading-edge pressure peak by modifying the nose camber. The specific increase of $C_{L_{max}}$ corresponding to deflection angle, θ_{slat} is estimated based on data from the Douglas Aircraft Company [84]. Trailing edge flaps allow more lift by increasing the effective camber of the airfoil.

4.1.8 Loads

V-n diagrams are used to determine the maximum aircraft loads as a function of airspeed, altitude, and weight. Two diagrams are created: the maneuver diagram for variations in the load factor with airspeed for maneuvers and the gust diagram associated with vertical gusts.

4.1.9 Operating Cost

Total operating cost (TOC) contains the direct operating cost (DOC), associated with the direct operation of the aircraft, and the indirect operating cost (IOC), including items that support the operations of the aircraft indirectly. The details items accounting for the DOC and IOC are explained in [84].

Although PASS has some cost modeling capabilities none of these features of PASS have been used in this work.

4.1.10 Mission Analysis

The mission analysis routine ties together all the various tools in PASS to run an aircraft through a typical flight and evaluate its overall performance. The key points analyzed are the takeoff run, takeoff rotation, 2nd segment climb, subsonic climb to acceleration altitude, subsonic-to-supersonic acceleration, supersonic climb to initial

cruise altitude, cruise and landing. In our work in this thesis, only the cruise condition benefits from enhanced computations for the aircraft performance.

4.1.11 Optimization

PASS provides a non-gradient based optimizer for configuration studies based on the Nelder-Mead simplex method. Given some variables, the optimizer will minimize an objective function subject to constraints. The variables, constraints and objective are all user-defined. Typically, the optimizer will be tied to the mission analysis computation. Constraints usually consist of performance goals such as range and balanced field length. Additional constraints to ensure a viable aircraft in the eyes of the FAA may also be imposed, to ensure, for instance, that the aircraft will climb out at the minimum 2.4% gradient stipulated by FAR regulations. Details of the optimization problem formulation are discussed in later sections.

4.1.12 Design Configurations

The baseline design, from which all work started, was created using the default PASS analysis modules which are based on classical supersonic aerodynamics and vortex-lattice methods. Subsequent designs are also created by PASS with two significant differences: 1) the simplified aerodynamic drag prediction module was replaced by the response surface fits created using our multi-fidelity approach, and 2) a ground boom calculation module was added (also based on a multi-fidelity response surface fit) for addition of loudness-related objective functions or constraints.

It is worth noting that in the designs presented in this thesis, no assumptions of future technology have been made. All designs use models of existing propulsion plants, materials, and systems that can be incorporated into an actual design today.

4.2 Linear Panel Method: A502/Panair

The A502 solver, also known as Panair [99, 138], is a flow solver developed at Boeing to compute the aerodynamic properties of arbitrary aircraft configurations flying at

either subsonic or supersonic speeds. This code uses a higher-order (quadratic doublet, linear source) panel method, based on the solution of the linearized potential flow boundary-value problem. Results are generally valid for cases that satisfy the assumptions of linearized potential flow theory - small disturbance, not transonic, irrotational flow and negligible viscous effects. Once the solution is found for the aerodynamic properties on the surface of the aircraft, A502 can then easily calculate the flow properties at any location in the flow field, hence obtaining the near field pressure signature needed for sonic boom prediction. In keeping with the axisymmetric assumption of sonic boom theory, the near field pressure can be obtained at arbitrary distances below the aircraft [100].

4.3 Comparison of A502 and AirplanePlus Results

Since we are using different-fidelity flow solver modules for our multi-fidelity response surface fitting tool, it is important to be aware of the similarities and differences in the solutions provided by each of the solvers. In certain regions of the design space (where the flow is linear), the low-fidelity analysis(A502/Panair) can provide as accurate solutions as the high-fidelity analysis(AirplanePlus) and improve computational efficiency. However, the low-fidelity analysis cannot be applied to the entire design space because its accuracy is limited in the transonic nonlinear regime. Therefore for the areas of the design space where the low-fidelity tool fails in accuracy and convergence, high-fidelity analysis should be applied. By knowing exactly the limits of applicability of the low-fidelity analysis, we can minimize the necessary number of high-fidelity analyses and still obtain the same accuracy that would have resulted from using high-fidelity methods alone. The purpose of this section is to compare the results provided by A502/Panair and BOOM-UA, and highlight the areas where A502/Panair can be a viable alternative to the Euler calculation and where A502/Panair is not sufficiently accurate.

Two separate configurations were considered and employed only for comparison purposes. The details of the geometry and flight condition are summarized in Table 4.2. The first one was used to assess the quality of the aerodynamic performance

data. This is the configuration design which was optimized by the standard version of PASS and, according to PASS, satisfies all mission requirements in Tables 4.3 and 6.5. The details of the PASS optimization procedure are explained in detail in Section 6.1. For this PASS optimized configuration, the design parameters for the wing sections (highlighted in blue in Table 4.2) are assumed to be optimum but are not known, and thus we set them as some possible values based on previous optimization experience. To investigate the effect of the tail and nacelles on the aerodynamic performance, these parts are removed and eventually the wing-body-only configuration is considered as well. The second configuration was used to compare the boom predictions, and geometric details are shown in Table 4.4. This is the configuration which had been optimized in previous work [92, 89, 101] although realistic mission constraints are not considered.

4.3.1 Comparison of aerodynamic performance

Wing-Body Configuration: Standard-PASS optimized configuration

Aerodynamic performance for the PASS-optimized configuration was analyzed with A502 and AirplanePlus. The configuration used in these calculations is the same configuration in the next section, but the nacelles and tail are removed. The panel generation for the A502 calculation and the triangular surface mesh for the Euler calculations are shown in Figure 4.2. The Euler grid is significantly coarsened for visualization purposes compared to the one used in the actual computations. The freestream Mach, $Mach_\infty$, is 1.6 and steady cruise conditions are assumed. The coefficient of drag, C_D , was calculated at various C_L values using both A502 and AirplanePlus, and was plotted in the drag polar in Figure 4.3. Good agreement between A502 and AirplanePlus can be seen resulting mainly from the lack of transonic effects caused by the low Mach number normal to the leading edge of the wing inboard section, $Mach_\perp = 0.7$.

Fuselage, Wing and Tail Geometry

Maximum fuselage length	125 <i>ft</i>
Wing reference area (S_{ref})	1,078 ft^2
Wing aspect ratio (AR)	4.0
Wing quarter-chord sweep (Λ)	53.35°
Wing taper	0.15
Wing dihedral	3°
Leading edge extension	0.278
Trailing edge extension	0.197
Break location	0.4
Location of wing root LE	0.294
Root section t/c	2.5%
Break section t/c	3.0%
Tip section t/c	2.5%
Root section twist	0.0
Break section twist	0.0
Tip section twist	0.0
Root section maximum camber location	0.279
Break section maximum camber location	0.345
Root section maximum camber	0.0
Break section maximum camber	0.0
Vertical tail area (% S_{ref})	0.125
Vertical tail AR	0.65
Vertical tail Λ	56°
Vertical tail λ	0.6
Horizontal tail area (% S_{ref})	0.6
Horizontal tail AR	2.0
Horizontal tail Λ	56°
Horizontal tail λ	0.3

Flight condition

Freestream Mach number	1.6
Altitude at initial cruise	42,002 ft
Design C_L at initial cruise	0.13
Alpha limit	15°
Maximum Take-Off Gross Weight	96,875 lb

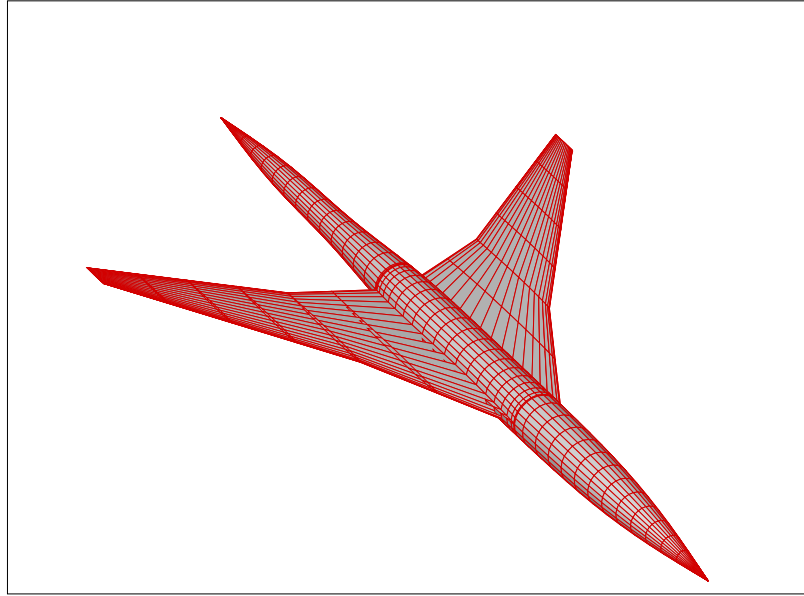
Table 4.2: Summary of geometric and performance design variables for PASS-optimized configuration

Range	4,500 nmi
BFL	6,000 ft
Minimum static margin	0.0

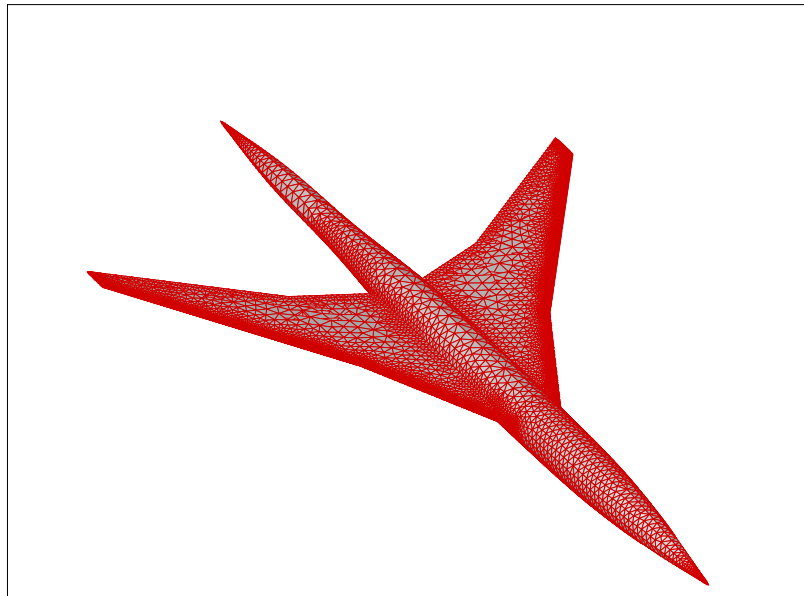
Table 4.3: Some mission constraints for PASS-optimization

Fuselage, Wing and Tail Geometry	
Maximum fuselage length	150 <i>ft</i>
Wing reference area (S_{ref})	2,064 ft^2
Wing aspect ratio (AR)	6.0
Wing quarter-chord sweep (Λ)	35.0°
Wing taper	0.3
Wing dihedral	1°
Leading edge extension	1.0
Trailing edge extension	0.5
Break location	0.5
Location of wing root LE	0.3
Root section t/c	4.0 %
Break section t/c	4.0 %
Tip section t/c	4.0 %
Root section twist	0.0
Break section twist	0.0
Tip section twist	0.0
Vertical tail area (% S_{ref})	0.291
Vertical tail AR	2.56
Vertical tail Λ	41°
Vertical tail λ	0.5
Horizontal tail area (% S_{ref})	0.008
Horizontal tail AR	2.7
Horizontal tail Λ	41°
Horizontal tail λ	0.5
Flight condition	
Freestream Mach number	1.5
Altitude at cruise	50,000 ft
Design C_L at cruise	0.1
Weight at cruise	100,000 lb

Table 4.4: Summary of geometries and flight condition for boom baseline



(a) Surface panel representation for A502



(b) Triangular surface mesh for AirplanePlus (coarsened)

Figure 4.2: Surface grids for wing-body standard-PASS optimized configuration

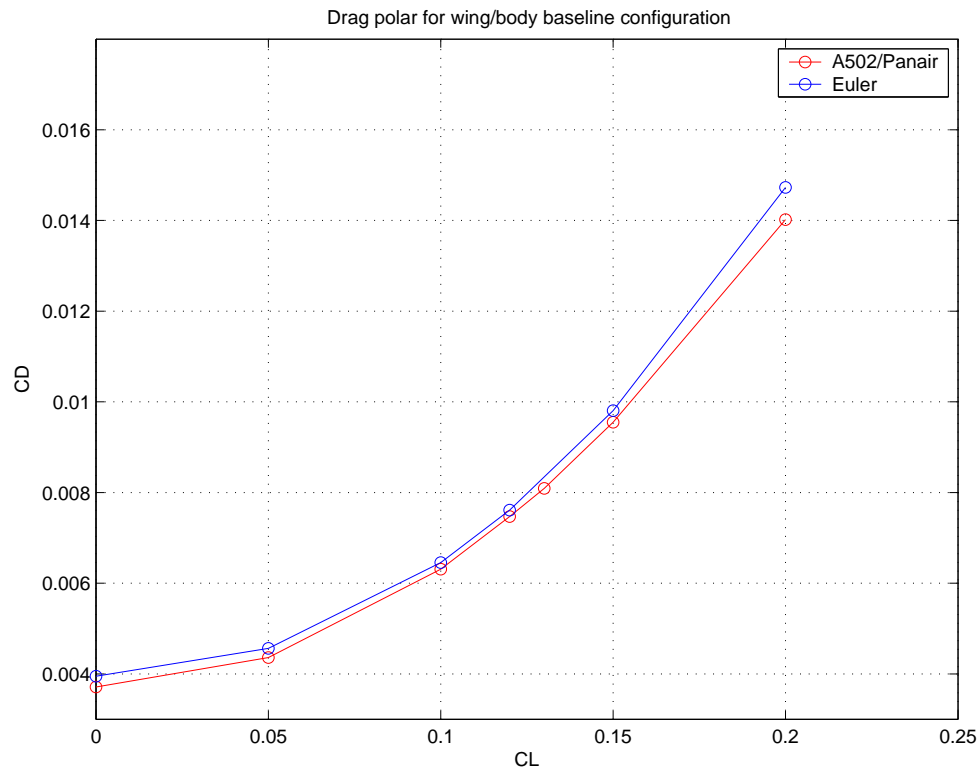
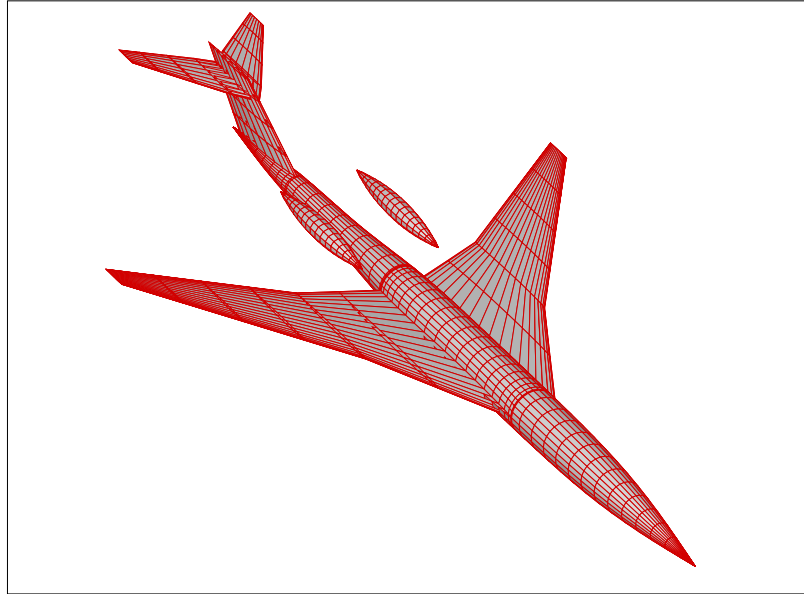


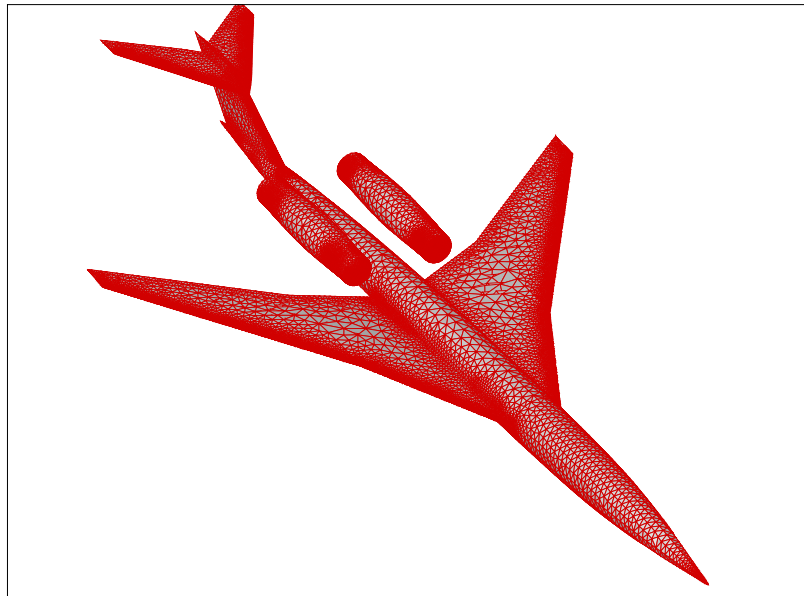
Figure 4.3: Comparison of drag polars for standard-PASS optimized wing-body configuration between A502 and AirplanePlus

Full Configuration: Standard-PASS optimized configuration

A complete configuration with vertical tail, horizontal tail, and nacelles was considered for aerodynamic performance comparisons. A surface panel representation and a coarsened triangular surface mesh are shown in Figure 4.4. Since the inflow/outflow boundary conditions for the nacelles cannot be handled in A502, they are replaced by solid bodies of revolution with identical volume to the original nacelles. Thus no internal flow is considered for the nacelles in the A502 calculations. The drag polar in Figure 4.5 shows slight differences between the A502 and Euler analyses. The difference between the A502 and Euler calculations appears to be a constant shift of magnitude 6-7% range. One of the reasons for these differences may be the difference in the nacelle representation.



(a) Surface panel representation for A502



(b) Triangular surface mesh for AirplanePlus (Coarsened)

Figure 4.4: Surface grids for the standard-PASS optimized configuration

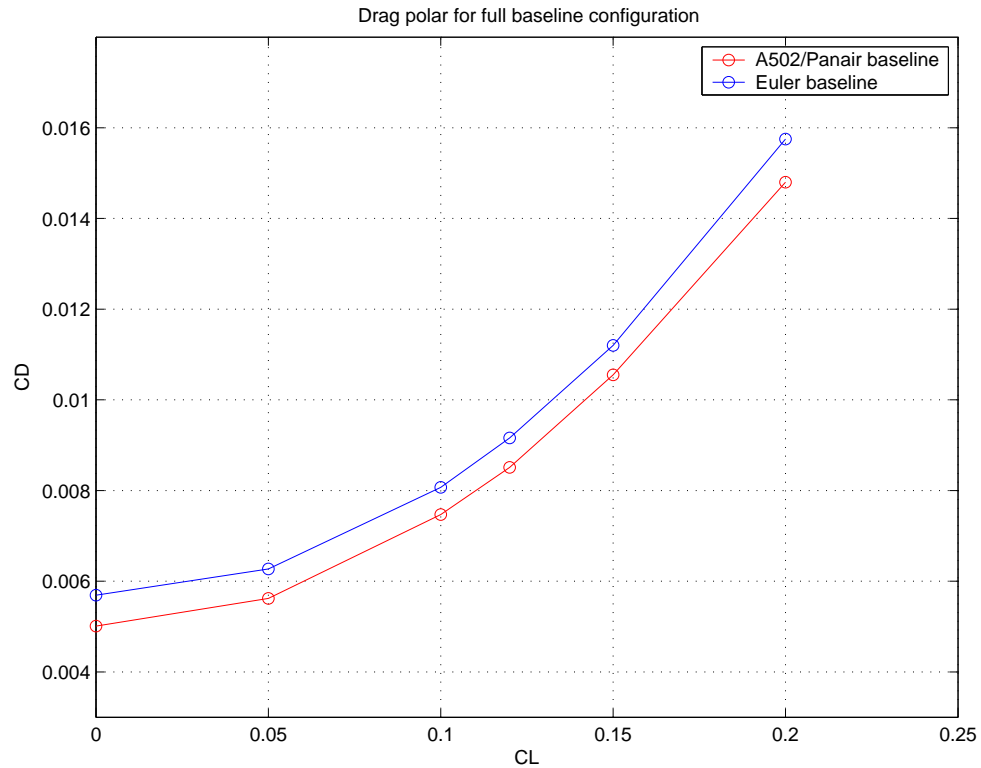
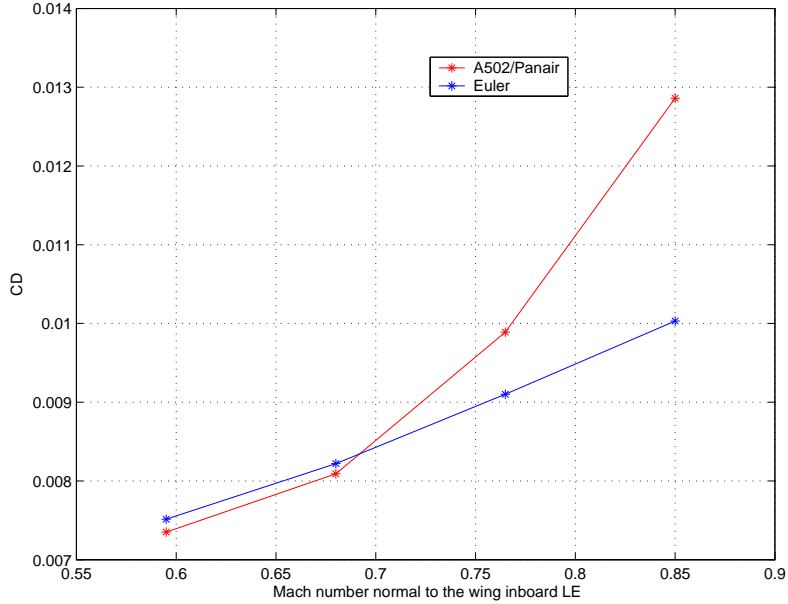


Figure 4.5: Comparison of drag polars for full configuration between A502 and AirplanePlus

To show that A502 is unable to predict transonic effects, the values of the C_D computed by both A502 and AirplanePlus have been compared by varying the freestream Mach number such that $Mach_{\perp}$ as defined earlier is in the transonic regime. For a given geometry, the sweep angle of the inboard wing is 64.855° and is larger than the sweep angle of outboard wing section, 53.349° . The results of this comparison are shown in Figure 4.6, and the numerical values and errors are summarized in Table 4.5. As $Mach_{\perp}$ gets close into the transonic regime the difference in C_D between A502 and the Euler calculation becomes as large as 28%. For those regions, A502 cannot produce accurate results and Euler calculations should be used instead.


 Figure 4.6: Comparison of values of C_D for varying $Mach_{\perp}$ for full configuration

$Mach_{\infty}$	$Mach_n$	$C_{D_{A502}}$	$C_{D_{Euler}}$	Error (%)
1.4	0.5949	0.00735	0.007514	-2.1826
1.6	0.6799	0.00809	0.00822	-1.58
1.8	0.765	0.00989	0.00911	8.6694
2.0	0.85	0.01286	0.01003	28.215

 Table 4.5: Comparison of values of C_D for varying $Mach_{\perp}$ for full configuration

4.3.2 Comparison of results for ground boom loudness

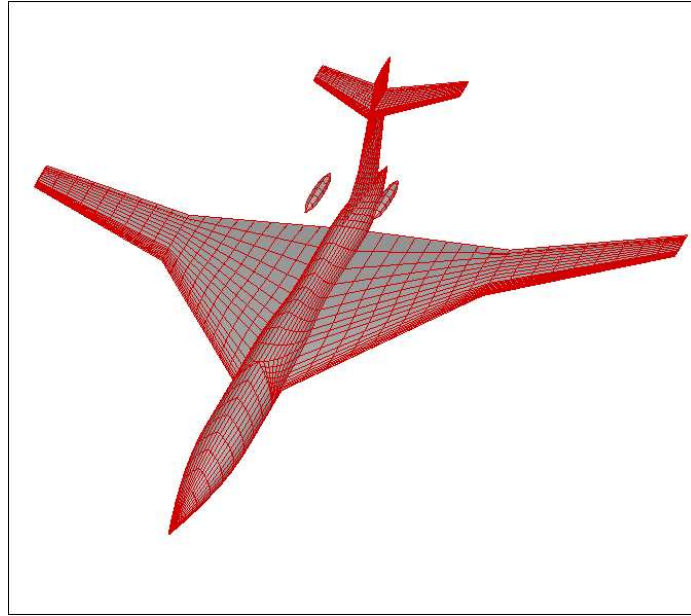
Figure 4.7 shows another aircraft configuration used for comparisons of the ground boom loudness predicted by A502/Panair and the Euler calculations. This configuration was the baseline for a previous multi-disciplinary optimization [92, 89, 101]. As pointed out earlier, this baseline configuration was built without consideration for realistic mission constraints. Although some very simplified constraints such as cruise range, trim and longitudinal stability were incorporated [89], a detailed mission profile was never accounted for.

The surface panel representation for A502 and the triangular surface mesh for the Euler calculations are shown in Figure 4.7. A typical solution-adaptive refinement

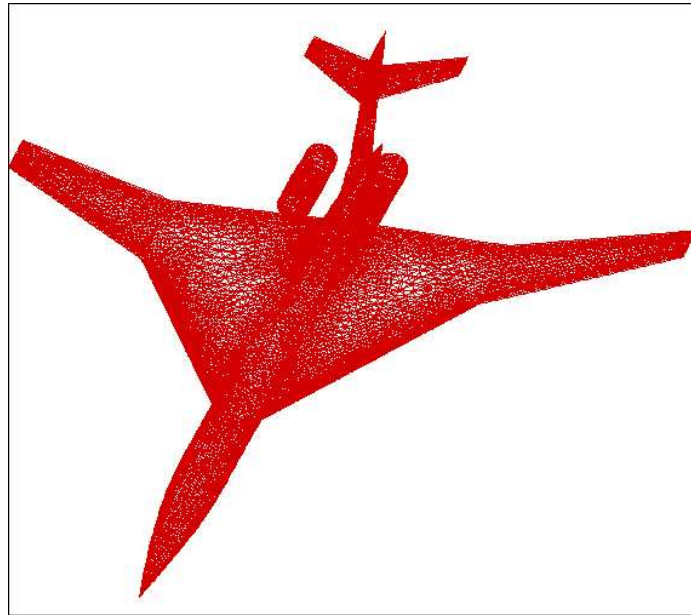
procedure to extract the near-field pressure distribution is shown in Figure 4.8 where the mesh has been refined through two adaption cycles. The flight Mach number was set to 1.5, the flight altitude was 50,000 *ft*, and a steady cruise condition was assumed. At this freestream Mach number and for the given quarter-chord sweep angle (35°), the $Mach_\perp$ was about 0.7 and only small transonic effects are observed. A pressure gradient based criterion explained in Chapter 3 was applied and refinement can be seen in the region where shocks and expansions are present.

The analysis was carried out for two cases: (1) angle of attack fixed at 3° and (2) design C_L fixed at 0.1. For both cases the near-field pressure was extracted at 1.2 body lengths on the symmetry plane below the aircraft and the ground boom was predicted by both the Thomas code and PCBoom3. For both cases excellent agreement is shown in Figures 4.9 and 4.10: no transonic effects were experienced.

When the freestream Mach number is increased so that $Mach_\perp$ gets close to 1.0, the differences in the near-field pressure distributions obtained by A502 and AirplanePlus become much more pronounced. In the following results, the freestream Mach number was given the values 1.76, 1.863, 1.9665, and 2.07 corresponding to $Mach_\perp$ values of 0.8533, 0.9032, 0.9534 and 1.0. All computations were carried out at a fixed $C_L = 0.10$. Figure 4.11 shows the computed near-field pressure signatures from both A502/Panair and the Euler computations for these four cases. It can be seen that, as the normal Mach number enters the region where transonic flow effects are significant, the predictions of A502/Panair start to deteriorate to the point where they become unusable. However, one must note that even for normal Mach numbers of 0.90, the predictions in near-field pressure distribution from A502 are quite accurate, while the C_D prediction is already off by 28% for $Mach_\perp$ of 0.85 (see Table 4.5.) Agreement is fairly good at the first two flow conditions (with a maximum relative error of only 5.5%) but it quickly worsens (the relative error is 20% in the last case). This experiment, together with additional experience not reported here shows that it is only in this very narrow region of the design space that A502/Panair does not deliver useful results. This is important information to ensure that our multi-fidelity approach can create high-fidelity information at fairly low cost. Initially one may think that if the transonic flow regime is avoided altogether, then A502/Panair should



(a) Surface panel representation for A502



(b) Triangular surface mesh for AirplanePlus

Figure 4.7: Surface grids for the boom baseline configuration

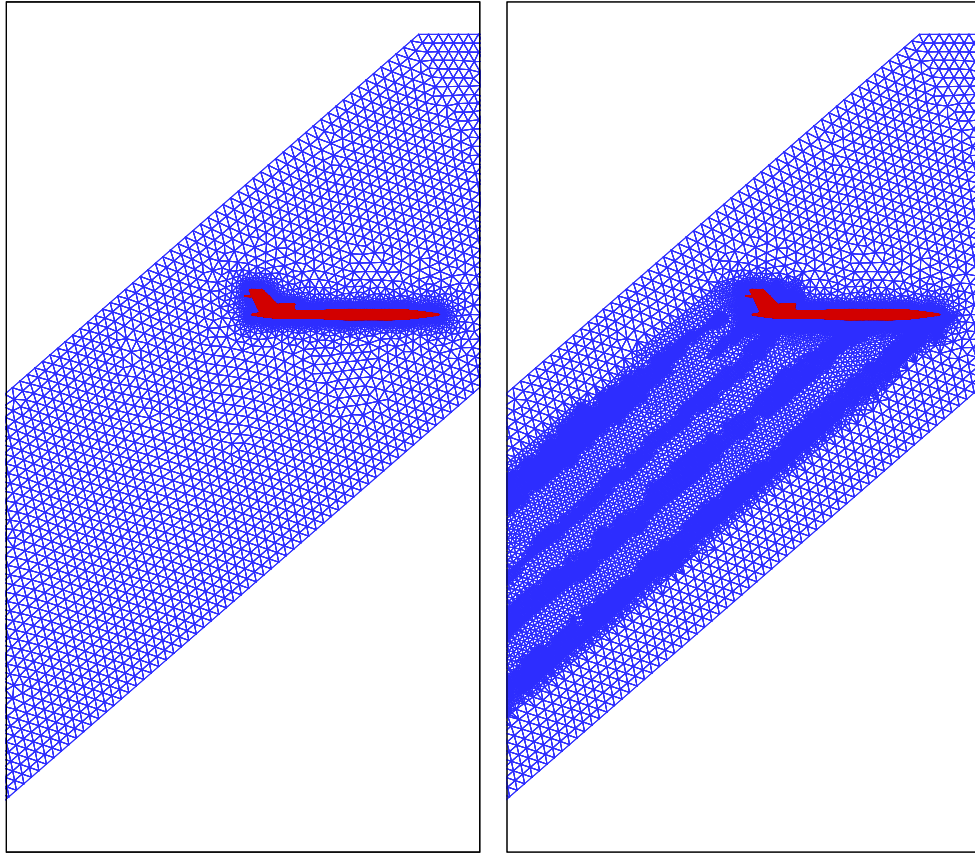
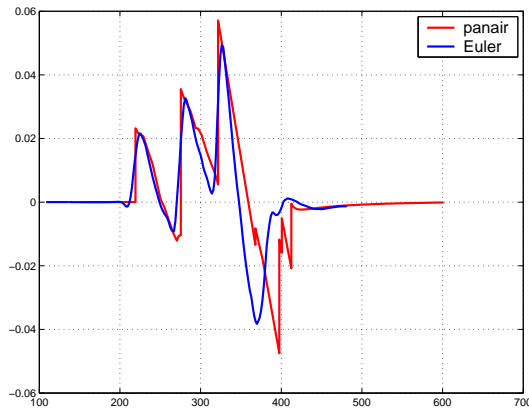


Figure 4.8: Symmetry plane mesh before and after solution-adaptive refinement

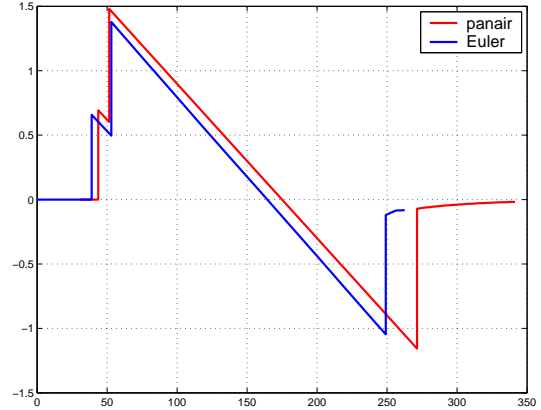
be sufficient to accomplish all design tasks related to aerodynamic performance and ground boom loudness. Unfortunately, the results in Chapter 6 point out that the optimizer appears to want to arrive at wing geometries that operate in this regime and, therefore, the higher fidelity models are necessary to obtain believable designs.

4.4 SYN87-SB and SYN107-MB

Finally we present results from another set of high-fidelity analysis tools: SYN87-SB and SYN107-MB. Both solvers are based on the solution of the Euler/RANS equations on structured (possibly multiblock) grids. Both solvers include an adjoint solver that can be used to generate inexpensive gradient information that can later be used in

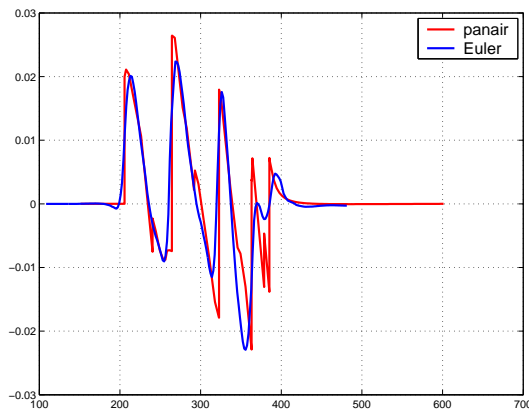


(a) Comparison of near-field pressure

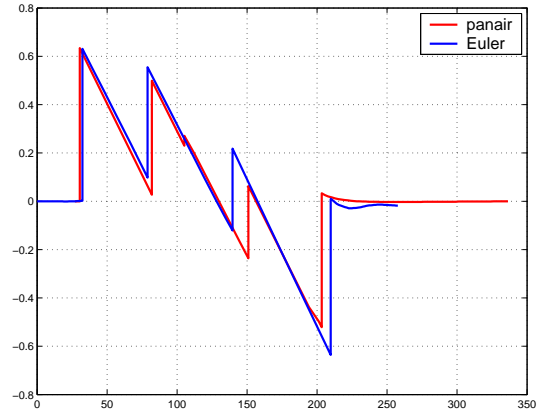


(b) Comparison of ground boom signature

Figure 4.9: Comparison of near-field pressure and ground boom signature between A502 and AirplanePlus when $AOA = 3^\circ$

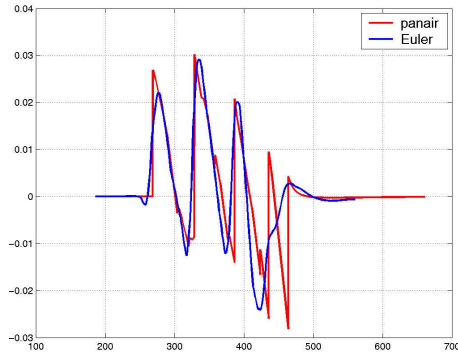


(a) Comparison of near-field pressure

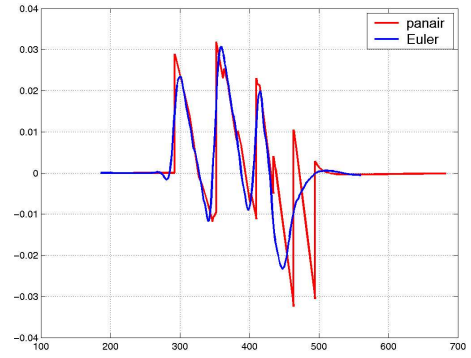


(b) Comparison of ground boom signature

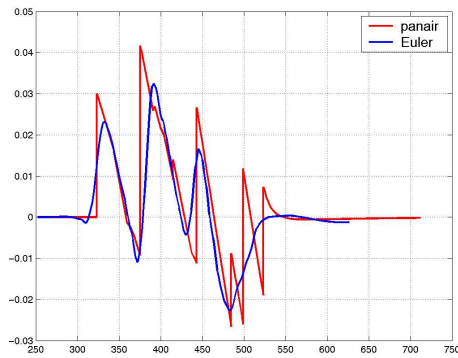
Figure 4.10: Comparison of near-field pressure and ground boom signature between A502 and AirplanePlus when $C_L=0.1$



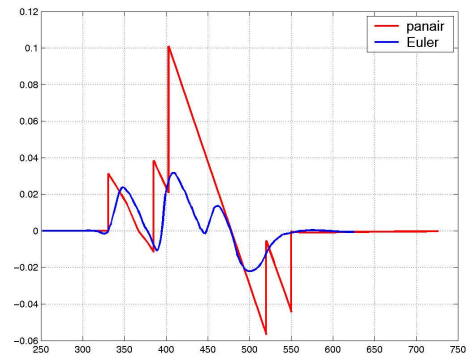
(a) $Mach_\infty = 1.76, Mach_\perp = 0.8533$



(b) $Mach_\infty = 1.86, Mach_\perp = 0.9032$



(c) $Mach_\infty = 1.97, Mach_\perp = 0.9534$



(d) $Mach_\infty = 2.07, Mach_\perp = 1.0036$

Figure 4.11: Near-field pressure comparisons between A502/Panair and the Euler computations for increasing free stream Mach numbers and corresponding normal Mach numbers.

shape optimization studies.

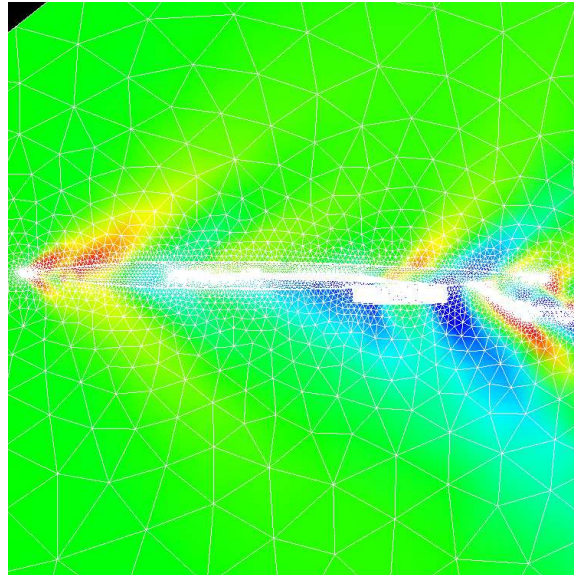
1. *SYN87-SB*. A single-block, wing-body Euler adjoint analysis and optimization code that uses the NPSOL SQP algorithm for optimization with or without constraints. SYN87-SB allows for arbitrary changes to the shape of the fuselage and wing and is able to enforce thickness, curvature, and fuel volume constraints.
2. *SYN107-MB*. A multi-block, complete configuration, RANS adjoint optimization code that also uses the NPSOL SQP algorithm for optimization and that allows similar geometry controls, cost functions, and constraints as SYN87-SB, but that can be made to treat arbitrarily complex geometries such as the complete aircraft configurations that are the subject of this work.

4.4.1 Validation with Unstructured Code

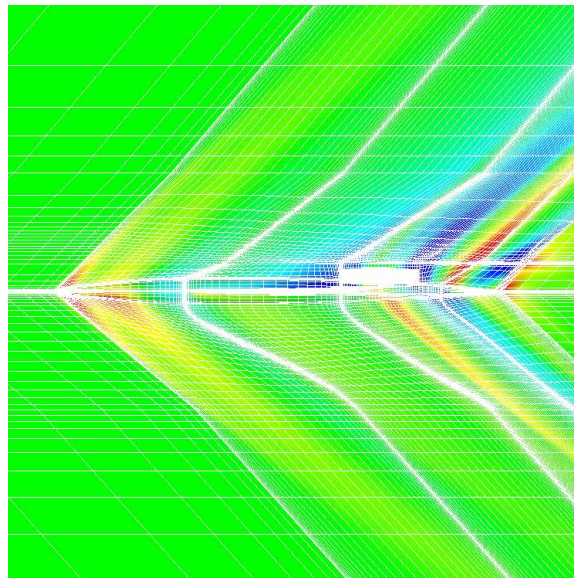
In later studies, we employ a gradient-based optimization approach for local searches of the design space. For these studies an adjoint solver was used to obtain gradient sensitivity information at rather low cost. Unfortunately the adjoint solver was only available for structured grid topologies and therefore we needed to use SYN107-MB rather than AirplanePlus. Because additional solvers are introduced, it is important to validate their predictions to guarantee the accuracy of the outcome. Although different grid topologies (see Figure 4.12) are used in SYN107-MB and AirplanePlus, both solvers are of high-fidelity (and they both are used in Euler mode) and therefore their results are expected to be very close. Figure 4.13 shows a comparison of a drag polar computed using AirplanePlus and SYN107-MB. The results shows that the two curves nearly coincide.

In our design studies, the local search method was not used by itself but instead was performed after a global search had been completed. Large variations in the geometric design parameters are allowed in the global search since global search methods can better handle resulting large and ill-behaved design spaces with some regularities (they do not require gradient information.) The local search step following the global search explores a small region of the design space identified by the global search which

can be locally smooth and continuous and therefore makes gradient-based optimization possible. Variations in geometry corresponding to a narrowed design space are not necessarily large and a structured grid can be easily perturbed to obtain the gradient information. A structured mesh flow solver can then be used. The details of global and local searches will be explained in Chapter 6.



(a) Tetrahedral unstructured grid, mesh nodes = 1.6 million



(b) Multi-block structured grid, mesh nodes = 5.9 million

Figure 4.12: Comparison of grid between unstructural and structural system

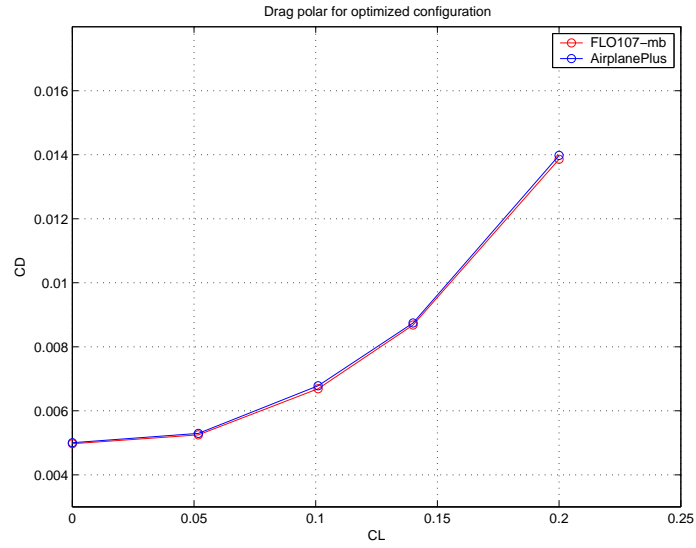


Figure 4.13: Comparison of drag polars between SYN107-MB and AirplanePlus

Chapter 5

Response Surface Approximation and Optimization Technique

The choice of optimization method, either global or local, depends to a large extent on the characteristics of the design space. For smooth design spaces where the derivatives with respect to all design variables are available, gradient-based optimization approaches can locate a local minimum with a relatively small number of function evaluations. However, for noisy design spaces the usefulness of gradient information is questionable. In these cases global optimization techniques are more appropriate at the expense of much larger numbers of function evaluations. When the function evaluation requires significant amounts of computational resources, such as in our MDO problem where the aerodynamic and ground boom objectives are analyzed by high-fidelity methods, the whole design process becomes complicated and time-consuming. Previous research [104, 105, 106, 107] has shown the complexity of the MDO design process even when fully parallelized modules and advanced sensitivity techniques are used. For this reason, high-fidelity analyses typically used in single discipline designs may not be suitable for direct use in MDO [108, 105]. Faced with these problems, the alternative of using simpler approximation models has received increasing attention in recent years.

In this chapter we first demonstrate the characteristics of the design spaces we are faced with. The design spaces we need to explore typically have large dimensionality

(~ 30), and it becomes difficult to visualize their characteristics. In the first section two-dimensional slices of the design space are illustrated to visually understand the characteristics of the design spaces we handle in this study. The effect of the number of samples on the accuracy of the response surfaces generated are investigated.

Three types of response surface approximation methods are employed in this thesis: the Kriging model, Neural Networks (NN) and multi-dimensional quadratic fits. Each response surface has different accuracy and efficiency (construction time) properties, and they have different capabilities to handle large numbers of samples. The accuracy and efficiency of the neural networks and quadratic fit approaches are compared, since both are based on least-squares fitting techniques.

Due to the different number of analyses carried out with each of the different fidelity tools, a single response surface approach is not sufficient and we combine methods and tools to construct multi-fidelity response surfaces. Thus, we construct multi-fidelity response surfaces where the number of analyses with each fidelity tool decreases with increasing fidelity. Low-fidelity tools have very inexpensive computational cost and can be used for a large number of samples within limits of their applicability whereas high-fidelity tools are rather expensive and should be applied only in the small regions where the accuracy of low-fidelity tools is not sufficient.

5.1 Characteristics of Design Space

The sonic boom design space is known to be noisy, discontinuous and to contain multiple local extrema [52]. Shape optimization of complete three-dimensional supersonic jets requires a reasonably large number of design variables and the visualization of the design space characteristics is not straightforward.

For a simple inspection of the characteristics of the design space, two design variables that control the fuselage radius close to the fuselage nose are selected. These design variables are expected to play a dominant role in the formation and intensity of the front shock of the ground N wave. The two fuselage radii at 7.5% and 11.25% of the body length are varied by $\pm 50\%$ from the original values in small increments. The configuration of interest is the PASS-optimized configuration in Chapter 4. For

simplicity in the computations, the vertical and horizontal tails and the nacelles are removed from the configuration. Analyses were conducted using FLO107-MB, a parallel single/multi-block Euler/RANS flow solver using structural grid topology.

Figure 5.1 shows the corresponding two-dimensional distributions of C_D and the dBA noise metric without rise time modification. The C_D response is relatively smooth over the entire region, while that for the sonic boom noise metric is very noisy and shows multiple local minima and discontinuities. If we were to increase the dimensionality of the design space, the complexity of the responses would increase dramatically.

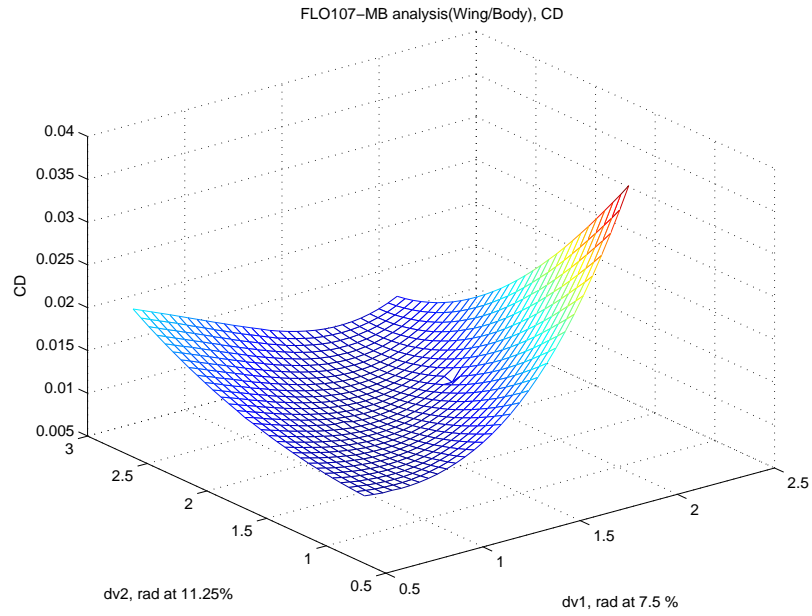
These results produce useful information in deciding what type of response surface method and optimization scheme should be employed for this kind of problems. A response surface method which can simulate multiple local extrema and discontinuities should be considered. Derivative information may not be available for regions containing discontinuities and gradient-based local minimization schemes may fail. Thus it is concluded that derivative-free global optimization schemes are better suited for this type of problem (such as non-linear SIMPLEX methods and Genetic Algorithms which are discussed in a later section.) The cost of these global optimization techniques (derived from the associated number of function evaluations) can be minimized through the use of response surface approximations that are inexpensive to evaluate.

5.2 Approximation Methods for Response Surface Construction

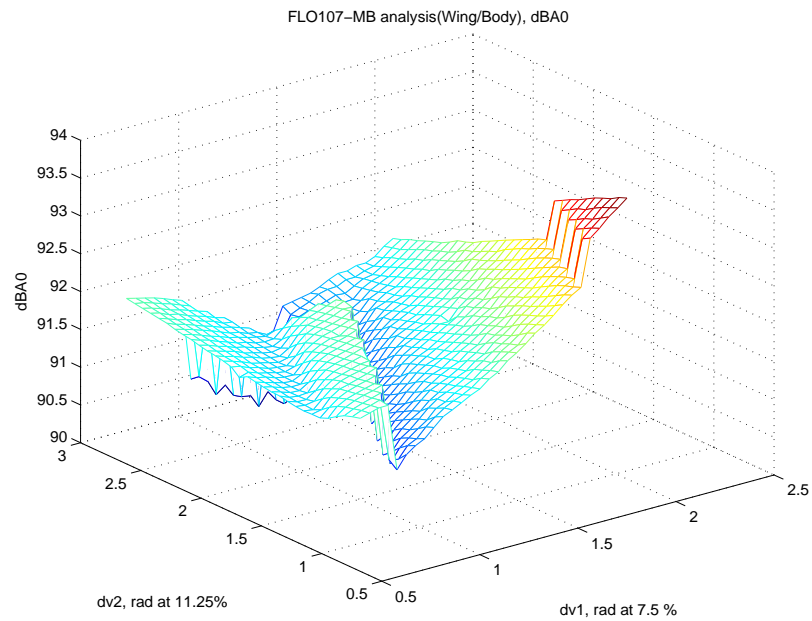
5.2.1 Sampling technique

The problem of choosing a set of initial design sites (sampling points) over the entire design space has been studied extensively in the recent literature on the design and analysis of computer experiments (DACE) [109, 116, 117].

In this study, we use one of the quasi-Monte Carlo integration methods: Latin Hypercube Sampling(LHS) [120, 122]. This is often called a “space-filling” method in the sense that it samples the space according to a certain distribution for the



(a) Design surface of C_D



(b) Design surface of dBA

Figure 5.1: Two dimensional design spaces analyzed by FLO107-MB

inputs such that an independent uniform distribution on $[0, 1]$ is achieved. If we want n sample points in a d dimensional space, then each of the n variables is chosen from d equally spaced values. After the design sites have been chosen, aerodynamic performance, sonic boom loudness, and mission violation are evaluated by our various-fidelity analysis tools and an initial response surface is constructed.

5.2.2 Least-squares regression response surface modeling

One of the easiest and fastest methods of fitting is the traditional quadratic response surface fitting. This method is based on least-squares regression techniques [123, 124, 125] and mathematically it reduces to approximating

$$y(x) = f(x) + \epsilon, \quad (5.1)$$

where $y(x)$ is the unknown function of interest, $f(x)$ is the polynomial approximation, and ϵ is the random error that is assumed to be normally distributed with zero mean and variance σ^2 . The polynomial function $f(x)$ is an approximation to $y(x)$ and can be a polynomial of any order. In this thesis, we employ quadratic polynomials for the approximation to $y(x)$:

$$\hat{y} = \beta_0 + \sum_{i=1}^k \beta_i x_i + \sum_{i=1}^k \beta_{ii} x_i^2 + \sum_{i=1}^k \sum_{j<i} \beta_{ij} x_i x_j. \quad (5.2)$$

The parameters, $\beta_0, \beta_i, \beta_{ii}$, and β_{ij} , of the polynomial in Equation 5.2 are determined through least-squares regression, that simply minimizes the sum of the squares of the differences between the predicted values, $\hat{y}(x)$ and the actual values, $y(x)$. The coefficients of Equation 5.2 can be obtained using following formula:

$$\beta = [X'X]^{-1} X'y, \quad (5.3)$$

where X is the matrix of sample point locations, X' is its transpose, and y is a column vector with the values of the response for each input vectors.

5.2.3 Kriging Model

The Kriging approximation technique, developed in the field of spatial statistics, has been drawing attention as an alternative to expensive CFD simulations. In theory, it is able to interpolate sample data and to model functions with multiple local extrema [109, 111]. Employing this interpolation technique one can create a surface fit from measured sample data using advanced statistical methods [113] (variations of the method of design of experiments (DOE)). While searching for data trends and global and local outliers, the ability of the Kriging method to capture multiple local extrema and even discontinuities (to some extent) is fundamental in global optimization and it was shown in previous work [52, 89, 92]. For those reasons, the Kriging model was employed as one of the multi-fidelity components in our multi-fidelity response surface approach.

The Kriging technique uses a two-component model that can be expressed mathematically as

$$y(\mathbf{x}) = f(\mathbf{x}) + Z(\mathbf{x}), \quad (5.4)$$

where $f(\mathbf{x})$ represents a global regression model and $Z(\mathbf{x})$ is the realization of a stationary Gaussian random function that creates a localized deviation from the global model [116]. The regression model, $f(\mathbf{x})$, is usually taken to be a polynomial of orders 0, 1 or 2. In this thesis, we adopt a zeroth order polynomial for the global regression model. If $f(x)$ is taken to be an underlying constant [111], β , equation 5.4 becomes

$$y(\mathbf{x}) = \beta + Z(\mathbf{x}). \quad (5.5)$$

The estimated model of Equation 5.5 is given as

$$\hat{y} = \hat{\beta} + \mathbf{r}^T(\mathbf{x})\mathbf{R}^{-1}(\mathbf{y} - \mathbf{f}\hat{\beta}), \quad (5.6)$$

where \mathbf{y} is the column vector of response data and \mathbf{f} is a column vector of length n_s which is filled with ones. \mathbf{R} in equation 5.6 is the correlation matrix which can be obtained by computing its elements $R(\mathbf{x}^i, \mathbf{x}^j)$, the correlation function between any

two sampled data points. This correlation function is specified by the user and the basis functions chosen used determine, to a large extent, the quality and behavior of the approximation. In this work, we use a Gaussian exponential correlation function of the form provided by Giunta, et al. [110]

$$R(\mathbf{x}^i, \mathbf{x}^j) = \exp \left[- \sum_{k=1}^n \theta_k |\mathbf{x}_k^i - \mathbf{x}_k^j|^2 \right], \quad (5.7)$$

where θ_k is a set of parameters determined by Equation 5.10. The correlation vector between \mathbf{x} and the sampled data points is expressed as

$$\mathbf{r}^T(\mathbf{x}) = [R(\mathbf{x}, \mathbf{x}^1), R(\mathbf{x}, \mathbf{x}^2), \dots, R(\mathbf{x}, \mathbf{x}^n)]^T. \quad (5.8)$$

The value of $\hat{\beta}$ is estimated using the generalized least squares method as

$$\hat{\beta} = (\mathbf{f}^T \mathbf{R}^{-1} \mathbf{f})^{-1} \mathbf{f}^T \mathbf{R}^{-1} \mathbf{y}. \quad (5.9)$$

Since \mathbf{R} is a function of the unknown variable θ , $\hat{\beta}$ is also a function of θ . Once θ is obtained, Equation 5.6 is completely defined. The value of θ is obtained by maximizing the following function over the interval $\theta > \mathbf{0}$

$$-\frac{[n_s \ln(\hat{\sigma}^2) + \ln |\mathbf{R}|]}{2}, \quad (5.10)$$

where

$$\hat{\sigma}^2 = \frac{(\mathbf{y} - \mathbf{f}\hat{\beta})^T \mathbf{R}^{-1} (\mathbf{y} - \mathbf{f}\hat{\beta})}{n_s}. \quad (5.11)$$

The best Kriging model can be constructed by solving the unconstrained nonlinear optimization problem given by Equation 5.10. We use the MATLAB function *fmincon* to find the maximum likelihood estimations for the θ parameters with simple lower and upper bound constraints.

In order to construct a Kriging approximation the only data required are the function values at a number of pre-specified sample locations. For many computational methods, secondary information such as gradient values may be available as a result

of the analysis procedure and can be used to enhance the accuracy and to lower the cost of the Kriging approximation [92].

The Kriging model has been successfully used in previous design work [92, 89, 90], however some practical difficulties should be noted. As the number of sample points grows, the size of the correlation matrix becomes larger and the computation time increases dramatically. Kriging calculations require the inversion of the correlation matrix and if the sample locations are evenly spaced (as is the case in LHS) this matrix is usually well-conditioned. However if some of the sample locations are clustered because of irregular initial sampling, or if the function is sampled at additional sites that cluster near a minimizer, the subsequent correlation matrix becomes ill-conditioned very quickly. Adding a small number to the diagonal of the correlation matrix has been suggested [126] to increase diagonal dominance.

5.2.4 Neural Network

Artificial Neural Network

Neural networks (NN) [128] have attracted interest from many fields including engineering, biology, medicine, economics and etc. They were intended to model the way in which the human brain processes visual data and learns to recognize objects. Their pattern matching and learning capabilities can be applied to approximating design spaces by nonlinear mapping where the networks are connected by weights and thresholds in the form of nonlinear functions. There are three components to this networks: a set of input nodes, one or more layers of 'hidden' nodes, and a set of output nodes as shown in Figure 5.2. The input nodes are not really neural at all: these nodes simply serve to introduce the values of the input variables. Hidden and output nodes arrange the linear form of a weighted sum of its inputs, and generalize the output with a nonlinear function $\phi(\cdot)$, called an *activation* function: The linear weighted sum of inputs, $\sum_{i=0}^d w_i x_i \equiv \mathbf{w}^T \mathbf{x}$ can be generalized to be the output of $\phi(\mathbf{w}^T \mathbf{x})$, where w_i are the weights and x_i ($i = 0, \dots, d$) are the inputs with x_0 corresponding to the bias, i.e., $x_0 = 1$. Then a NN becomes a nonlinear parametric modeling problem and the parameters can be fitted by training these network using

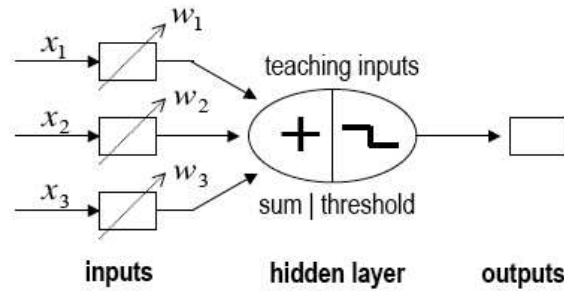


Figure 5.2: The schematic of Neural Network system

the initial data set.

The network connections among the three types of nodes can be either feedforward or recurrent. The simplest and most widely-used form is a feedforward network where the signals flow from inputs forwards through any hidden layers, eventually reaching the output nodes. The recurrent form of a network [129] is bi-directional and contains more complex dynamics, however it can be unstable and was not used in this thesis.

Here we employ one hidden layer, fully connected, feedforward neural network as in Figure 5.3. One important issue is the choice of activation functions which play a role as the threshold to fire the neuron (transfer the information) to the next layer. We have investigated three types of activation functions: sigmoid functions, exponential functions, and radial basis spherical/ellipsoid Gaussian functions.

- The logistic sigmoid function has the important properties that it is continuously differentiable and has a simple derivative form.

$$\phi(a) = \frac{1}{1 + e^{-a}} \quad (5.12)$$

- Exponential functions are important when solving systems of ODE and simulating the plane wave propagation of multiple signals

$$\phi(w; x) = \exp^{w^T \mathbf{x}} \quad (5.13)$$

- In a radial basis function network, the activation of hidden layers is determined

by the distance between input vector and prototypical/center vector. The general form of the activation function is $\phi(\|\mathbf{x} - \mu\|_2^2)$, where μ is a center vector and $\|\cdot\|_2$ is the L_2 norm. In this thesis, we adopt a spherical Gaussian function as the radial basis activation function,

$$\phi(x) = \exp\left(\frac{-\|\mathbf{x} - \mu\|_2^2}{2\sigma^2}\right), \quad (5.14)$$

where σ_j^2 is the variance.

A radial basis function network [121] is slightly different from the general NN. It is a three-layer feedforward network that uses a linear transfer function for the output units and a nonlinear transfer function (normally the Gaussian) for the hidden units. The radial function NN mapping is given by $\sum_{j=1}^m w_j \phi_j(x) + w_0$, where $\phi_j(x)$ can be replaced by Equation 5.14. The parameters which should be determined are the linear parameters, w_j and the nonlinear parameters used in $\phi_j(x)$. RBF networks usually employ an unsupervised learning algorithm where the basis function parameters cannot consider the information in the target set and therefore they may not be the optimum choice.

On the other hand, supervised learning algorithms can yield the simultaneous determination of linear and nonlinear parameters trying to match the target information. They use the data to adjust the network's weights and thresholds so as to minimize the error in its predictions on the training set.

Golub and Pereya [130, 131] proposed that the training of some types of neural networks becomes a separable nonlinear least-squares problem that can be solved by the Variable Projection method. The Variable Projection method is based on the idea of supervised learning algorithm.

Variable Projection Method: VARPRO

The best measure of accuracy of a NN is the sum of the squares of the differences between the NN output and the actual response for each input vector. Since we have a three-layer NN as in Figure 5.3, the weight parameters involved are the weights at each hidden node j : $\mathbf{w}_{h,j}$, and the weights for the output node: \mathbf{w}_0 . Then the final

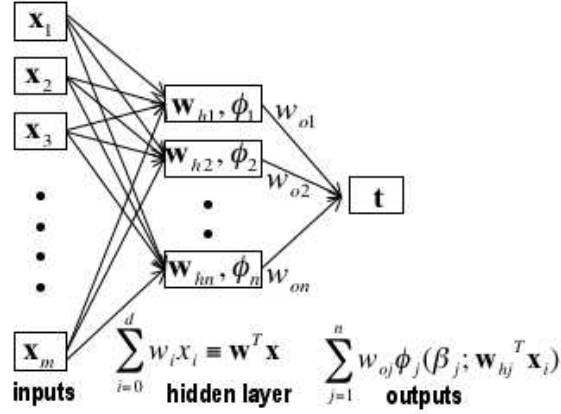


Figure 5.3: The schematic of Neural Network system for VARPRO

outputs can be approximated as a linearly weighted combination of the nonlinear activation functions:

$$\sum_{j=1}^n w_{0j} \phi_j(\beta_j; \mathbf{w}_{hj}^T \mathbf{x}_i), \quad (5.15)$$

if we have observed training data, (\mathbf{x}_i, t_i) , then the sum-of-squares error function (SSE) is given by

$$SSE = \min \frac{1}{2} \sum_{i=1}^m \left(\sum_{j=1}^n w_{0j} \phi_j(\beta_j; \mathbf{w}_{hj}^T \mathbf{x}_i) - t_i \right)^2. \quad (5.16)$$

If we rewrite the first tem in the right hand side of the Equation 5.16 as follows [130]:

$$\eta(\mathbf{a}, \alpha; \mathbf{x}) = \sum_{j=0}^n a_j \phi_j(\alpha_j; \mathbf{x}), \quad (5.17)$$

then the resulting separable nonlinear least squares problem is given by

$$\min_{\mathbf{a}, \alpha; \mathbf{x}} = \min_{\mathbf{a}, \alpha} \|\mathbf{t} - \eta(\mathbf{a}, \alpha; \mathbf{x})\|_2^2 = \min_{\mathbf{a}, \alpha} \|\mathbf{t} - \Phi(\alpha) \mathbf{a}\|_2^2, \quad (5.18)$$

where w_{0j} was replaced by a_j and both the \mathbf{w}_{hj} and β_j by α_j . The size of the training set is m , the number of hidden nodes is n , the linear output-node weights are a_j , and the α_j are the nonlinear parameters (the weights inside the activation

function associated with the hidden node j .) $\Phi(\alpha)$ is an $(m \times n)$ matrix function whose elements are $\Phi_{i,j}(\alpha) = \phi_j(\alpha_j; \mathbf{x}_i)$.

We should note that the parameters α and \mathbf{a} are separable and the *Variable Projection algorithm (VARPRO)* [130] takes advantage of this property and reduces the original problem into a smaller nonlinear problem. It divides the solution process into two steps: first it eliminates the linear parameters \mathbf{a} by introducing the pseudo-inverse of $\Phi(\alpha)$ such that $\mathbf{a} = \Phi^+(\alpha)\mathbf{t}$, where $\Phi^+(\alpha)$ is the Moore-Penrose generalized inverse of the rectangular matrix $\Phi(\alpha)$. Then reduced nonlinear problem for α is solved and the linear parameter \mathbf{a} is obtained in a post-processing step.

To summarize the problem is

$$\min_{\mathbf{a}, \alpha} \|\mathbf{t} - \Phi(\alpha)\mathbf{a}\|_2^2 = \|\mathbf{t} - \Phi(\alpha)\Phi^+(\alpha)\mathbf{t}\|_2^2 = \|\mathbf{P}_{\Phi(\alpha)}^\perp \mathbf{t}\|_2^2, \quad (5.19)$$

where the linear operator:

$$\mathbf{P}_{\perp(\alpha)}^\perp = (\mathbf{I} - \Phi(\alpha)\Phi^+(\alpha)), \quad (5.20)$$

is the projector on the orthogonal complement of the column space of $\Phi(\alpha)$. That is how the name *Variable Projection* is given to this solution procedure.

This procedure is implemented in the VARPRO algorithm [132] from Weidlinger Associates Inc. and we used VARPRO to test the accuracy of our response surface approximation to the real design space.

Comparison between VARPRO and Quadratic Fits

Since VARPRO is based on the nonlinear least squares problem, we compared the results between a least-squares regression model (quadratic fit) and VARPRO. Our test problem has the 16 geometric design parameters in the standard-PASS optimized configuration shown in Chapter 4, and the responses are the corresponding C_D value and three measures of ground boom loudness. The analysis was done using different fidelity tools corresponding to the accuracy in the solutions (responses): A502, CE and FE. The number of training points used is 5,217 and the sample points for validation (error computation) were kept separate and were not included in the initial

Response (baseline value)	RMS error in VARPRO (4 sigmoids)	RMS error in quad fit
C_D (0.0121)	0.000732	0.00071
Initial peak (0.9) of ground wave	0.078	0.092936
dBA0 (92.24)	0.70681	0.7418
dBA1 (79.44)	1.52041	1.5943
dBA3 (80.17)	0.91581	0.98585

Table 5.1: Accuracy of VARPRO and quadratic response surface given by the sum of the errors in different output functionals

training set. The RMS errors in those responses were compared between VARPRO and quadratic fit and are shown in Table 5.1. Four sigmoid activation functions used. As can be seen in Table 5.1, the RMS error is not much different between VARPRO and simple quadratic fit. Except for the error in the initial pressure rise of the ground wave, the relative % error is less than 7%, which is permissible in our work. The initial pressure rise was not used as an one of the objectives in our optimization work.

In addition, the effect of different numbers and types of activation functions on the accuracy of the NN response surface was investigated. Table 5.2 shows the RMS errors corresponding to several choices of activation functions. When we use a single type of activation function (for example the sigmoid), as the number of functions increases, the accuracy improves. However, the computational cost for the creation of a VARPRO model was rather expensive when compared with the simple quadratic fit as shown in Table 5.2, although not prohibitive: the computation time is of the order of minutes/hours for VARPRO and seconds for the quadratic fit. Considering the trade-offs between accuracy and computational cost, the slightly larger errors in the quadratic fit analysis are deemed permissible compared to the rather expensive additional computational cost for VARPRO. Therefore we employ the quadratic fit as another component of our multi-fidelity response surface instead of the VARPRO method when it comes to least-squares based fits. However, it should be noted that with enough computational time and an additional parallel computation algorithm, VARPRO is the better choice for accurate computation.

Activation function	C_D	dBA0	computation time (min)
4 sigmoids	0.000731965	0.70681	3
8 sigmoids	0.0006028	0.6329	25
12 sigmoids	0.00054436	0.602044	55.38
16 sigmoids	0.00050679	0.5740	105
32 sigmoids	0.000421	0.49446	405
4 gaussian(ellipsoid)	0.0008585	0.82997	1.5
4 gaussian(spherical)	0.00076121	0.77468	0.25
4 exponential	0.000734	0.73834	0.75
2 sigmoids & 2 exponentials	0.000710473	0.7357	2

Table 5.2: Error in prediction of response between VARPRO and Quadratic fit

5.3 Multi-Fidelity Response Surface

In section 5.2, several response surface methods were investigated and have been found to exhibit different characteristics regarding their ability to handle many sample points. We build the multi-fidelity response surfaces using a training set analyzed by the low- and high-fidelity analysis tools. Our multi-fidelity approach to the construction of the response surface fits relies on a hierarchy of four different aerodynamic analysis modules

1. PASS internal analysis based on classical aerodynamics and some empirical corrections.
2. A502/Panair supersonic linearized panel code.
3. Euler solutions using a mesh which is relatively coarse in the near-field (around 250,000 nodes for the complete configuration) - we refer to these computations by the label "Coarse Euler (CE)."
4. Euler solutions of the highest fidelity using several cycles of unstructured mesh adaptation (with a total of around 3-5 million nodes for the complete configuration) - we refer to these computations by the label "Fine Euler (FE)."

It should be noted that Coarse Euler (CE) analysis does not include the solution-adaptive mesh refinement in the near field and cannot predict the sonic boom propagation accordingly. It, however, has enough mesh resolution on the surface.

In order to obtain response surface fits of the highest fidelity one could carry out a large number of FE solutions and fit the resulting data (for both C_D and boom loudness). Unfortunately, for large dimensional design spaces (we will be using up to 25 design variables later on), accurate fits require a large number of function evaluations. This is particularly true in our case since the ranges of variation of each of the design variables will be rather large.

The main objective in this section is to generate response surface fits of the same quality/accuracy that would be obtained by evaluating the FE solutions only, but at a much reduced cost. We accomplish this by relying on a fundamental hypothesis that will be tested later on and for which we have already presented some evidence: *the higher fidelity tools are only needed in small regions of the design space where the lower fidelity models have exhausted their range of applicability*. This is bound to be true as it is the premise upon which aerodynamic design has been predicated for the last 50 years: aerodynamicists and engineers use the fastest tools for a specific purpose (when they are known to work well) and switch to more time-consuming, expensive tools only when they are needed. For example, in supersonic design, classical equivalent area concepts and linearized panel codes can provide very accurate results as long as nonlinear effects (such as transonic flows in the direction normal to the leading edge of the wing) are not present and viscosity does not play a dominant role in the solution of the flow.

With this in mind, we have used the following five-step procedure to create the response surfaces used in this work. All databases of candidate designs are obtained by populating the design space using a Latin Hypercube Sampling (LHS) technique. The following steps were used for Design I in Chapter 6, and the number of samples, the number of design variables, and the threshold values for the error correspond to Design I. The procedure is, however, general for the multi-fidelity response surface designs used later on (Designs I, and II in Chapter 6). The details of each design problem are presented in Chapter 6).

1. Run a large database of candidate designs obtained from ($> 8,000$) using the PASS aerodynamics module. Each evaluation takes roughly 3 seconds to compute on a modern workstation (Pentium 4, 3.2 GHz). This evaluation also flies each aircraft through the mission and returns a measure of the infeasibility of the design (an L-2 norm of the constraint violations.) Those designs that are found to significantly violate the requirements/constraints of the mission are removed from the database and are no longer considered in the response surface creation.
2. Run the remaining database of candidate designs using the A502/Panair solver. Each evaluation requires about 7 seconds of CPU time on the same modern workstation.
3. Select the design points whose relative error for C_D (based on the baseline design) is larger than a specified threshold, $\epsilon_{PASS-A502}$, and analyze only those designs using the Coarse Euler (CE) approach. In Design I, we have set this threshold to about 30% resulting in a number of CE evaluations in the neighborhood of 1,000. Each CE evaluation requires about 7 min on a modern workstation (5 minutes for the mesh generation and 2 minutes on 8 processors for the flow solution.)
4. We finally select the design points whose relative error for C_D (again based on the the baseline design) is larger than $\epsilon_{CE-A502}$ and analyze those designs using the Fine Euler (FE) approach. This threshold was set to 25% in our work, resulting in approximately 500 FE solutions. Each FE evaluation, from beginning to end, including geometry and mesh generation and adaptation (the bottlenecks in the process, since they are run serially) requires about 30 minutes of wall clock time. The flow solution portions (using AirplanePlus) are run in parallel using 16 Athlon AMD2100+ processors of a Linux Beowulf cluster.
5. Baseline quadratic response surface fits (using least squares regression) are created for the C_D and boom results for A502/Panair. The difference between the FE evaluations and the predictions of these quadratic fits is approximated with

a Kriging method, and the resulting approximation is added to the baseline quadratic fits.

In sum, the response surfaces are the addition of the quadratic fits based on the A502/Panair results and the Kriging fits to the difference between the FE solutions and those quadratic fits. The constructed multi-fidelity response surface is then provided to PASS to replace the classical aerodynamic analysis module inside PASS to guarantee the accuracy close to the high-fidelity Euler analysis.

The criterion for switching from a low-fidelity analysis to a high-fidelity analysis is one of the fundamental issues in variable-fidelity optimization. The criterion in our multi-fidelity procedure has, to some extent, the flavor of Richardson's extrapolation in that it recursively uses results from different fidelities to arrive at a final answer/fit. It also has an adaptive nature to it, as results from the higher fidelity models are only evaluated in areas of the design space where the lower fidelity models are found to be insufficiently accurate. If the hierarchy of models is chosen in such a way that the areas where the lower fidelity models fail are small compared with the size of the design space, then the procedure described above should be quite effective in producing results that are of nearly high-fidelity over the *entire* design space. Our experience shows that this is the case for aerodynamic performance: the PASS aerodynamic module is quite good at predicting the absolutely best wing (lower bound estimate on the C_D) that could be produced if considerable design work were done on the configuration (potentially using adjoint methods and a high degree of shape parameterization). However, it is unable to predict some of the finer details of aerodynamic performance and certainly fails when transonic effects are present. A502/Panair is also unable to deal with transonic flow effects (as was shown in section 4.3.1) but produces more realistic results than the PASS analysis as the actual geometry of the configuration is truly accounted for. Finally, the Euler models (CE and FE) are quite good predictors of the aerodynamic performance of the complete aircraft as long as viscous effects are not dominant. It must be mentioned that, if sonic boom were not an issue in these designs, the CE evaluations would be sufficient as the differences in C_D between CE and FE are found to be insignificant (less than 4 counts) over the large range of variations pursued in this work.

5.3.1 Number of Sample Points

The effect of the number of samples on the accuracy of response surface has been investigated. In the interest of computational efficiency, the smallest number of sample points that guarantees the accuracy of the response surface should be used. This number depends on the size of the design space to be approximated, which can be determined by the number of design variables and the range of design variable variation.

The accuracy of the response surface as a function of number of sample points is plotted in Figure 5.4 as relative errors. The design space we explore in this study has a maximum of 25 design variables as in Design II in Chapter 6. The results in Figure 5.4 are obtained for the corresponding design space. The analysis was done with A502/Panair that has somewhat inexpensive computational costs. Unreasonable noise in the output resulting from the limitations of A502/Panair were removed by enforcing lower and upper bounds and excluding those sample points in the training set for a response surface creation. A multi-dimensional quadratic fit, which was explained in detail in section 5.2.2 was used, since it is able to handle a large number of sample points. C_D was used as the aerodynamic performance measurement, and the initial peak of the ground boom and three types of noise metric were used for boom performance measurements. The number of sample points varies from 350 to 35,000. For this particular design space and response surface method, about 5,000 sample points appear to be enough to achieve converged accuracy.

In our optimization work (Design II) in Chapter 6 which has the same 25 design variables, we included about 5,000 sample points to construct the response surface, therefore this experiment proves that the number of training data in our work is appropriate (albeit not excessive).

5.4 Gradient-free Optimizer

The nature of the design spaces that result from these multi-disciplinary systems was shown to be noisy and ill-behaved in a previous section, and therefore, in general,

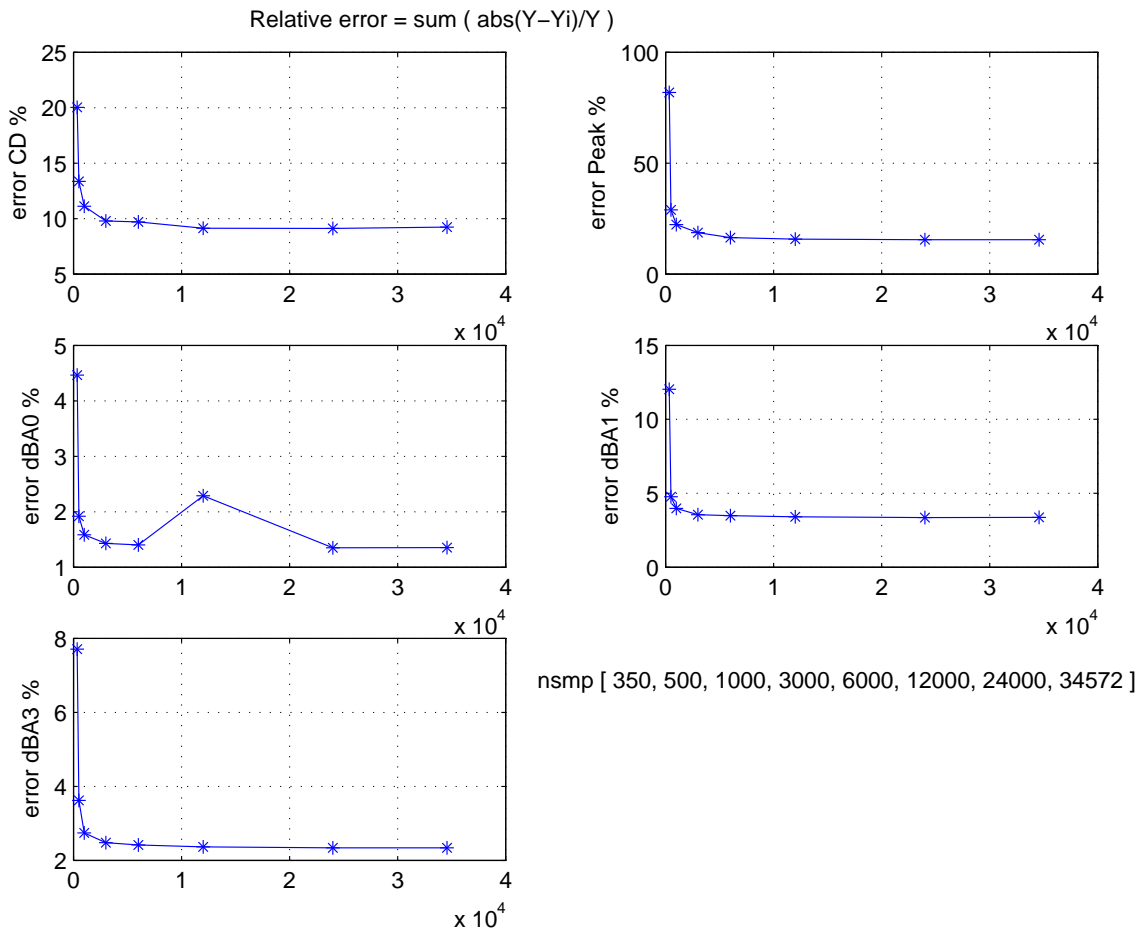


Figure 5.4: The effect of number of the samples on the relative error

may only be amenable to non-gradient based optimizers. We have used either the SIMPLEX method or Genetic Algorithms(GAs) for this phase of the design [101, 92, 31, 89, 93, 91].

However non-gradient based optimizers have often been criticized for their relatively expensive computational cost for a large number of function evaluations and impose severe limits on the maximum number of design variables that can be used.

5.4.1 Nonlinear SIMPLEX Method

The nonlinear Nelder-Mead SIMPLEX method [141] is a simple optimization algorithm seeking a set of design variables corresponding to the global extremum (maximum or minimum) of any n -dimensional objective function $F(x_1, x_2, \dots, x_n)$. It is based on a number of simple rules. The starting point is used to construct a *simplex*, a shape with $m + 1$ points, where m is the number of design variables or the dimensionality of the design space. Thus for a two parameter problem, for example, there are three points (a triangle). Three main operations are used: reflection, extension and contraction. With these three operations, the SIMPLEX method explores the design space and tries to bound the "search area" and find extrema.

The search is terminated when no more significant improvement of the response is observed when moving from one simplex to the next and/or the displacements are insignificant.

The SIMPLEX algorithm is fairly simple to implement and does not require derivative information. However it should be noted that when there are local extrema, it is highly probable the algorithm will fail and get trapped there, instead of identifying the global extremum. Drastic increases in the computational cost limit the number of design variables that can be used with the SIMPLEX method and the convergence is not always guaranteed [142, 143] This SIMPLEX algorithm is implemented as a module inside PASS and the mission requirement values are handled as nonlinear constraints in the SIMPLEX.

5.4.2 Genetic Algorithms

Genetic Algorithms (GAs) have been widely used as a stochastic search method. The theory is based on human evolution process and employs genetic operations, such as selection, crossover, mutation and reproduction. Each individual (object) is represented as a chromosome and the GA operates on a population of chromosomes and applies genetic operators to produce the best offspring and proceed to the next generation. Just like other global optimizers, GAs do not require gradients or mathematically complex formulas and thus they are easy and simple to implement and can

handle various data representations for different problems with one algorithm.

Single vs. Multi Objective Optimization

The minimization of sonic boom has often conflicted with the other disciplines in the design problem. Mission requirements should be considered as a set of nonlinear constraints as well in order to produce realistic results. This is the setup of a typical single optimization problem. When several criteria are considered, the optimal solution is generally not unique since no point achieves optimality with respect to all objectives simultaneously. A *nondominance* criteria [133] is better suited for this type of the multi-disciplinary optimization. The family of nondominated individuals suggest a set of solutions which are superior to the rest with respect to all objective criteria, but are inferior to other solutions in one or more objectives, and they are often called the *Pareto set* [133].

Genetic Algorithms (GAs) can use this dominance criteria in a straightforward fashion to drive the search process toward the Pareto front. During the stochastic search, GAs explore the entire feasible space and build a database of solutions which can be thought of as a cloud of points. At convergence, the cloud does not evolve any more and its convex hull determines the optimal Pareto set. Due to the unique features of GAs, which work with a population of solutions, multiple Pareto optimal solutions can be captured in a single run. First, the GA applies non-dominance definitions to each individual according to their fitness value, but in a multi-objective optimization problem, several criteria are assigned instead. Therefore, to evaluate the fitness of the individuals, a ranking algorithm is necessary. Many of the Multi-Objective Evolutionary Algorithms (MOEA) are criticized by their computational complexity related to the ranking/sorting of the individuals by comparing their fitness and the need for specifying sharing parameters. Our results in multi-objective optimization are based on the algorithm of Srinivas and Deb: the Non-dominated Sorting Genetic Algorithm (NSGA) [134]. The NSGA-II algorithm was used to alleviate the above problems and has shown fast convergent rates [135]. It uses the non-dominated sorting procedure as a ranking selection method which emphasizes the optimal points, where the sharing technique, or niche method, is used to stabilize

the subpopulations of the ‘good’ points. Once the set of optimal solutions is identified, it is left to the designer to choose one solution out of many possible ones. This is the primary reason that makes GAs ideally suited for multi-objective optimization.

However in an optimization problem which involves a large number of design variables, a bigger population and a larger number of generations may be required, and the corresponding computation cost may be prohibitive. One of the advantages of GAs is that the fitness evaluation for each individual can be done in parallel [136]. Even though parallel GAs were implemented in this thesis, a sequential version of GA was sufficient for the number of design variables used (25) and the two objective functions in the problem.

Two examples of previous dual-objective optimization work are shown in Figures 5.5 [92] and 5.6 [89]. For both cases, the Pareto fronts were obtained based on a Kriging response surface representation of the design space. Validation by high-fidelity Euler analysis is illustrated in the plot as well. Figure 5.5 shows the results from previous unconstrained optimization work [92], and Figure 5.6 from the simple constrained optimization work [89].

5.5 Gradient-based Optimizer

If the design space is smooth, continuous, and well-behaved, and gradient information is available everywhere, gradient/sensitivity information can provide very useful input for the search directions to follow in the design space. This can contribute to reducing the number of function evaluations and to accelerating the optimization process. In addition, gradient information allows us to test well-formulated optimality conditions so that the optimization process can be driven in a way that convergence can be guaranteed.

The necessary information are the gradients, Jacobian and Hessians of the cost/objective function and constraints with respect to the design variables. The ideal way to obtain gradient information is to differentiate an analytical solution to the system. Although analytical solutions can be found for simplified problems such as Laplace’s equation or

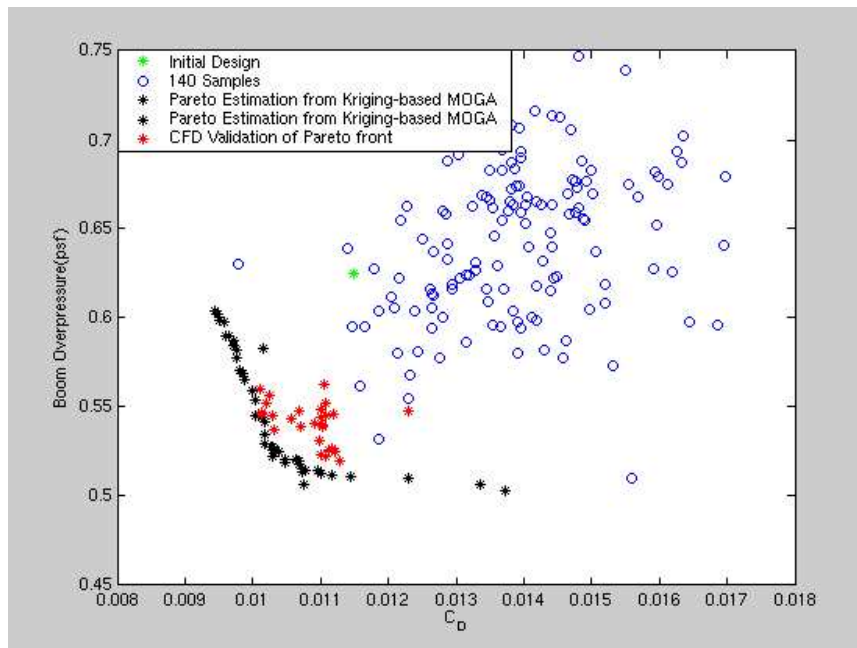


Figure 5.5: Pareto front from multi-objective optimization without constraints. From [92]

Poisson's equation for a simple geometry, it is usually very difficult to obtain analytical solutions as in the case of our problem. There have been several ways to calculate the gradients, and the most widely-used methods, the finite difference method, the complex-step method, and the adjoint method are briefly introduced.

5.5.1 Finite difference method

A traditional way to calculate the gradients is the finite difference method (FDM). Additional function evaluations are required with perturbed parameter values (step sizes) and these increase the computational cost dramatically if a large number of design variables are involved. For satisfactory accuracy in the finite-difference gradient, a range of step sizes must be tried instead of a single value of step size, which often leads to mN computational cost for the entire gradient evaluation, where m is the number of different step sizes and N is the number of gradient evaluations required.

An example of an estimate of the first derivative of a objective function f using a

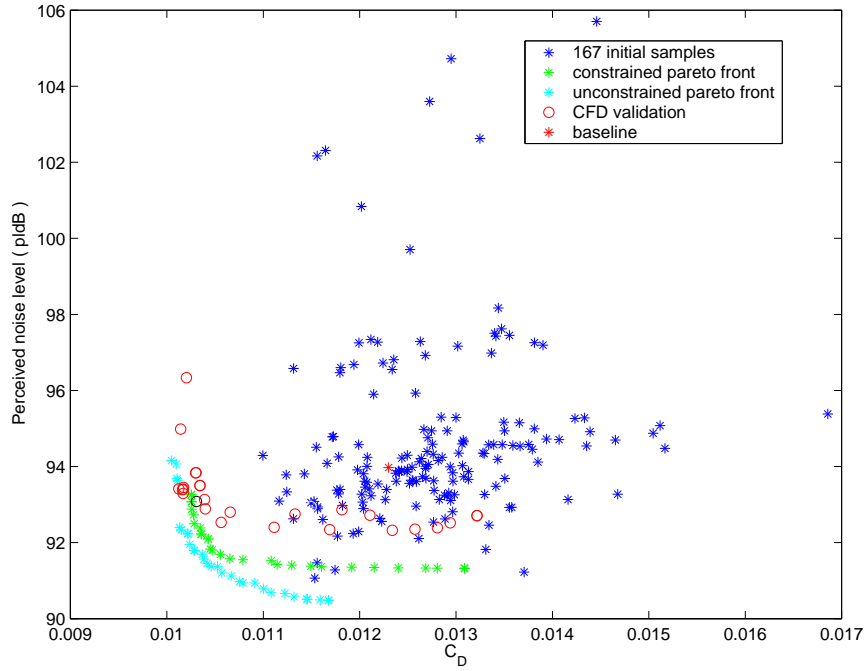


Figure 5.6: Pareto front from multi-objective optimization with simple constraints. From [89]

first-order forward-difference approximation is as follows:

$$\frac{\partial f}{\partial x_i} = \frac{1}{\delta x_i} [f(\dots, x_i + \delta x_i, \dots) - f(\dots, x_i, \dots)] = \frac{f(x_i + \delta x_i) - f(x_i)}{\delta x_i} + \mathcal{O}(\delta x_i), \quad (5.21)$$

where δx_i is the step size in the design variable. From Equation 5.5.1, to reduce the truncation error $\mathcal{O}(\delta x_i)$ a small step size is desired, which increases the subtractive cancellation errors and this error related to the step sizes are the main drawback for the FDM. On the contrary, the complex-step method shows very good accuracy with a small step sizes.

5.5.2 Complex-step method

The error related to subtractive cancellation with small step sizes can be reduced by the complex-step method [144]. An objective function is expanded with a Taylor series and the step size is added to the imaginary part of the objective function. A brief mathematical formula follows:

$$f(x + i\delta x) = f(x) + i\delta x f'(x) - (\delta x)^2 \frac{f''(x)}{2!} - i(\delta)^3 \frac{f'''(x)}{3!} + \dots \quad (5.22)$$

If we divide the imaginary parts of the above equation by δx , then a second order complex-step approximation to the first derivative of $f(x)$ can be obtained by

$$f'(x) = \frac{\text{Im}[I(x + i\delta x)]}{\delta x} + \delta x^2 \frac{f'''(x)}{3!} + \dots \quad (5.23)$$

As can be seen in the above equations, no subtractive cancellation error is involved in this method and higher accuracy is guaranteed as the step size is decreased. Therefore the complex-step method is more robust and does not require a range of step sizes as in FDM. However the real and imaginary parts of complex numbers increases the computational time compared to a single evaluations of the finite-difference method by approximately a factor of 2 [138].

5.5.3 Adjoint method

The adjoint method is a very efficient method to obtain gradient information with respect to an arbitrary number of design variables by solving an adjoint equation. This requires that the additional adjoint equation be solved for each objective/cost function. Thus this method can be useful in problems that have a large number of design variables and relatively few objective functions.

The basic theory and methodology of the adjoint method has been presented numerous times before and will not be repeated here. The reader is referred to [151, 152] for more details of the actual formulation and for representative design calculations using this method. By now, the adjoint method has been used for a very large number of design calculations in all flow regimes: low-speed high-lift configurations,

transonic designs, and supersonic configurations. This method has been applied in both academic and industrial environments is by now a fairly established procedure.

In the local search steps in our work, an adjoint solver has been used to calculate gradient information with respect to all the design variables in a short amount of time.

5.5.4 NPSOL Sequential Quadratic Programming Optimizer with Adjoint Solver

The design programs SYN87-SB and SYN107-MB are coupled to a nonlinear constrained optimization package, NPSOL [102, 103]. NPSOL is a sequential quadratic programming (SQP) method incorporating an augmented Lagrangian merit function and a BFGS(Broyden [145]-Fletcher [146]-Goldfarb [147]-Shanno [148]) quasi-Newton approximation to the Hessian of the augmented Lagrangian. The algorithms used in NPSOL are numerically stable and are guaranteed to converge to a local optimum, if the design space is locally smooth enough.

Chapter 6

Optimization Results

In this Chapter, the results of two different design optimization cases that use the procedures outlined earlier will be presented. A brief summary of the complexity and approach of these optimization cases is shown in Table 6.1. The design goal is: for Mach number 1.6, 6-8 passenger supersonic business jet configuration with a range of 4,000 nmi and with a T/O field length that does not exceed 6,500ft. The two optimization problems use the same baseline configuration in Section 6.1 as a starting point. The same mission profile is specified for each design case. Specific details regarding the differences in approach for both optimization problems are presented in the following sections. The optimization runs using the SIMPLEX method included in the PASS software were performed by Mr. Mathias Wintzer (Desktop Aeronautics, Inc.) and the some figures for the PASS optimization results (Figures 6.2, 6.8, 6.11, 6.12, 6.13 and 6.18) are also courtesy of Mr. Mathias Wintzer.

In the first section, the simultaneous minimization of the maximum take-off gross weight (MTOW) and of the ground boom loudness is pursued. Due to the ill-behaved

Design	number of parameters	objectives	Optimizer	MDAs	Scope
Design I	18	boom & MTOW	SIMPLEX	PASS,A502,CE,FE	Global
Design II	25	MTOW	SIMPLEX & NPSOL(adjoint)	PASS,A502,FE + Local	Global

Table 6.1: Optimization problem definition for Designs I and II.

characteristics of boom responses for a design space, only a global search method was implemented. For this purpose, a multi-fidelity response surface which contains the full hierarchy of our analysis tools has been used.

A two-level optimization which carries out a global search (such as the one used in Design I) followed by a local search is demonstrated in section 6.3. Since the use of an adjoint-based local search in the noisy and discontinuous sonic boom design space is not yet practical, only single-objective optimizations were investigated for the two-level optimization process.

All the design optimization cases increase the efficiency of the procedure by using the multi-fidelity response surface approach presented earlier. However, the details of the implementation of the multi-fidelity response surface technique vary from one design case to the other depending on the particulars of the optimization problem. The design variables are also selected differently for each case. PASS does not internally store detailed surface information (particularly the twist and camber distributions, although it assumes an optimal choice) and therefore it is impossible to have certain design variables related to the wing section. Consequently the aerodynamic prediction module in PASS only plays a role in the design by providing a criterion to switch from low/mid- to high-fidelity analyses. A total of 18 design variables were used in Design I, while wing section changes were considered and a total of 25 design variables were chosen in Design II (for the global search). Additional design variables were added for the local, adjoint-based, portion of the search procedure in Design II.

6.1 Baseline Configuration

6.1.1 Standard-PASS Optimization

A baseline geometry for Designs I and II (in Section 6.2 and 6.3) was generated by running the standard version of PASS for a mission with the performance objectives summarized in Table 6.4 and 6.5. PASS consists of two separate components:

1. A mission analysis module: the geometric parameters and flight conditions in Table 6.2 are input into the PASS mission analysis module and a large number

of output variables (shown in Table 6.2) are calculated.

2. A nonlinear constrained SIMPLEX optimizer: the SIMPLEX optimizer is used to minimize the MTOW of the aircraft while satisfying the mission constraints summarized in Table 6.5. This SIMPLEX optimization module is directly connected to the mission analysis module for the necessary function evaluations and tries to find the best set of input design variables to produce a minimum MTOW, while satisfying all mission constraints.

The SIMPLEX optimization procedure was used to generate the baseline configuration which is shown in Figure 6.1. The geometric details of this configuration are shown in Table 6.3. Since the mission analysis module is based on the theoretical aerodynamics, the details of the wing sections (airfoil shape, camber, and twist) are not known at this level and they are highlighted in blue in Table 6.3 and initialized using default values based on previous experience. The actual mission parameters for this baseline are shown in Table 6.5

Mission requirements and geometric constraints for the baseline configuration were based on numbers representative of current industrial interest. In an effort to generate an aircraft achievable using current levels of technology, advanced technology assumptions were kept to a minimum. The main purpose of our multi-disciplinary optimization is to generate aerodynamic and boom performance improvements from this standard PASS-optimized configuration by using high-fidelity analyses.

6.1.2 Design Variables

The final values of the design variables of the PASS-optimized baseline configuration are provided in Table 6.3. These are then used as initial values for the subsequent optimizations. Note that the values highlighted in red were not allowed to vary during the optimizations. The variation in the incidence angles at the three defining wing sections and of the maximum camber (highlighted in blue) is only permitted in Design II, and is not considered for Design I. Therefore we can expect larger improvements in the aerodynamic performance in Design II: this will be shown in

PASS mission analysis inputs
Mach number
MTOW
Sref (trapezoidal (trap) wing area) of wing & tails
AR (aspect ratio)
thickness to chord ratios of wing and tails
taper of wing and tails
leading edge extension of wing and tails
trailing edge extension of wing and tails
dihedral angle of wing and tails
location of wing root leading edge on the fuselage
quarter chord sweep of wing and tails
dihedral angles of wing and tails
alphalimit (maximum AOA limit at $C_{L_{max}}$)
engine type
engine location
uninstalled sea level static take-off thrust for one engine
ratio of actual SFC to reference engine SFC
flap & slat deflection angles during the full mission stages
span and chord of flap
ratio of gear track to fuselage width
altitudes during the full mission stages
payloads (passengers, crews, baggage and cargo)
fuselage layouts (nose/tailcone fineness ratio, width, height, radii)
$C_{L_{max}}$ of horizontal tail
PASS analysis outputs
cruise range
second segment climb gradient
FAR balance take-off/landing field length
drag to thrust ratio (D/T) at cruise points
lift to drag ratio(L/D) at cruise points
total C_D (including parasite drag, induced drag, compressibility drag)
drag divergence Mach number
load factors (limit/ultimate)
minimum stability
chordwise position (x/c) of landing gear on wing
C_L margins for wing, tails during the full mission stages
C_L during the full mission stages
equivalent flat plate parasite drag area for the components
components weights
weights during the full mission stages
SFC (Specific Fuel Consumption)
total available thrust
fuselage length & width

Table 6.2: Input and Output parameters for PASS mission analysis

Wing reference area (S_{ref})	1,025 ft ²
Wing aspect ratio (AR)	3.526
Wing quarter-chord sweep (Λ)	54.96°
Wing taper	0.15
Wing dihedral	3°
Leading edge extension	0.5
Trailing edge extension	0.199
Break location	0.4
Location of wing root LE	0.249
Root section t/c	2.23%
Break section t/c	2.63%
Tip section t/c	2.71%
Root section twist	0.0
Break section twist	0.0
Tip section twist	0.0
Root section maximum camber location	0.279
Break section maximum camber location	0.345
Root section maximum camber	0.0
Break section maximum camber	0.0
Vertical tail area (% S_{ref})	0.125
Vertical tail AR	0.65
Vertical tail Λ	56°
Vertical tail λ	0.6
Horizontal tail area (% S_{ref})	0.6
Horizontal tail AR	2.0
Horizontal tail Λ	56°
Horizontal tail λ	0.3

Maximum fuselage length	125 ft
Minimum cockpit diameter	60 inches
Minimum cabin diameter	78 inches
Cabin length	25 ft

Cruise Mach	1.6
MTOW	85,809 lbs
Alpha limit	15°

Table 6.3: Geometric design parameters for the baseline configuration.

Range	4,000 nmi
BFL	6,500 ft
Minimum static margin	0.0

Table 6.4: Some of mission constraints goal (details are in Table 6.5.)

Constraint	baseline value	Min. Value	Max. Value
Cruise range(n.mi.)	4010.6	4,000	N/A
TOFL (ft)	5433.6	N/A	6,500
LFL(ft)	4714.4	N/A	6,500
Minimum stability	0.0145	0.0	N/A
Vertical tail CL for engine out condition	0.1	-1.0	1.0
Second segment climb gradient	0.0372	0.024	N/A
Main gear location as fraction of chord length	0.8572	0.6	0.95
Initial cruise-climb gradient	0.00508	0.005	N/A
Final cruise-climb gradient	0.00558	0.005	N/A
Horizontal tail CL margin, takeoff	0.98377	0.0	N/A
Horizontal tail CL margin, takeoff rotation	0.47328	0.0	N/A
Horizontal tail CL margin, climb	1.1064	0.0	N/A
Horizontal tail CL margin, initial cruise	0.8554	0.0	N/A
Horizontal tail CL margin, final cruise	0.86091	0.0	N/A
Horizontal tail CL margin, landing	0.96766	0.0	N/A
Wing CL margin, climb	0.4201	0.0	N/A
Wing CL margin, initial cruise	0.8554	0.0	N/A
Wing CL margin, final cruise	0.8609	0.0	N/A
Elevator deflection, takeoff rotation	-14.55	-25.0	N/A
Elevator deflection, takeoff	-0.4671	-10.0	N/A
Elevator deflection, climb	0.039569	-10.0	N/A
Elevator deflection, landing	-10.535	-15.0	N/A

Table 6.5: Mission analysis values for the baseline and bounds for optimization runs.

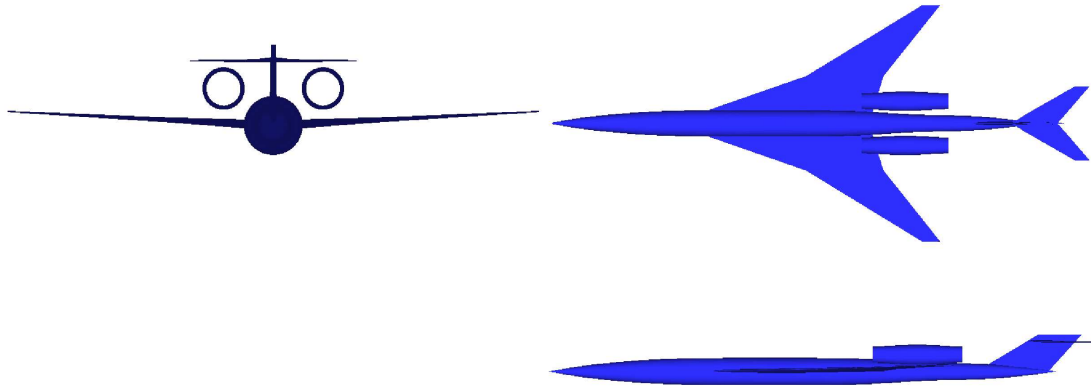
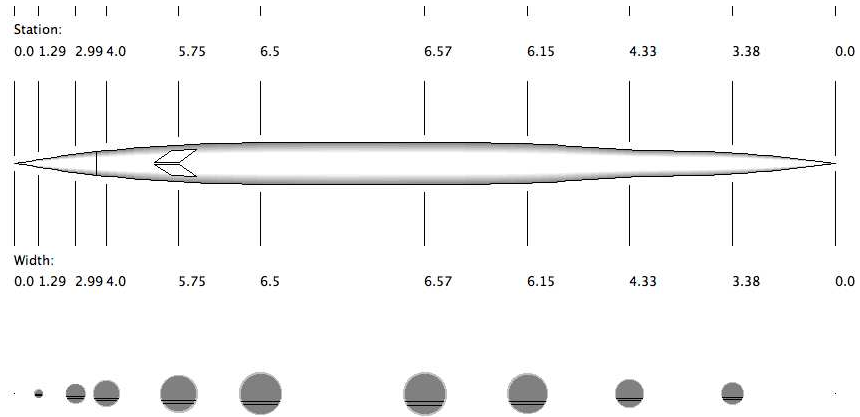


Figure 6.1: Three-view drawing of baseline PASS-optimized configuration

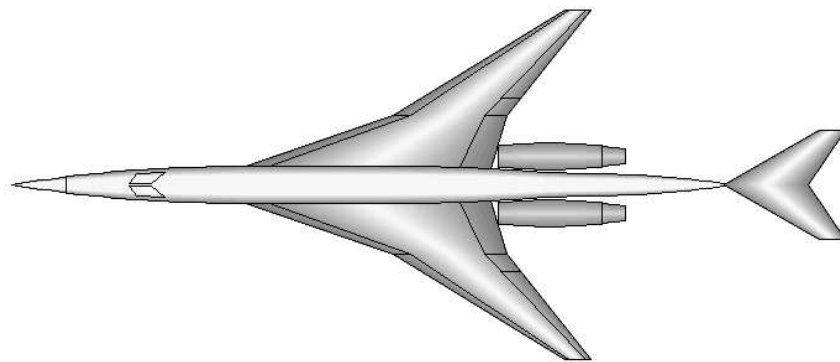
Section 6.3. In addition to these variables, a total of 6 variables representing the radii of fuselage stations located at 3%, 7.5%, 11.25%, 62.5%, 75%, and 87.5% of the fuselage length were added to allow for both performance improvements and boom tailoring (were the design problem definition required it), and to maintain cabin and cockpit compartment constraints. The outer mold line of the fuselage was generated by fitting an Akima spline to the specified radius distribution. Note that the allowable ranges for all of the design variables (for the baseline configuration and all subsequent designs) were rather large, being at least $\pm 30 - 40\%$ of their baseline values. This large range of variations allows for a more complete design space to be searched but also makes the job of both the optimization algorithm and the response surface fitting techniques more complicated. The values of the leading and trailing edge extensions are normalized by the trapezoidal wing root chord. The location of the wing root leading edge is normalized by the fuselage length and is measured from the leading edge of the fuselage. Both the vertical and horizontal tail areas are normalized by S_{ref} . Some design variables defining wing planform are shown in Figure 6.4

6.1.3 Mission Profile

This baseline geometry, according to PASS, meets all of the requirements of the mission specified in Table 6.4 as can be seen in the mission profile in Figure 6.3. Note



(a) Fuselage layout and stations



(b) Top view of configuration

Figure 6.2: Summary of baseline configuration.

Design I	Design II	Variable	Min. Value	Max. Value
x_1	x_1	S_{ref} (ft ²)	1,000	1,300
x_2	x_2	Wing aspect ratio (AR)	3.0	5.0
x_3	x_3	Wing quarter-chord sweep (Λ)	45°	60°
x_4	x_4	Location of wing root LE	0.2	0.4
x_5	x_5	Leading edge extension	0.0	0.75
x_6	x_6	Trailing edge extension	0.0	5.0
x_7	x_7	Root section t/c	2.0%	3.0%
x_8	x_8	Break section t/c	2.5%	3.5%
x_9	x_9	Tip section t/c	2.0%	3.0%
N/A	x_{10}	Root section twist	-1	2
N/A	x_{11}	Break section twist	-2	1
N/A	x_{12}	Tip section twist	-5	-2
N/A	x_{13}	Root section maximum camber location	20.0%	40.0%
N/A	x_{14}	Break section maximum camber location	20.0%	40.0%
N/A	x_{15}	Root section maximum camber	0.0%	1.0 %
N/A	x_{16}	Break section maximum camber	0.0%	1.0 %
x_{10}	x_{17}	Fuselage station 2 radius / fus. length (x = 3.75 ft)	0.005	0.020
x_{11}	x_{18}	Fuselage station 3 radius / fus. length (x = 9.37 ft)	0.005	0.020
x_{12}	x_{19}	Fuselage station 4 radius / fus. length (x = 14.06 ft)	0.005	0.020
x_{13}	x_{20}	Fuselage station 8 radius / fus. length (x = 78.12 ft)	0.015	0.035
x_{14}	x_{21}	Fuselage station 9 radius / fus. length (x = 93.75 ft)	0.010	0.030
x_{15}	x_{22}	Fuselage station 10 radius / fus. length (x = 109.37 ft)	0.005	0.020
x_{16}	x_{23}	Max TOGW (lbs)	80,000	100,000
x_{17}	x_{24}	Initial cruise altitude (ft)	39,902	44102.1
x_{18}	x_{25}	Final cruise altitude (ft)	51,490	56,910

Table 6.6: Bounds for geometric design variables and for sample distribution for response surface generation.

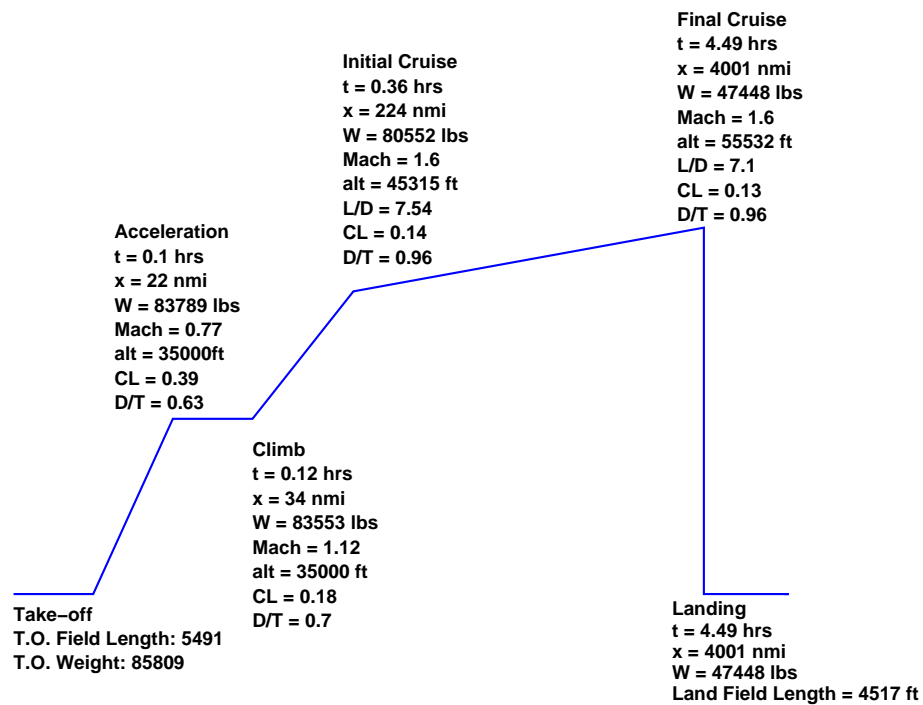


Figure 6.3: Mission profile (analyzed by standard PASS) of baseline configuration

that no attempt to minimize or tailor the ground boom signature has been made in this design. Furthermore, this design can be considered a *best-case* scenario since it was calculated using the aerodynamic prediction module in PASS, which computes coefficients of drag that can be assumed to represent a lower bound estimate. This is due to the fact that the aerodynamic prediction module inside PASS is based on certain theoretically-realistic assumptions related to the shape of the spanwise and longitudinal lift distributions when computing inviscid drag. However the twist angles and maximum cambers corresponding to this ideal wing are not known at this PASS analysis/design level. If the C_D information provided by the high-fidelity analyses were to be identical to the information provided by this PASS model, then the same aircraft ought to be able to fly the mission and complete it while satisfying all of the constraints that were imposed on the original baseline design. Though achievable in principle, these estimates for best possible performance can in practice only be attained with a significant high-fidelity CFD design effort.

For subsequent optimization runs, the optimizer was configured such that the

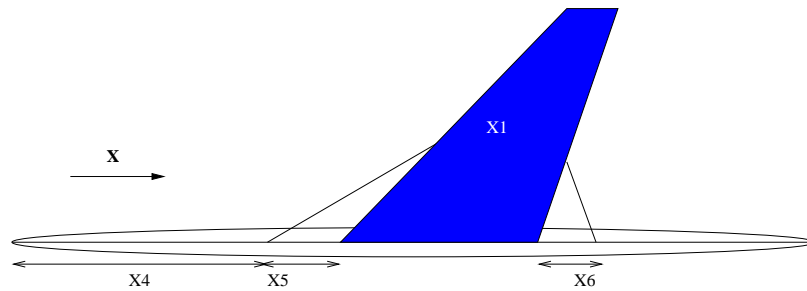


Figure 6.4: Design variables for wing planform

input variables and associated bounds mirrored the perturbation values used in generating the response surfaces. These inputs and bounds are summarized in Table 6.6. The design constraints presented in Table 6.5 were also imposed.

Re-evaluation of Mission Profile

Noting the differences between PASS and the high-fidelity CFD analyses, the baseline case was re-evaluated with a modified version of PASS where the aerodynamic module for the cruise segment was replaced with direct high-fidelity CFD evaluations. Given that the baseline geometry is evaluated without any knowledge of the actual twist and camber distributions, it is not surprising that without additional design work, the drag reported by the CFD evaluations was substantially higher than that reported by PASS. The aerodynamic module in PASS reports an inviscid drag coefficient at the beginning of the cruise segment of $C_{D_{PASS}} = 0.0079$, while that of the Euler analysis is, as expected, substantially higher, $C_{D_{EULER}} = 0.0117$. The results of this analysis using the information from the Euler analysis is presented in Table 6.7. It is clearly apparent that both the cruise range and L/D ratio have decreased by a large amount, and that the baseline design does not have a sufficient climb gradient at either the beginning or end of cruise conditions. The numbers for cruise L/D are based on the total C_D with contributions resulting from inviscid and viscous drag. The value of the L/D ratio is calculated inside the PASS module using the high-fidelity values for the aerodynamic performance of the configuration during the cruise condition. Notice also that the predicted loudness (from the Euler analysis using mesh adaptation) is 81.12 dBA. The results from PASS do not provide us with a value of the boom loudness

Performance	standard PASS	PASS + Euler
Range	4010 n.mi.	3381 n.mi.
BFL	5434 ft	5434 ft
L/D at initial cruise	7.55	6.30
L/D at final cruise	7.13	5.95
Ground signature (dBA)	N/A	81.12
Climb gradient at initial cruise	0.0051	-0.02436
Climb gradient at final cruise	0.0056	-0.0254

Table 6.7: Results of PASS + Euler surface analysis of the baseline configuration.

since the details of the flow field are not known in its aerodynamic module.

The results presented in this section are of fundamental importance since, in some senses, two of the main points of this study are to first see how close we can get to the performance of the PASS baseline design when using the higher-fidelity models and, second, what additional work (and methods/tools) is required to obtain such a design.

6.2 Design I: Multi-fidelity and Multi-Disciplinary Optimization of Supersonic Jets

In Chapter 4 we have investigated a hierarchical multi-fidelity design approach where high-fidelity models are only used where and when they are needed to correct the shortcomings of the approximations inherent in the low-fidelity models. Our design approach consists of two basic components: a multi-disciplinary aircraft synthesis tool (PASS) that uses highly-tuned low-fidelity models of all of the relevant disciplines and computes the complete mission profile of the aircraft, and a hierarchical, multi-fidelity environment for the creation of response surfaces for aerodynamic performance and sonic boom loudness (BOOM-UA) that attempts to achieve the accuracy of an Euler-based design strategy with significantly lower cost.

6.2.1 Multi-Fidelity Response Surface

The procedure of constructing the multi-fidelity response surfaces is described in Chapter 5 in detail, where the five steps required were explained, and therefore only a short summary is provided in this section. Figure 6.5 shows the results of the over 5,000 candidate designs evaluated using A502/Panair that are retained after the initial filtering of over 8,000 PASS results. The red dots in the Figure indicate those candidate designs for which the predicted values of C_D differ by more than $\epsilon_{PASS-A502} > 30\%$ between PASS and A502. Note that a number of these red dots have unreasonably large values of C_D since the geometries and design conditions are such that the limits of applicability of A502 are exceeded. These points, approximately a total of 1,000, for which the disagreement between PASS and A502 is large are taken for further evaluation using CE. It must be noted that the reason why we believe that the difference between these two predictions is a good indicator of the error in the A502 prediction is that, albeit simplified, PASS includes a model of compressibility/transonic drag that A502 is unable to account for. For this reason, the discrepancies in the values of C_D are indicative of configurations for which transonic flow conditions may exist and, therefore, indicative of configurations that require a more sophisticated tool (Euler) in order to obtain reasonable accuracy. Figure 6.6 shows in blue the results of the CE analyses for the A502 results labeled in red. Note that no attempt to correct the boom loudness (dBA) is made since the CE results do not have sufficient mesh resolution in the near field to yield accurate boom predictions. This same procedure is repeated once more but increasing the level of fidelity by one step. The points in the CE database that show large differences in comparison with the A502/Panair results ($\epsilon_{PASS-A502} > 30\%$) are re-evaluated using the FE approach. The final result is a set of FE evaluations that are meant to be clustered around the areas where the lower fidelity models cannot accurately predict the flow physics. These results can be seen in Figure 6.7 where the blue and yellow dots represent the CE evaluations. The yellow dots represent the CE candidate designs that exhibit large differences ($> 25\%$) in C_D when compared with the results of A502/Panair. The configurations corresponding to the yellow dots (around 500 in total) are evaluated using the FE procedure and their C_D and dBA values are corrected

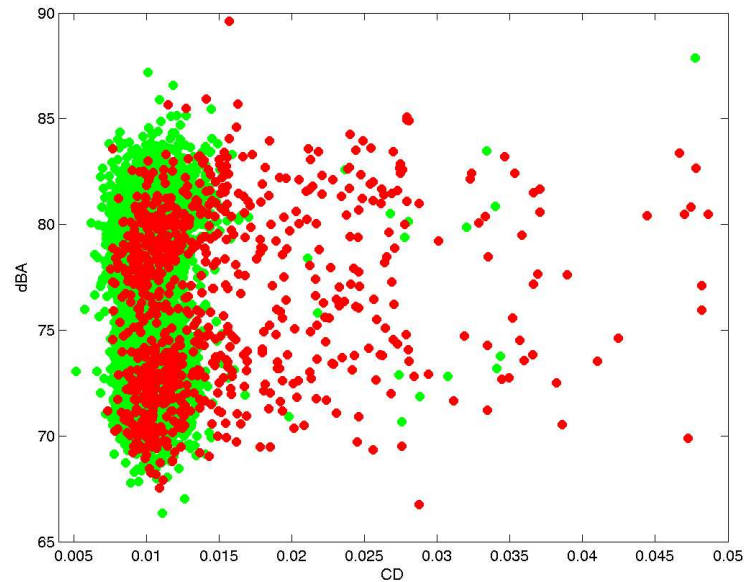


Figure 6.5: Database of A502/Panair results. Green dots: A502-analyzed points. Red dots: A502-analyzed points with large errors.

and represented with the purple dots. Notice that in this last step, the values of the boom loudness for the points representing the FE results have been corrected: the FE results are adaptively refined in the near field so that accurate near-field pressure distributions and ground booms can be obtained.

A quadratic fit (least-squares regression) for C_D is constructed from the 5,000 design points analyzed by A502/Panair. A Kriging fit for the difference in C_D values between the FE and A502 analyses is then added to the quadratic fit. This addition of the quadratic fit of A502 results and the Kriging fit of difference in FE and A502 results becomes the multi-fidelity response surface that replaces the low-fidelity aerodynamic module inside PASS.

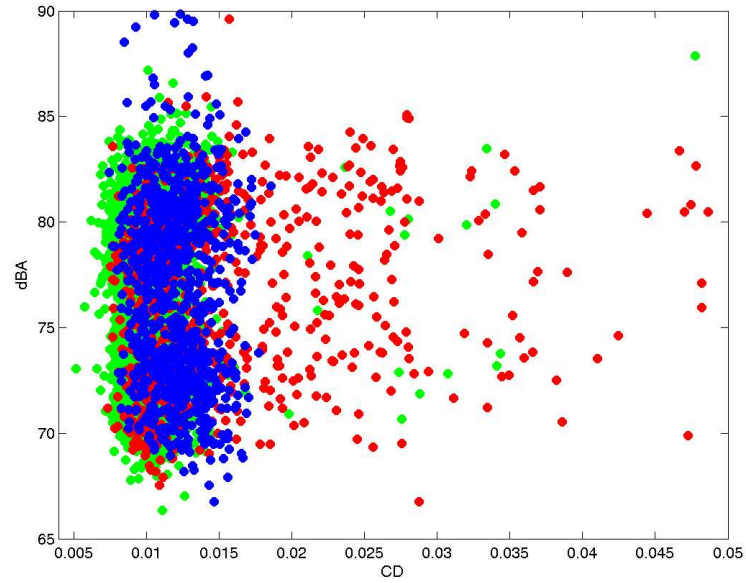


Figure 6.6: A502/Panair and CE results. Green dots: A502-analyzed points. Red dots: A502-analyzed points with large errors. Blue dots: CE-reanalyzed points

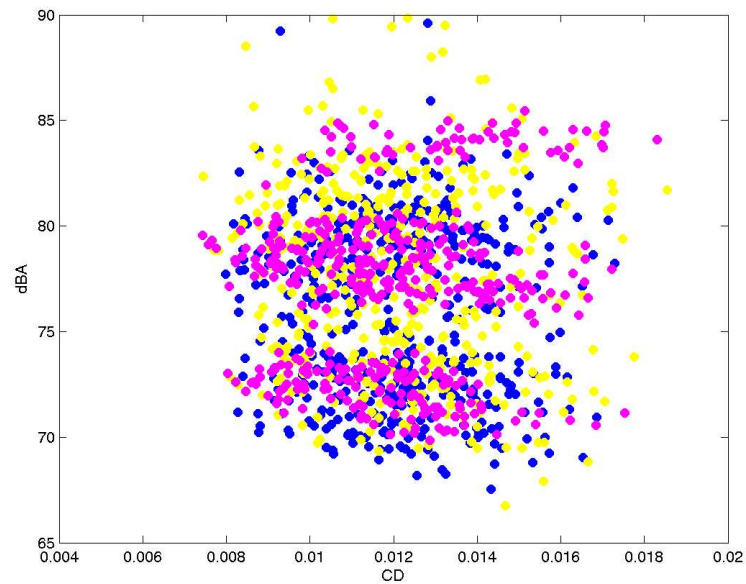


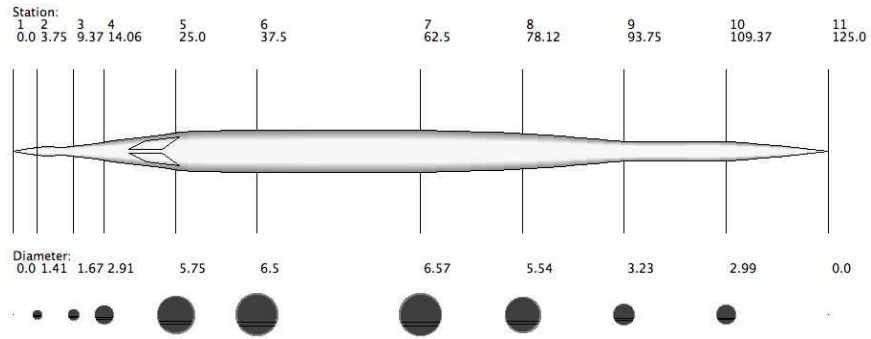
Figure 6.7: CE and FE results: Blue dots: CE-analyzed points. Yellow dots: CE-analyzed points with large errors. Magenta dots: FE-reanalyzed points

6.2.2 Minimum Boom Loudness (dBA) Optimization : Modified PASS Optimization

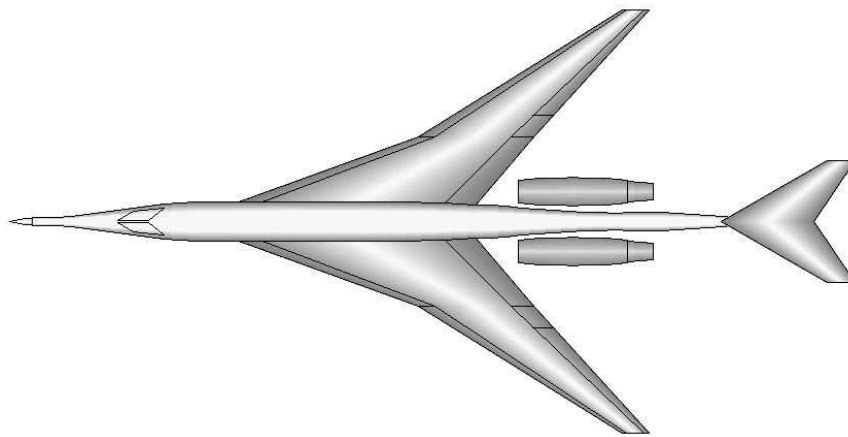
The minimum boom loudness optimization used the fits of sonic boom strength (measured as dBA1 with finite rise time) as the objective function and the multi-fidelity fits for the cruise C_D for the evaluation of the performance of the candidate design during the cruise condition. The mission constraints which were not satisfied by the baseline are fully met by this boom-optimized configuration, and are shown in Table 6.8 and Figure 6.9. Comparison of the near-field pressure signature in Figure 6.10 shows a significant reduction in the shock strength (especially in the rear portion) for the optimized configuration. However the decreased cruise altitude (from 45,315 to 40,854 *ft*) decreases the effectiveness of this near-field pressure reduction as shown in Figure 6.10 (b). This fact indeed indicates the difficulty of this type of multi-disciplinary problem. Nevertheless, the reduction in the ground boom is still noticeable, about 3.47 dBA1 from 81.12 in the baseline to 77.65 dBA1 (78.87 dBA1 from the RS prediction). It is noted that an increase in MTOGW appears to be inevitable in order to increase the range from 3,381 n.mi to 4,000 n.mi.. If we were to introduce more design variables and allow for wing section changes as in Design II, this range constraint can be shown to be satisfied with much less MTOGW and this will be explained in the section discussing Design II.

Variation on Result of Boom-Constrained Optimization

Although a seemingly viable design was found, as shown in the summary Table 6.8, an examination by experienced designer of the planform view in Figure 6.8 indicates that the optimizer is exploiting a weakness in the wing weight routines' ability to estimate the increase in weight due to sweepback. Accordingly the optimizer excessively increases the sweepback in an effort to drive the objective value down. A minor modification of this configuration is generated in the next section in order to create what is deemed to be a more feasible wing planform. It is worth calling attention to the interesting fuselage shaping that has been converged upon. A plot of the iteration history for this case is shown in the Figure 6.11.



(a) Fuselage layout and stations



(b) Top view of configuration

Figure 6.8: Summary of boom optimized configuration (Design I).

Performance	
Range	4,000 n.mi.
BFL	6,500 ft
MTOGW	97,130 lbs
Ground signature (dBA)	77.65 (78.87 from RS)
Wing and Tail Geometry	
Wing reference area	1,155 ft^2
Wing aspect ratio	4.2
Wing quarter-chord sweep	55°
Leading edge extension	0.55
Trailing edge extension	0.026
Wing root leading edge	0.23
Root section t/c	3.0%
Break section t/c	2.56%
Tip section t/c	2.0%

Table 6.8: Results of PASS + response surface optimization for boom minimization.

Minor reductions in reference area (from 1,155 ft^2 to 1,100 ft^2), aspect ratio (from 4.2 to 3.7) and sweep (55 degrees to 54 degrees) were manually applied to the above design to return the wing planform to a more reasonable shape. The resulting configuration suffered a only modest decrease in the ground boom noise level (by 0.82 dBA1, from 81.12 to 80.3 dBA1), while still managing to meet all other constraints, as can be seen in Table 6.9 and Figure 6.12.

6.2.3 Minimum TOGW Optimization: Modified PASS Optimization

An optimization was also run with TOGW as an objective function and with sonic boom removed entirely from consideration in the design problem. Given the results presented in Table 6.10 and Figure 6.13, it can be surmised that the outlandish low-boom configuration in Section 6.2.2 was largely due to the boom requirement, since this pure-performance optimization results in a decidedly more believable design. The resulting design, however has an increased boom loudness which is slightly higher than the baseline, by 2.58 dBA1 from 81.12 in baseline to 83.7 dBA (84.9 dBA1 from

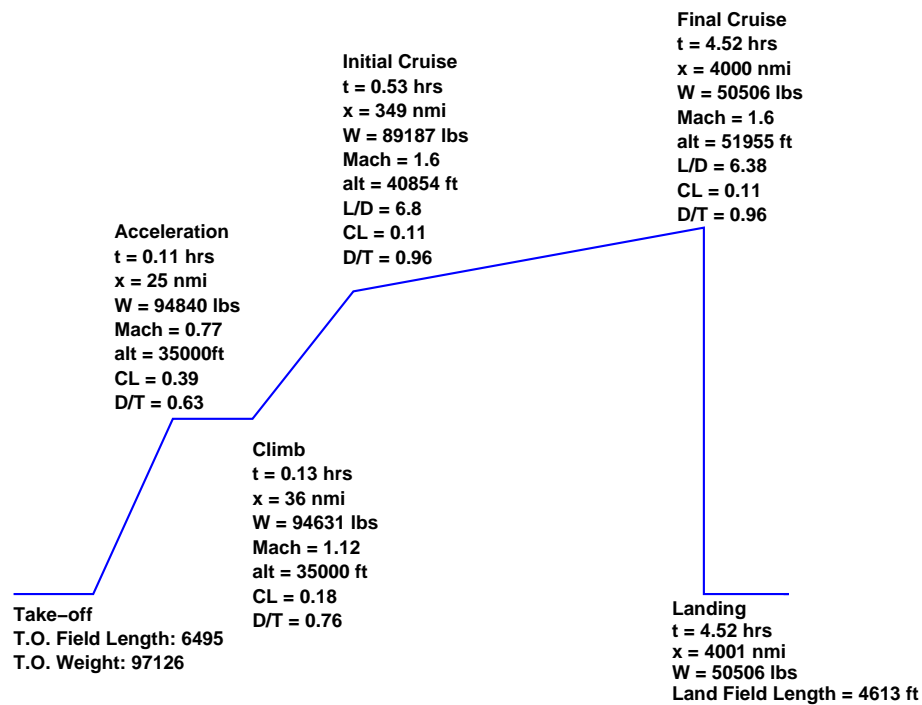
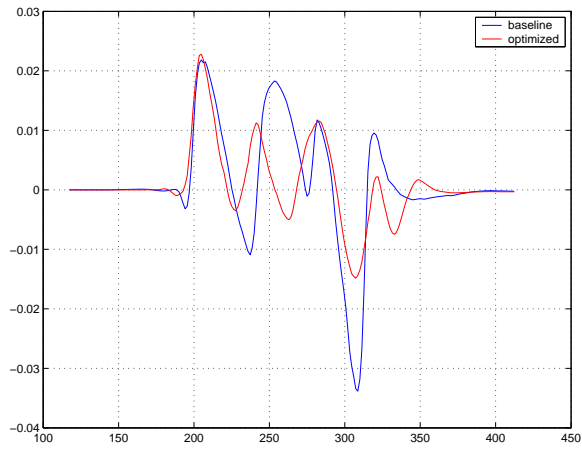


Figure 6.9: Mission profile (analyzed by standard PASS+RS) of boom optimized configuration (Design I)

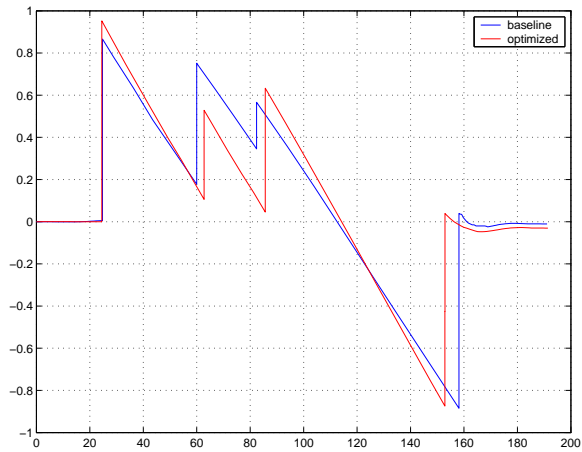
RS prediction) in the optimized configuration. Considering that the minimum boom design had achieved a 3.5 dBA reduction, this improvement in performance comes at a substantial cost. The MTOGW was reduced from the boom-optimized configuration, but it is still higher than the PASS baseline so that the range constraint can be met.

6.2.4 High-Fidelity Validation of Optimization Results

In this section we present the results of the validation of the predicted boom and aerodynamic performance (C_D) for the designs carried out using the PASS+RS approach. We present validations for the boom-optimized configuration and for the TOGW optimization only. These results serve two main purposes. Firstly, they assess, indirectly, the accuracy of the response surface fits, at least in the areas where the optima are found. Secondly, they provide the necessary confidence in the outcome of the designs from the PASS+RS design methodology.



(a) Near-field pressure distribution



(b) Ground boom signature

Figure 6.10: Euler comparison for optimized and baseline designs.

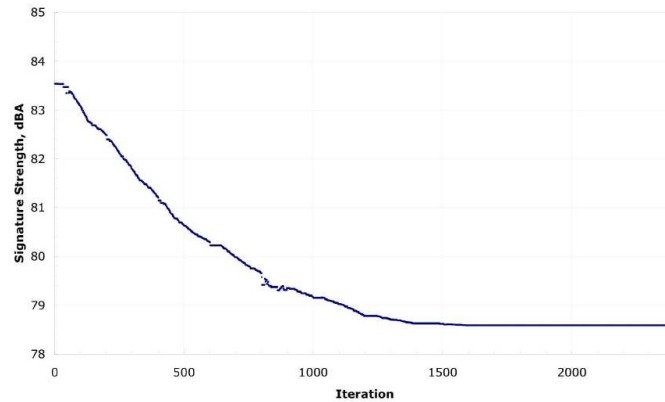


Figure 6.11: Convergence history of boom constraint function.

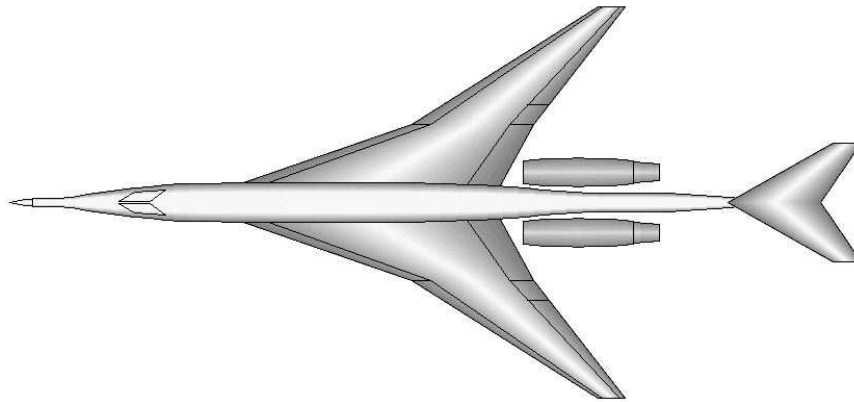
Performance

Range	4,021 n.mi.
BFL	6,255 ft
MTOGW	95,000 lbs
Ground signature (dBA)	80.3

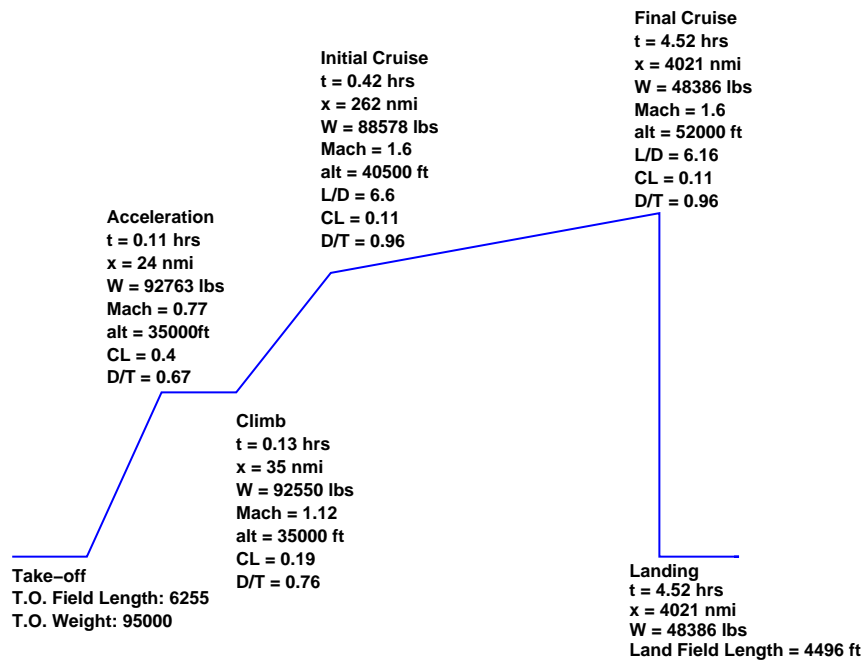
Wing and Tail Geometry

Wing reference area	1,100 ft^2
Wing aspect ratio	3.7
Wing quarter-chord sweep	54°
Wing root leading edge	0.23

Table 6.9: Results of PASS + response surface optimization for boom-constrained optimization with small manual modifications.

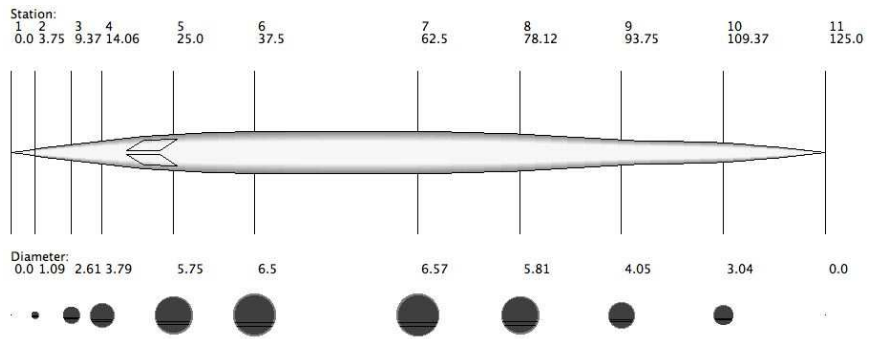


(a) Top view of configuration

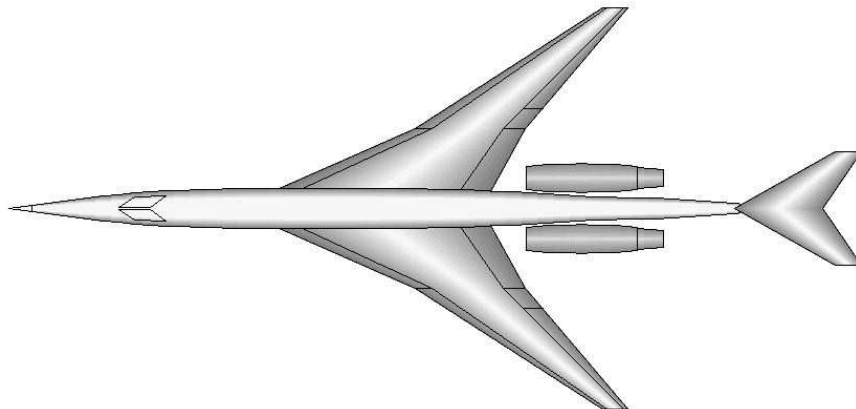


(b) Mission profile (analyzed by PASS + RS)

Figure 6.12: Summary of boom optimized configuration with small manual modifications (Design I).



(a) Fuselage layout and stations



(b) Top view of configuration

Figure 6.13: Summary of TOGW optimized configuration (Design I).

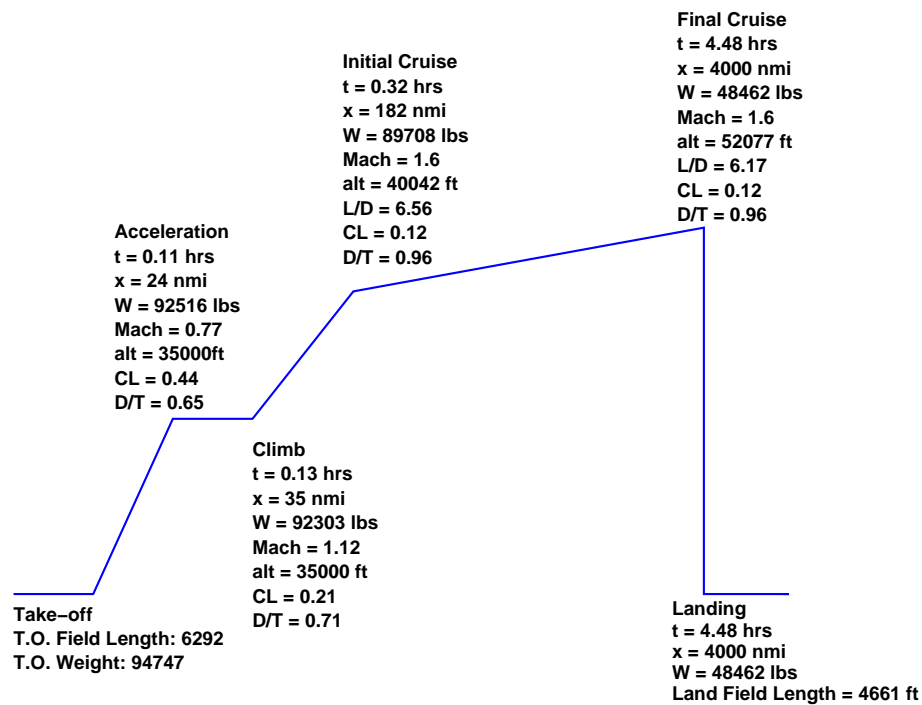


Figure 6.14: Mission profile (analyzed by standard PASS+RS) of TOGW optimized configuration (Design I)

Table 6.11 shows the results of this validation study. As can be seen the errors in the prediction of the inviscid C_D of the aircraft are rather small: for the boom-optimized design, the response surface fit predicted a $C_D = 0.00911$ (S_{ref} for boom-optimized design is $1,156ft^2$, and for baseline $1,025ft^2$. Design C_L at initial cruise for boom-optimized design is 0.11583 and design C_L for baseline is 0.1446), while the actual Euler re-analysis produced $C_D = 0.00949$. The same is true, or even better of the TOGW-optimized result: the response surface fit had predicted a $C_D = 0.01154$ (S_{ref} for boom-optimized design is $1,000ft^2$, and for baseline $1,025ft^2$. Design C_L at initial cruise for TOGW-optimized design is 0.128 and for baseline 0.1446), while the actual Euler re-analysis comes in very close at $C_D = 0.01174$, a very small error indeed. The comparisons for the predicted boom levels show a similar trend. For the boom-optimized configuration, the response surface fit had predicted a value of $dBA = 78.87$, while the Euler re-analysis yielded $dBA = 77.65$. In other words, the response surface had over-predicted the noise level of the configuration by almost 1

Performance	
Range	4,000 n.mi.
BFL	6,300 ft
MTOGW	94,747 lbs
Ground signature (dBA)	83.7 (84.9 from RS)

Wing and Tail Geometry	
Wing reference area	1,000 ft^2
Wing aspect ratio	4.2
Wing quarter-chord sweep	54.1°
Leading edge extension	0.34
Trailing edge extension	0.14
Wing root leading edge	0.29
Root section t/c	2.6%
Break section t/c	3.06%
Tip section t/c	2.55%

Table 6.10: Results of PASS + response surface optimization for TOGW optimization.

	$C_{D_{RS}}$	$C_{D_{Euler}}$	dBA_{RS}	dBA_{Euler}	C_D Rel. Error	dBA Rel. Error
Min. Boom Design	0.00911	0.00949	78.87	77.65	4%	1.57 %
Min. TOGW Design	0.01154	0.01174	84.9	83.7	1.7 %	1.43%

Table 6.11: Results of validation of minimum boom and minimum TOGW designs.

dBA. For the TOGW-optimized configuration, the response surface fit predicted a dBA = 84.9, while the actual Euler analysis achieved dBA = 83.7.

6.3 Design II: Two-Level Optimization of Aerodynamic Performance

In this section we describe our approach to the two-level design of a supersonic business jet configuration where we combine a conceptual, SIMPLEX-based, optimization tool having a hierarchy of flow solvers of increasing fidelity (including simplified aerodynamic models, a linearized panel method and both structured and unstructured Euler solvers) and advanced adjoint-based Sequential Quadratic Programming (SQP) optimization approaches.

An approach that has been often followed to introduce higher-fidelity analyses into these conceptual design tools is the use of pre-generated response surfaces that represent, in an accurate and inexpensive way, some key disciplines in the design: the computational cost is paid upfront when the response surfaces are generated by repeated evaluation of the MDAs. This type of highly-tuned conceptual design tools often employs direct search method because of the low computational cost per function evaluation. Unfortunately, the use of higher-fidelity models often requires higher-fidelity discretization with much large numbers of design variables (this is indeed the case for aerodynamic shape optimization [94, 95]), making the use of traditional response surface formulations impossible within the context of *conceptual* design and using large numbers of design variables.

On the other hand, much progress has been achieved with some specific high-fidelity design tools. This is true in both the structural design and aerodynamic shape optimization communities [108, 105, 94, 140]. In these two areas both separately and in combination [107, 138, 137, 139] novel methods such as the adjoint and direct methods have been used to carry out designs with high-fidelity and large numbers of design variables. Efforts to couple these advanced design methods to the large number of disciplines that are considered in traditional *conceptual* design are only at their beginning stages and the adjoint method for aerodynamic shape optimization, for example, has not been yet extended to treat the highly constrained design spaces present in supersonic vehicle design.

As one of these efforts, we are seeking to combine the advantages of both non-gradient- and gradient-based design methods. A direct method is combined with multi-fidelity response surfaces to handle very large variations of the design variables. Since we are trying to limit the computational expense required to construct these multi-fidelity response surface approximations, we are willing to work with approximations that may have errors around 5% in some areas of the design space where the sample points used for the response surface construction have not been sufficiently clustered. For this reason, the second component of our two-level optimization approach is to perform adjoint-based aerodynamic shape optimizations of the resulting multi-disciplinary designs to recover the performance that may have been lost due

to inaccuracies in the response surfaces and to ensure that the performance of the resulting design is that predicted by the high-fidelity tools. In principle, a realistic design procedure would iterate between these two optimization levels; in this thesis we have carried out a single iteration of the procedure for demonstration purposes. The resulting design, however, meets all of the design constraints and criteria at the end of this first design iteration.

First, multi-fidelity response surfaces are constructed using both A502/Panair and the AirplanePlus Euler solver in a manner that is similar to that described in Design I. The SIMPLEX method is used for the first global optimization level, together with these response surfaces, to find the expected locations of the optima in such large design spaces. This procedure is performed entirely inside PASS and all the necessary constraints are imposed. In other words, the first step of the design optimization calculations in Design II are very similar to the actual optimizations carried out in Design I. High-fidelity validations of the corresponding optimized configuration (using both structured and unstructured Euler solvers) are also shown and compared to each other in Chapter 4.

The adjoint wing redesign follows so that maximum performance (minimum drag) at the cruise condition can be recovered. The wing planform and fuselage shape resulting from the first design step remain fixed during this adjoint shape optimization. A larger number of design variables are introduced mainly in the wing sections. Since the changes occur only in the wing sections (twist and camber, no thickness changes) it is assumed that the resulting configuration will be close to still meeting all of the mission requirements imposed by PASS at the first global optimization level. Of course this may not be exactly true (due to variations in chordwise and spanwise loading and changes in pitching moment), but additional iterations of the design procedure are, in principle, able to correct these inconsistencies.

6.3.1 Modifications to Baseline Configuration

In Design I, a low-boom optimized configuration with high aerodynamic performance was found. However an increase in MTOGW from the standard-PASS results appeared to be necessary to fully recover the range requirement. A resulting flat wing (no twist or camber) prevents the baseline from obtaining its maximum aerodynamic performance. The baseline in Section 6.1 had an RAE supercritical airfoil in the wing inboard section and a biconvex airfoil with a sharp leading edge in the wing outboard sections and tails. However, since the designs appear to result in subsonic leading edges, subsonic airfoils are a better choice.

Therefore minor changes were made to the original baseline used in Design I. We replaced the wing sections with the NACA65 series airfoils with a rounded leading edge, and decreased the thickness of the tails from 5% to 3%. Due to these changes, the inviscid drag was reduced by almost 13 counts from 0.0117 to 0.0103451. To investigate the effect of the wing twist on aerodynamic performance (remember that the wing twist was not directly manipulated by PASS), a total of five test cases were calculated. For each of these cases, the wing was given a washout varying from -1° to -5° in increments of 1° , and linear interpolation of the twist through the span was assumed. The corresponding inviscid drag coefficients are shown in Figure 6.15. Although the linear twist distribution may not be ideal, we can infer from this simple experiment that there is a certain twist angle distribution which leads to a load distribution that maximizes aerodynamic performance. If we choose the wing with a washout of -4° , an additional reduction of 6 counts in inviscid drag was obtained, and the inviscid C_D is reduced to 0.00973452 (S_{ref} is fixed at the same value, 1,025ft). This configuration was chosen as the baseline for Design II. The corresponding mission parameters are shown in Table 6.12. Even by including the twist changes (that PASS did not consider directly) the mission requirements are not satisfied with this modified baseline design. Although some improvements have been achieved from the original baseline, additional design work is needed to fully meet the mission requirements.

As mentioned before, one of the main purposes in this thesis work is to see how

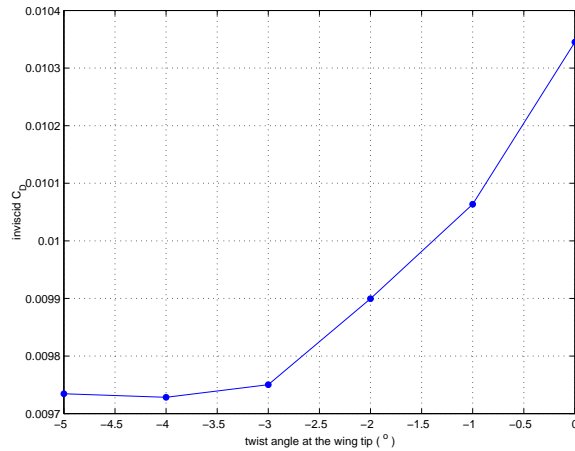


Figure 6.15: Inviscid drag coefficients at various wing tip twist angles.

Performance	baseline in Design I	baseline in Design II
Range	3381 n.mi.	3624 n.mi.
BFL	5434 ft	5434 ft
L/D at initial cruise	6.30	6.69
L/D at final cruise	5.95	6.49
Climb gradient at initial cruise	-0.02436	-0.012749
Climb gradient at final cruise	-0.0254	-0.00867

Table 6.12: Comparison of mission profile for modified baseline (analyzed by PASS + Euler)

closely our multi-fidelity optimization work can get to the standard PASS optimization results. These results are based on best-case scenario aerodynamic assumptions and therefore can be considered to be representative of the highest performance achievable. In Design II, the ground boom loudness was removed completely as a consideration so that direct comparisons with the results of PASS can be made. The improved baseline configuration (described earlier) with changes to the airfoil sections and with a wing washout of -4° is employed as the starting point for Design II. The corresponding inviscid drag coefficient was for this configuration at the beginning of the cruise condition was found to be 0.00973452.

Additional design variables for the wing sections are introduced. These consists of the twist angles at three wing sections (root, break and tip) and the value of the

maximum camber and its location at two wing sections (root and break) which are included as shown in Table 6.6.

6.3.2 Multi-Fidelity Response Surface

The construction procedure of the multi-fidelity response surface is the same as was used in the Design I, although the hierarchy of analysis tools is slightly different. A hierarchy of three different aerodynamic analysis modules was used:

1. PASS
2. A502/Panair
3. Fine Euler (FE) simulation used only for inviscid drag calculation.

The grid size in the FE calculation in this Design II case (~ 1.5 million nodes) is smaller than in the FE in Design I ($3 \sim 5$ million nodes). This is because the objective of Design II is the minimization of MTOW without consideration of sonic boom. High mesh density is required only on the surface of the aircraft and in the neighborhood of the surface of the configuration, but not in the near-field below the aircraft as was the case in Design I. The computation times for a flow solution of these FE calculations is less than 7 min (on a 16 processor computer), although the computation time for geometry creation and mesh generation remains the same.

The response surface creation procedure is summarized again below:

1. Initial design points ($> 8,000$) are sampled by LHS, and PASS analyzes the mission and the aerodynamic properties. A pre-specified mission violation threshold selects feasible and mildly infeasible candidates for the A502/Panair analysis.
2. A502/Panair calculates the aerodynamic performance for about 2,500 design points filtered from the PASS mission analyses in 1..
3. The error in C_D is compared with the threshold value, $\epsilon_{PASS-A502}$ (45%). The design points for which the error is larger than the threshold are selected (~ 250 points) and recalculated by the FE calculation.

4. A quadratic fit (least-squares regression) for C_D is constructed from the 2,500 points analyzed by A502/Panair. A Kriging fit for the difference in C_D values between the FE and A502 analyses the is added to the quadratic fit.

Figures 6.16 and 6.17 show a graphical view of the procedure followed in the multi-fidelity response surface construction. C_D values are plotted at various design C_L values. The initial 2,500 design points selected by the mission violation criteria are plotted in green dots in Figure 6.16. The design points which have a difference in C_D between A502 and PASS, $\epsilon_{PASS-A502}$, larger than the 45% are highlighted in red. Note that some of those points have unreasonably high C_D values indicating that A502 cannot provide an accurate analysis for some configurations. Those 250 design points are recalculated by FE and the corrected values are plotted in blue in Figure 6.17.

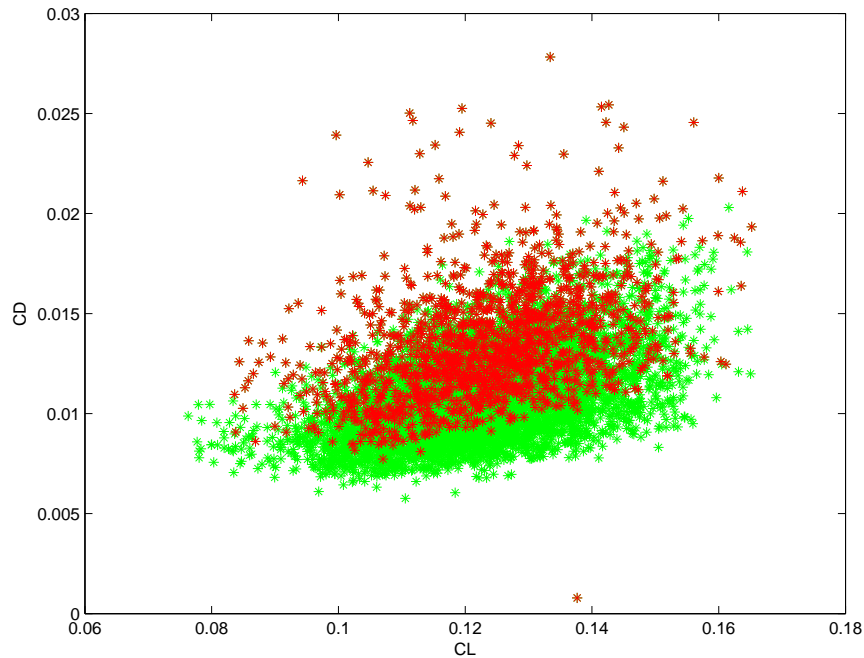


Figure 6.16: Database of PASS (green) and A502/Panair (red) results.

The constructed multi-fidelity response fit can replace the corresponding low-fidelity modules in PASS, which makes for a remarkably simple integration problem.

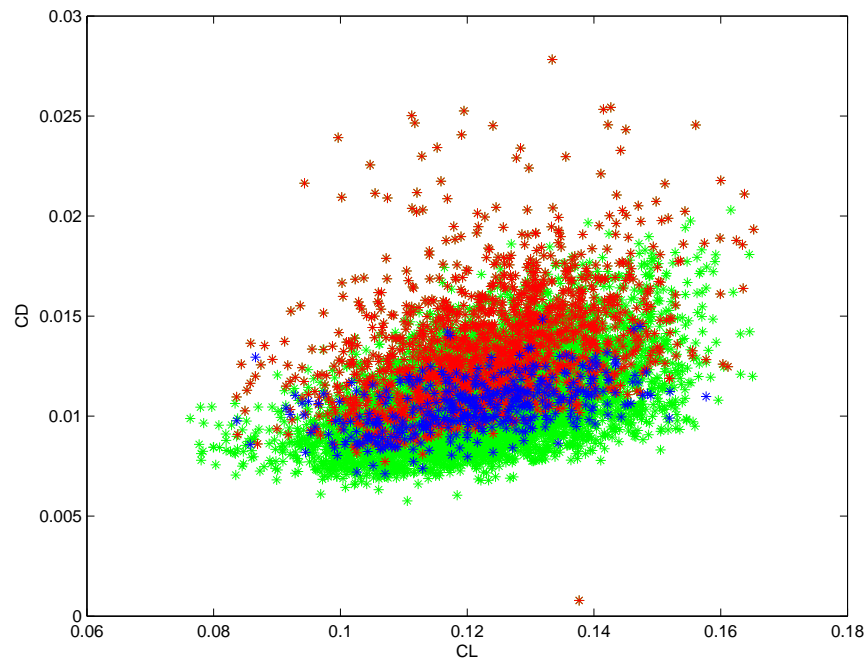


Figure 6.17: Database of PASS (green), A502/Panair (red) and FE (blue) results.

PASS can then be used to generate optimized results and the outcome of the optimization can be analyzed using high-fidelity tools to ensure that the response surface fits provide accurate representations of the true high-fidelity responses. The validity of these fits will be assessed by direct analysis of the resulting optimized designs using two different Euler solvers.

6.3.3 Minimum MTOGW Optimization: Gradient-Free Global Optimization Using Modified PASS

In this section we present the results of the optimization that used the version of PASS that had been enhanced with the response surface fits created with our multi-fidelity approach. The focus was on minimizing the MTOW of the aircraft while meeting all of the mission requirements.

Views of the fuselage layout, a top view of the optimized configuration, and the resulting mission profile with key values are shown in Figure 6.18 and 6.19. Figure 6.20

Performance	
Range	4,000 n.mi.
BFL	6,381 ft
MTOGW	87,547 lbs

Wing and Tail Geometry	
Wing reference area	1,082.82 ft^2
Wing aspect ratio	3.12
Wing quarter-chord sweep	58.85°
Leading edge extension	0.617
Trailing edge extension	0.00846
Wing root leading edge	0.20
Root section t/c	2.3%
Break section t/c	2.5%
Tip section t/c	2.55%

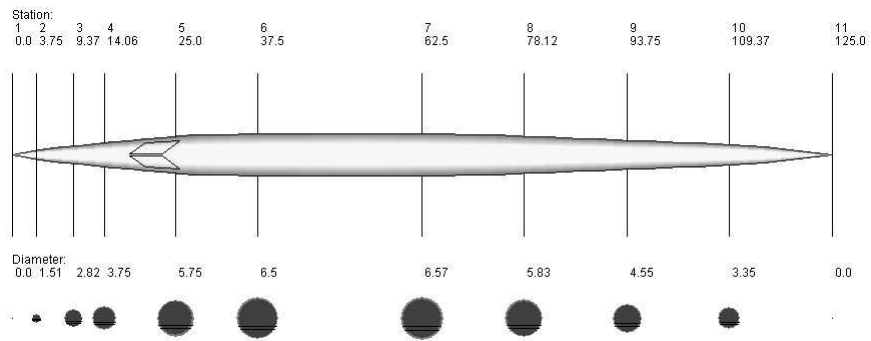
Table 6.13: Results of PASS + response surface optimization for boom minimization.

shows the side-by-side comparison of the baseline and optimized configurations. Performance and geometric details are shown in Table 6.13. The increase of the wing inboard sweep and the decrease of the wing AR are noticeable in the wing planform changes. From the front view in Figures 6.20 (b) and (d), we can see that the flat wing of the baseline configuration has received both camber and twist. Minor changes in several fuselage sections have also occurred.

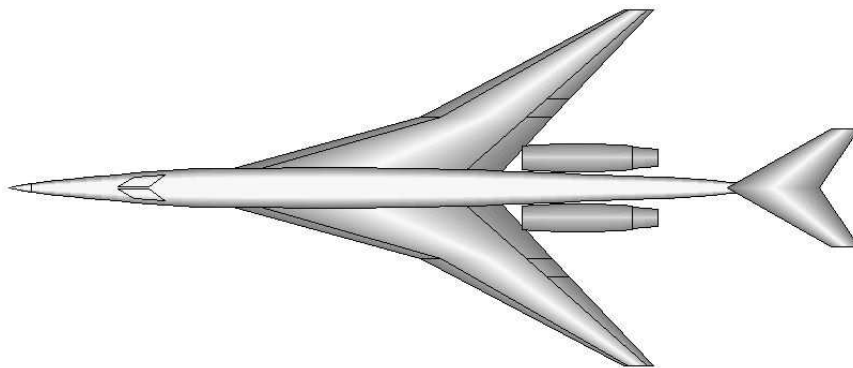
It should be noted that the reduction of MTOGW is very significant when compared to Design I with a MTOGW of 87,574 lbs. At a design C_L of 0.1367, the inviscid C_D was as small as 0.0085 (The baseline had C_D , 0.0119 at design $C_L=0.1446$. S_{ref} for optimized design is 1,000 ft^2 , and S_{ref} for baseline is 1,025 ft^2). The standard PASS version predicts C_D , 0.0077 at this design C_L . Additional drag reductions will be shown in the second step of this design procedure by using an adjoint wing redesign method.

6.3.4 High-Fidelity Validation of Optimization Results

There are several points of interest that must be noted. The response surface fit predicts a lower C_D and a higher C_L (improving L/D significantly) when compared with the direct Euler analysis. As a result of the quality of the response surfaces our



(a) Fuselage layout and stations



(b) Top view of configuration

Figure 6.18: Summary of optimized configuration (Design II).

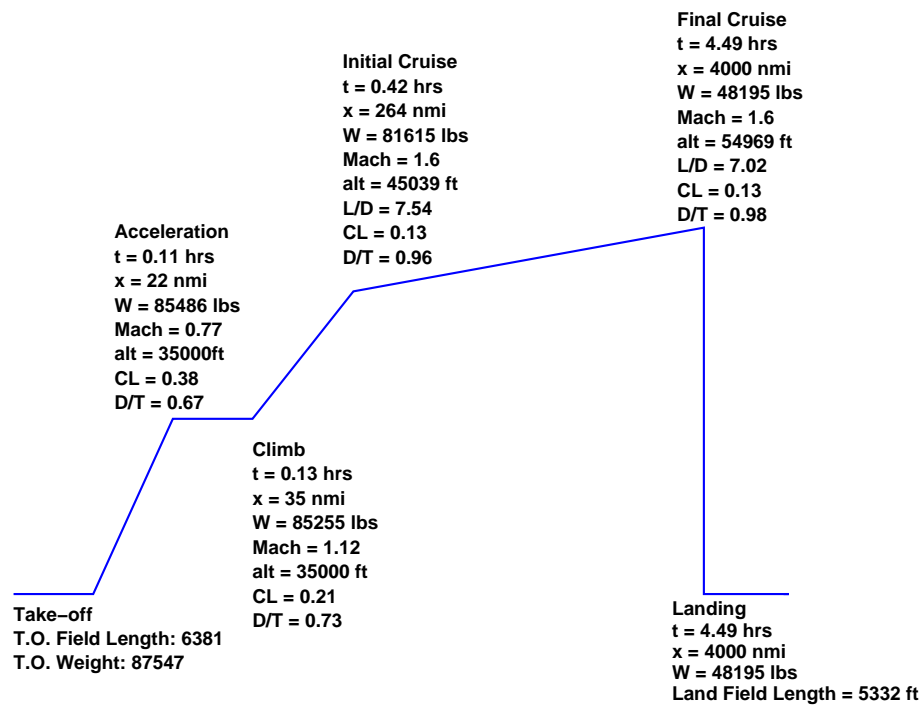
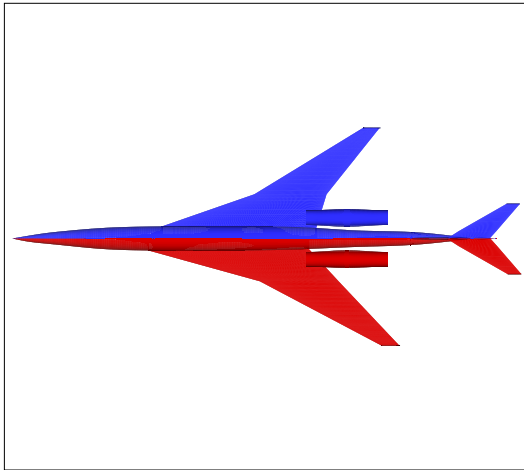


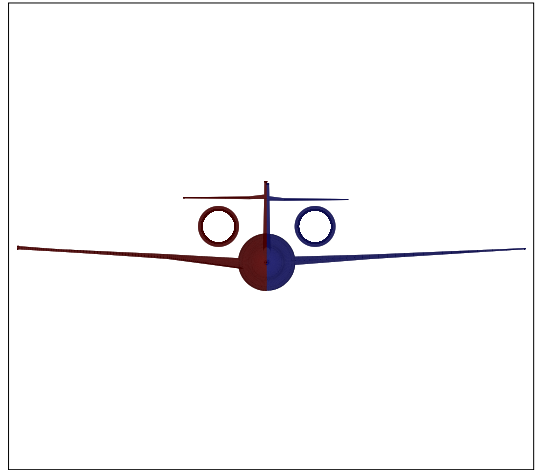
Figure 6.19: Mission profile (analyzed by standard PASS+RS) of optimized configuration (Design II)

optimizations believe that they have achieved a higher performance aircraft than they really have. In fact, PASS+RS predicts an inviscid cruise C_D of 0.0074 at a design C_L of 0.1367. With the same flight conditions and geometry standard PASS predicts a $C_D = 0.0077$, meaning that the value from the response surface for C_D was slightly underpredicted (C_D for baseline was 0.0119 at design C_L 0.1446 with S_{ref} 1,025ft, while optimized design has design C_L 0.128 and S_{ref} 1,000 ft). Euler validation of this configuration results in an inviscid C_D that is larger by 13% with a value of 0.0085.

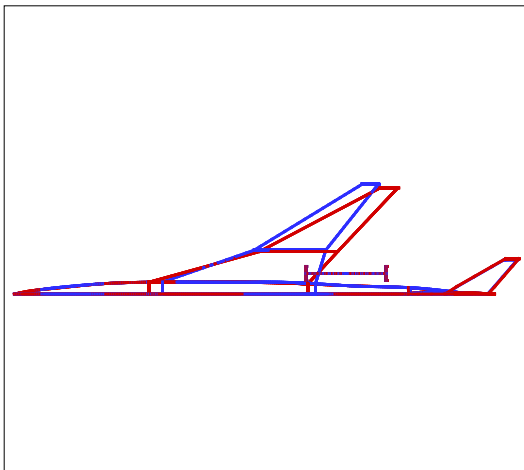
After careful investigation, the reason for these differences becomes obvious: the Euler analyses used to create the C_D response surfaces are clustered around design C_L 's of 0.12 to 0.13. In the meanwhile, the optimizer has determined that a larger C_L would be beneficial to the design (in the neighborhood of 0.1367). For this reason, the amount of high-fidelity data points around the final design region is small and the quality of the fit is reduced. This seems to indicate that additional Euler evaluations



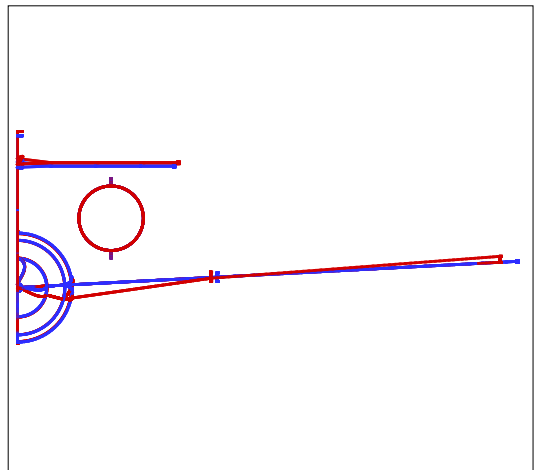
(a) Top view of baseline and optimized configurations



(b) Front view of baseline and optimized configurations



(c) Comparison of wing planform



(d) Comparison of front view

Figure 6.20: Comparison of shapes of baseline and optimized configuration (blue:baseline, red:optimized).

in the neighborhood of $C_L = 0.1367$ would be needed to improve the agreement between the predicted and achieved designs.

After realizing that the richness of our fits was poor around the 0.1367 value of lift coefficient, other optimizations were run that were forced to fly at lower levels of C_L (around 0.12). Surprisingly, the design parameters for those designs were very similar to the previous one already presented with $C_L = 0.1367$. The corresponding Euler validation shows similar differences from the response surface results, and for that reason we have omitted those results here.

In comparison with previous work [91] it is clear that the number of high-fidelity function evaluations required for a 25-dimensional design space is more in the neighborhood of 500-1000 than in the 200 range that we have used here.

6.3.5 Minimum Drag Optimization: Adjoint Local Optimization

Once the simplex method has converged to an optimum (local or global) we may limit ourselves to smaller changes in the configuration. These changes are more likely to result on well-behaved design spaces that can be tackled with an adjoint procedure and a gradient-based optimization algorithm. In this second level of our optimizations we limit ourselves to modifications in the twist and camber of the wing, while maintaining the same wing planform, fuselage and relative positioning of the nacelles and empennage. The resulting optimized shape contains more details in the description of the wing geometry.

Two different tools are available for this portion of the overall optimization:

1. *SYN87-SB*. A single-block, wing-body Euler adjoint optimization code that uses the NPSOL SQP algorithm for the optimization with or without constraints. SYN87-SB allows for arbitrary changes to the shape of the fuselage and wing and is able to enforce thickness, curvature, and fuel volume constraints.
2. *SYN107-MB*. A multi-block, complete configuration, RANS adjoint optimization code that also uses the NPSOL SQP algorithm for optimization and that

allows similar geometry controls, cost functions, and constraints as SYN87-SB, but that can be made to treat arbitrarily complex geometries such as the complete aircraft configurations that are the subject of this work.

Because of time limitations, this second level of adjoint-based optimization was carried out using the SYN87-SB code only, although the flow solver portion of SYN107-MB was used to carry out validation runs using a 5.9 million node multiblock mesh that was constructed for the PASS/response surface optimized configuration. The second optimization involves the result of wing-body adjoint-based optimizations where the only design variables in the problem correspond to a detailed parameterization of the twist and camber distributions on the wing. Everything else remains unchanged from the values of the optimized configuration. For this purpose a drag minimization calculation at a $C_L = 0.1367$ was carried out. The twist and camber distributions of the wing were parameterized at 7 defining stations with 18 design variables each (leading and trailing edge droop, twist and 15 camber Hicks-Henne bumps) for a total of 126 design variables, which is a comparably large number when compared with the 9 design variables for the wing planform and sections in the first SIMPLEX optimization level. The optimization was allowed to run for 50 design iterations, at which point it was stopped (although full convergence had not been reached, the results were making very small drag improvements, of the order of a tenth of a count of drag). At the design C_L the computed value of the drag for the baseline wing-body configuration (using a block-structured mesh with $257 \times 64 \times 49$ nodes) was 72.02 counts. In 50 design iterations and through twist and camber changes, the drag of the wing-body configuration decreased by almost 5.5 counts. Although this reduction in C_D was achieved for the wing-body geometry, if we assume the same or better improvement for the full configuration with tails and nacelles we can expect the C_D values to be as low as those predicted by PASS. At a design $C_L = 0.1367$ the Euler analysis for the optimized configuration from the global PASS optimization was $C_D = 0.0085$. If we apply a similar drag count reduction of 5.5 counts from the wing-body configuration to the full configuration, we can assume that $C_D = 0.0079$ which is very close to what the standard version of PASS predicted, $C_D = 0.0077$. This implies the following very important fact: additional design work with specific

Objectives	Baseline	Optimized
C_L	0.1447	0.13671
S_{ref}	1,025 <i>ft</i>	1,000 <i>ft</i>
inviscid C_D	0.0099735	0.0079
inviscid L/D	14.51	17.31
MTOW (lbs)	85,809	87,547

Table 6.14: Comparison of performance between baseline and optimized configuration

design tools can recover values close to the maximum theoretical aerodynamic performance. This conclusion validates the use of tools such as PASS which include realistic upper bounds in performance. It also highlights the need for a complete set of design tools that can ultimately create the geometry that can recover these upper bounds in performance.

Chapter 7

Conclusions and Future Work

In this thesis, a number of design methods for the optimization of low-boom supersonic jets were investigated. Major issues regarding the optimization problem (including single- vs. multi-disciplinary aspects, high- and multi-fidelity analyses, and global vs. local searches) have been explored in the context of configuration and mission design.

An accurate boom prediction tool, BOOM-UA, was developed to automate the entire analysis procedure (from parametric CAD representation to aerodynamic performance and ground boom signatures and loudness). Detailed validation was carried out using available wind-tunnel experimental data. In addition, careful verification studies involving the required mesh resolution for this type of sonic boom calculations were carried out to determine the level of resolution needed to guarantee accurate design results. Multi-disciplinary aspects were included by considering the full length of the aircraft mission from take-off to landing. Mission constraints including T/O and landing field length, cruise range, climb gradient, stability & control and propulsion were imposed on the optimization problem. These attempts rendered the optimization process more complicated and computationally expensive. In addition, the ill-behaved characteristics of the boom design space made the use of efficient gradient-based optimization impossible, and instead a global search method was introduced. To alleviate the computational burden, a surrogate model is connected to global optimizer, which is built from a set of training data analyzed by various fidelity analysis tools. A hierarchy of analysis tools of different fidelities was employed in such

a way that the high-fidelity analyses were applied only when lower-fidelity analyses showed unacceptable accuracy. Kriging models and least-squares regression models were used to build multi-fidelity response surfaces.

A hybrid approach to combine global and local search methods was investigated by employing a two-level optimization procedure, and a mesh adaptive direct search method was also tested (although not discussed in this document). An adjoint-based NPSOL optimizer was applied in the neighborhood of the optimum that the first-level global optimization identified. Additional improvements were achieved compared to the single-level global optimization approach. The idea of solution-adaptive meshing of the design space was also employed but not discussed in this thesis.

These results show that our hybrid approach for surrogate model construction and optimization is quite useful in optimization problems involving supersonic jets.

7.1 Future Work

Several questions have been raised during this investigation that can help improve our approach and the quality of the results. The following areas are left for future work:

1. The introduction of a larger number of design variables is necessary to allow for geometric changes in the rear part of the configuration: for a reduction of the rear peak of the ground signature more geometric control is needed. In addition, careful choice of the parametrization control for these additional design variables was suggested by the results presented in Chapter 6. At the optima, the values of several design variables ended close to the upper or lower bounds used in the response surface construction. This indicates that during the response surface construction the range of variation for these variables should be adjusted/increased.
2. Details validations of the approximation models in our optimizations show, in general, good agreement with the high-fidelity analyses. However, more accurate models will contribute to making entire design procedure more robust and

effective. The development of global approximation models which are able to fit the noisy boom design space remains an important task. This will inevitably include automates techniques for the *refinement* of the baseline response surfaces.

3. Higher mesh resolution may be required for shaped boom design problems.
4. As the number of design variables increase, the computation time for GAs increase. Parallel GAs are available for computational speedups.
5. Some of the optimized wing shapes appear to have structural flutter problems. The introduction of more robust structural constraints in PASS would be desirable.

Bibliography

- [1] “Civil Aircraft Sonic Boom,” Aeronautics and Space, Code of Federal Regulations, Title 14, Part 91, Federal Aviation Adm., Jan. 1, 1987, pp. 169-170.
- [2] Stephen R. Norris, Edward A. Haering, Jr., and James E. Murray, “Ground-Based Sensors for the SR-71 Sonic Boom Propagation Experiment,” *High Speed Research Program Sonic Boom Workshop, NASA Langley Research Center, Hampton, VA, September, 1995*
- [3] *Leatherwood JD, Sullivan BM, Shepherd KP, McCurdy DA and Brown SA, “Summary of recent NASA studies of human response to sonic booms,” J Acoust Soc Am, 2002 Jan; 111(1 Pt 2):586-98.*
- [4] Fields, James M. “Reactions of Residents to Long-Term Sonic Boom Noise Environments,” *NASA/CR-97-201704, Wyle Laboratories, June 1997*
- [5] *Hubbard, H.H., Shepherd, K.P.A “A method for predicting community annoyance due to exposure to sonic booms,” 124th Meeting Acoustical Society of America, New Orleans, LA (Oct.31-Nov.,1992)*
- [6] *R.T. Whitcomb, and T.L. Fischetti, “Development of a Supersonic Area Rule and an Application to the Design of a Wing-Body Combination Having High Lift-to-Drag Ratios,” NASA RM, L53H31a, 1953.*
- [7] G.B. Whitham, “The Flow Pattern of a Supersonic Projectile” *Computations on Pure and Applied Mathematics*, vol. 5, pp.301–348,1970

- [8] R.T.Jones, "Theory of Wing-Body Drag at Supersonic Speeds," *NACA RM, A53H18a, 1953.*
- [9] A.R.George, "Reduction of Sonic Boom by Azimuthal Redistribution of Overpressure," AIAA Paper, 68-159.
- [10] H.W.Carlson, "An Investigation of the Influence of Lift on Sonic-Boom Intensity by Means of Wind-Tunnel Measurements of the Pressure Fields of Several Wing-Body Combinations at a Mach Number of 2.01," *NASA TN D-881, 1961*
- [11] H.W.Carlson, "Correlation of Sonic Boom Theory With Wind Tunnel and Flight Measurements," NASA TR R-213, 1964
- [12] H.W.Carlson, "Simplified Sonic Boom Prediction," *NASA Technical Paper, 1122, 1978.*
- [13] F.E.McLean, "Some Non-asymptotic Effects on the Sonic Boom of Large Airplanes," NASA Tn D-2877, June 1965.
- [14] L.B.Jones, "Lower Bounds for Sonic Bangs," *J. Roy. Aeron. Soc., 65, 4(1961).*
- [15] L.B.Jones, "Lower Bounds for Sonic Bang in the Far-field," *Aeron., Quart., XVIII, Pt. 1, 1-21 (1967).*
- [16] Hayes, Wallace D. "Linearized Supersonic Flow," PhD thesis, California Inst. of Technology, 1947
- [17] Hayes, Wallace D., "Sonic Boom Propagation in a Stratified Atmosphere, with Computer Program" NASA CR-1299, 1969
- [18] Hayes, Wallace D., "Brief Review of the Basic Theory," NASA SP-147, 1967, pp.3-7
- [19] Hayes, Wallace D., "Sonic Boom" *Annu. Rev. Fluid. Mech., Mar, 1971, pp.269-290*

- [20] Hayes, Wallace D., "Kinematic Wave Theory." Proc. Roy. Soc. London , 320:209-26
- [21] A.R. George and Kenneth J. Plotkin "Sonic Boom Waveforms and Amplitudes in a Real Atmosphere," *AIAA Journal*, , vol. 7, no. 10, Oct. 1969, pp. 1978-1981
- [22] K. J. Plotkin. Review of sonic boom theory. *AIAA paper 89-1105*, 12th AIAA Aeroacoustics Conference, San Antonio, TX, April 1989.
- [23] Kenneth J. Plotkin and J. M. Cantril "Prediction of Sonic Boom at a Focus " *AIAA paper*, 76-2, Jan., 1976
- [24] Kenneth J. Plotkin "Focus Boom Footprints for Various Air Force Supersonic Operations, " *WR 85-22*, Wyle Lab., Oct. 1985
- [25] Kenneth J. Plotkin, "Evaluation of a Sonic Boom Focal Zone Prediction Model" *WR 84-43*, Wyle Lab., Feb., 1985
- [26] Domenic J. Maglieri and Kenneth J. Plotkin "Aeroacoustics of Flight Vehicles, Theory and Practice," Vol. 1, pp. 519-561, Harvey H. Hubbard, Editor, Published in 1994
- [27] S.H. Cheung, "Application of CFD to Sonic Boom Near and Mid Field Prediction" *NASA TM 102867*, August 1990
- [28] S. H. Cheung and T. A. Edwards. Supersonic Airplane Design Optimization Method for Aerodynamic Performance and Low Sonic Boom. *In High-Speed Research Conference: Sonic Boom, Volume II*, February 1992, pp. 31-44.
- [29] M. Siclari and C.M. Darden, "An Euler Code Prediction of Near Field to Midfield Sonic Boom Pressure Signatures" *AIAA 90-4000-CP*
- [30] M. J. Siclari. Ground Signature Extrapolation of Three-Dimensional Near-Field CFD Predictions for Several HSCT Configurations. *In High-Speed Research Conference: Sonic Boom, Volume II*, February 1992, pp. 175-200.

- [31] M. Chan. *Supersonic Aircraft Optimization for Minimizing Drag and Sonic Boom*. PhD thesis, Stanford University, Stanford, CA 94305, 2003.
- [32] O.S.Rushov and G.M.Shefter “On the Energy of Acoustic Waves Propagating in a Moving Media” *App. Math. Mech.*, vol.26, no.5,1962,pp.1293-1309
- [33] D.I.Blokhintsev “Acoustics of a Nonhomogeneous Moving Medium” *NACA TM 1399, 1956*, Gostekhizdat, Moscow, U.S.S.R., 1946
- [34] Charles L. Thomas “Extrapolation of Sonic Boom Pressure Signatures by the Waveform Parameter Method” *NACA TN D-6832*, Washington, D. C. June, 1972
- [35] Charles L. Thomas “Extrapolation of Wind-Tunnel Sonic Boom Signature Without Use of a Whitham F-Function” *NASA SP-255*, 3rd conference on Sonic Boom Research, 1970
- [36] R.M.Hicks and J.P.Mendoza “Prediction of Aircraft Sonic Boom Characteristics From Experimental Near Field Results” *NACA TM X 1477*, 1967
- [37] Lomax, Harvard “The Wave Drag of Arbitrary Configurations in Linearized Flow as Determined by Areas and Forces in Oblique Planes,” *NACA RM A55A18*, 1955
- [38] Walkden, F. “The Shock Pattern of a Wing-Body Combination, Far From the Flight Path,” *Aeronaut. Q.*, vol. IX, pt.2, May 1958, pp. 164-194
- [39] Seebas, R. “Sonic Boom Theory,” *Journal of Aircraft*, vol. 6, no. 3, May-June 1969, pp. 177-184
- [40] R. Seebass and B. Argrow. Sonic boom minimization revisited. *AIAA Paper 98-295*, June 1998, 2nd AIAA Theoretical Fluid Mechanics Meeting, Albuquerque, NM
- [41] A.R.George, and R.Seebas, “Sonic Boom Minimization Including Both Front and Rear Shocks,” *AIAA J.*, 9, 2091-2093 (1971).

- [42] R.Seebass, and A.R.George, "Sonic-Boom Minimization," *J. Acoust. Soc. Am.*, 51, No.2 (pt.3), Feb. 1972, pp.686-694.
- [43] Yoshikazu Makino, "Near-field Inverse Design Using Gradient-Based Optimization with Continuous Adjoint Sensitivity Analysis," *CFD Journal*, Vol.12, 3:63 pp. 516-526
- [44] O.S.Ryzhov and G.M.Shefter, "On the Energy of Shock Waves Propagating in Moving Media," *Appl. Math. Mech.*, 26:1293-1309, 1962
- [45] A.R.George, "Lower Bounds for Sonic Booms in a Midfield," *AIAA J.*, 7, 1542 (1969).
- [46] J. Kang, "Nonlinear acoustic propagation of shock waves through the atmosphere with molecular relaxation," Ph.D thesis, Department of Mechanical Engineering, Pennsylvania State University, 1991
- [47] B.Lipkens and D.T.Blackstock "Model experiment to study sonic boom propagation through turbulence. Part II. Effect of turbulence intensity and propagation distance through turbulence" *J. Acoust. Soc. Am.*, 104(3 Pt 1):1301-9, Sep. 1998
- [48] H.Fletcher and W.Munson, "Loudness, its definition, measurement and calculation," *JASA*, 5(2), October 1993, pp. 82-108.
- [49] Allan D. Pierce, "Acoustics: An Introduction to Its Physical Principles and Applications" *Acoust. Soc. Am.*, New York, NY, 1989
- [50] K.E.Needleman, C.M.Darden, and R.J.Mack, "A Study of Loudness as a Metric for Sonic Boom Acceptability" *AIAA-1991-496*, Reno, NV, Jan., 1991
- [51] J. J. Alonso, I. M. Kroo and A. Jameson. "Advanced Algorithms for Design and Optimization of Quiet Supersonic Platforms," *AIAA Paper 02-0114*, 40th AIAA Aerospace Sciences Meeting and Exhibit, January 2002, Reno, NV.
- [52] H. S. Chung. *Multidisciplinary Design Optimization of Supersonic Business Jets Using Approximation Model-Based Genetic Algorithms*. PhD thesis, Stanford University, Stanford, CA 94305, 2004.

- [53] A. Jameson and D. Mavriplis, Finite Volume Solution of the Two-Dimensional Euler Equations on a Regular Triangular Mesh, *AIAA Journal*, Vol. 24, 1986, pp. 611-618
- [54] T. J. Baker. Mesh Adaptation Strategies for Problems in Fluid Dynamics. *Finite Elements in Analysis and Design*, Vol. 25, 1997, pp. 243-273.
- [55] M. A. Park. Adjoint-Based, Three-Dimensional Error Prediction and Grid Adaptation. *32nd Fluid Dynamics Conference*, June 24-27, 2002, St. Louis, MO
- [56] R. Lohner. Generation of Unstructured Grids Suitable for RANS Calculations *AIAA Paper 99-0662*, 1999
- [57] D. J. Mavriplis. Unstructured Mesh Generation and Adaptivity *ICASE 95-26*
- [58] J. Peraire, M. Mahdavi, K. Morgan and O. C. Zienkiewicz Adaptive Remeshing for Compressible Flow Computation *Journal of Computational physics*, 72:449-466 October, 1987
- [59] *Centaur System Users' Manual*, <http://www.centaursoft.com>
- [60] J. J. Alonso, J. R. R. A. Martins, J. J. Reuther, R. Haines, C. A. Crawford. *High-Fidelity Aero-Structural Design Using a Parametric CAD-Based Model*. *AIAA Paper 2003-3429*, 21st AIAA Applied Aerodynamics Conference. Orlando, FL. June 2003.
- [61] Curran A. Crawford, "An Integrated CAD Methodology Applied to Wind Turbine Optimization," Master thesis, Massachusetts Inst. of Technology, June 2003.
- [62] R. Haines CAPRI: Computational Analysis PRogramming Interface *Proceedings of the 6th International Conference on Numerical Grid Generation in Computational Field Simulations* July, 1998
- [63] R. Haines Automatic Generation of CFD-Ready Surface Triangulations from CAD Geometry *AIAA paper 99-0776*, 1999

- [64] L. Fornasier, H. Rieger, U. Tremel, E. Van der Weide. *Time Dependent Aeroelastic Simulation of Rapid Maneuvering Aircraft*. *AIAA Paper 02-0949*, 40th AIAA Aerospace Sciences Meeting and Exhibit, January 2002, Reno, NV.
- [65] A. Jameson, T. J. Baker and N. P. Weatherill. Calculation of Inviscid Transonic Flow over a Complete Aircraft. *AIAA Paper 86-0103*, 24th Aerospace Sciences Meeting, January 6-9, 1986, Reno, Nevada
- [66] A. Jameson and M. J. Berger, Automatic Adaptive Grid Refinement for the Euler Equations *AIAA journal*, Vol.23, 1985, pp. 561-568
- [67] A. Jameson, T. Baker, and T. Mitty, Generation and Adaptive Alteration of Unstructured Three-Dimensional Meshes *Third international Conference on Numerical Grid Generation in Computational Fluid Dynamics and Related Fields*, Barcelona, June 1991.
- [68] A. Jameson, T. Mitty, and T. Baker, Solution of Three-Dimensional Supersonic Flowfields via Adapting Unstructured Meshes *Fourth International Symposium on Computational Fluid Dynamics*, Davis, CA. Sept. 1991.
- [69] G. Warren, W. K. Anderson, J. L. Thomas and S. L. Krist Grid Convergence for Adaptive Methods *AIAA paper 91-1592*, June 1991
- [70] K. Plotkin, J. Page. *Extrapolation of Sonic Boom Signatures from CFD Solutions*. *AIAA Paper 02-0922*, 40th AIAA Aerospace Sciences Meeting and Exhibit, January 2002, Reno, NV.
- [71] Kenneth J. Plotkin "PCBoom3 Sonic Boom Prediction Model-Version 1.0e," *Wyle Research Report WR 95-22E*, October. 1998.
- [72] F. J. Wilcox. *Business Jet Sonic Boom Test - Unitary Plan Wind Tunnel Test 1870*. NASA Langley Research Center, February 2000.
- [73] Kenneth J. Plotkin "The effect of turbulence on the loudness of sonic boom" ASA 124th Meeting, New Orleans, 1992

- [74] K.J.Plotkin and A.R.George, "Propagation of Weak Shock Waves Through Turbulence," *Journal of Fluid Mechanics*, 54(3), 449-467,1972.
- [75] Allan D. Pierce, "Acoustics: An introduction to Its Physical Principles and Applications" *Acoustical Society of America*,, New York, NY, 1989
- [76] Joe Salamone, "Sonic Boom Simulation Using Conventional Audio Equipment," *NOISE-CON*, Baltimore, Maryland, July, 2004
- [77] C. M. Darden, E. D. Olson, E. W. Shields, "elements of NASA's High-Speed Research program," *AIAA Paper 93-2942*
- [78] N. M. Alexandrov, R. M. Lewis, C. R. Gumbert, L. L. Green, and P. A. Newman "Optimization with Variable-Fidelity Models Applied to Wing Design," *Accepted for Publication, AIAA Journal of Aircraft*
- [79] R.M.Lewis, "A Trust Region Framework for Managing Approximation Models in Engineering Optimization," *6th AIA/NASA/ISSMO Symposium on Multidisciplinary Analysis and Optimization*, September 1996, AIAA-96-4102
- [80] N. M. Alexandrov, R. M. Lewis, C. R. Gumbert, L. L. Green, and P. A. Newman "Optimization with Variable-Fidelity Models Applied to Wing Design," *Accepted for Publication, AIAA Journal of Aircraft*
- [81] S. E. Gano, V. M. Perez, J. E. Renaud, S. M. Batill "Multilevel Variable Fidelity Optimization of a Morphing Unmanned Aerial Vehicle," *45th AIAA/ASME/ASCE/AHS/ASC Structures, Structural Dynamics and Materials Conference*, AIAA 2004-1763 Palm Springs, CA, April 2004.
- [82] S.Burgee, A.A.Giunta, V.Balabanov, B.Grossman, W.H.Mason, R.Narducci, R.T.Haftka, and L.T.Watson, "A Coarse Grained Parallel Variable-Complexity Multidisciplinary Optimization Paradigm," *The international Journal of Supercomputing Applications and High Performance Computing*, 10 (1996), pp. 269-299
- [83] <http://desktopaero.com/products/PASSCatalogPage.html>.

- [84] <http://adg.stanford.edu/aa241/courseinfo.html>
- [85] Antoine, N., Kroo, I., Willcox, K., and Barter, G., "A Framework for Aircraft Conceptual Design and Environmental Performance Studies," *AIAA paper 2004-4314*, 10th AIAA/ISSMO Multidisciplinary Analysis and Optimization Conference, Albany, NY, Sep. 2004.
- [86] Nicolas E. Antoine, "Aircraft Optimization for Minimal Environmental Impact," Ph.D thesis, Department of Aeronautics and Astronautics, Stanford University, CA, 2004
- [87] A.A.Giunta, "Aircraft Multidisciplinary Design Optimization Using Design of Experiments Theory and Response Surface Modeling Methods," Ph.D thesis, Department of Aerospace and Ocean Engineering, Virginia Polytechnic Institute & State Univ., Blacksburg, Virginia, 1997.
- [88] J.Rodriguez, J.E.Renaud, and L.T.Watson, "Trust Region Augmented Lagrangian Methods for Sequential Response Surface Approximation and Optimization," *ASME Design Engineering Technical Conference*, September 14-17, Sacramento, CA.
- [89] S. Choi, J. J. Alonso and H. S. Chung "Design of a Low-Boom Supersonic Business Jet Using Evolutionary Algorithms and an Adaptive Unstructured Mesh Method," *45th AIAA/ASME/ASCE/AHS/ASC Structures, Structural Dynamics, and Materials Conference*, AIAA 2004-1758, Palm Springs, CA, April 2004.
- [90] S. Choi, J. J. Alonso and E. Weide. "Numerical and Mesh Resolution Requirements for Accurate Sonic Boom Prediction of Complete Aircraft Configurations". *AIAA Paper 2004-1060* 42nd AIAA Aerospace Sciences Meeting and Exhibit, Reno, Nevada, Jan 2004.
- [91] S. I. Choi, J. J. Alonso, I. M. Kroo, and M. Wintzer "Multi-fidelity Design Optimization of Low-boom Supersonic Business Jets," *10th AIAA/ISSMO Multidisciplinary Analysis and Optimization Conference*, AIAA 2004-4371 Albany, NY, September 2004.

- [92] H. S. Chung, S. Choi, J. J. Alonso, "Supersonic Business Jet Design Using Knowledge-based Genetic Algorithm with Adaptive, Unstructured Grid Methodology," *AIAA 2003-3791*, 21st Applied Aerodynamic Conference, Orlando, FL, June 2003.
- [93] H. S. Chung and J. J. Alonso "Multiobjective Optimization using Approximation Model-Based Genetic Algorithms," *10th AIAA/ISSMO Multidisciplinary Analysis and Optimization Conference*, AIAA 2004-4325 Albany, NY, September 2004.
- [94] J. Reuther and J. J. Alonso and A. Jameson and M. Rimlinger and D. Saunders "Constrained Multipoint Aerodynamic Shape Optimization Using an Adjoint Formulation and Parallel Computers: Part I," *Journal of Aircraft*, 36:51-60. 1999
- [95] J. Reuther and J. J. Alonso and A. Jameson and M. Rimlinger and D. Saunders "Constrained Multipoint Aerodynamic Shape Optimization Using an Adjoint Formulation and Parallel Computers: Part II," *Journal of Aircraft*, 36:61-74. 1999
- [96] A. Jameson "Aerodynamic Design via Control Theory," *Journal of Scientific Computing*, 3:233-260 1988
- [97] Nadarajah, S. K., Kim, S., Jameson, A., and Alonso, J. J. "Sonic Boom Reduction Using an Adjoint Method for Supersonic Transport Aircraft Configuration," *Symposium Transsonicum IV, International Union of Theoretical and Applied Mechanics*, September 2-6, 2002, DLR Gottingen, Germany
- [98] S. Nadarajah, A. Jameson, and J. J. Alonso. An adjoint method for the calculation of remote sensitivities in supersonic flow. *AIAA paper 2002-0261*, AIAA 40th Aerospace Sciences Meeting, Reno, NV, January 2002.
- [99] Carmichael, R.I., Erickson, L.I., "A Higher Order Panel Method for Predicting Subsonic or Supersonic Linear potential Flow about Arbitrary Configurations," *AIAA Paper 81-1255*, June 1981.

- [100] Ashley, H., Landahl, M. "Aerodynamics of Wings and Bodies", Dover, New York, republished 1985, p.104 and p.178
- [101] H. Chung and J. J. Alonso "Design of a Low-Boom Supersonic Business Jet Using Cokriging Approximation Models," *9th AIAA/ISSMO Symposium on Multidisciplinary Analysis and Optimization*, AIAA 2002-5598, Atlanta, GA, September 2002.
- [102] P.E.Gill, W.Murray, M.A.Saunders and M.H.Wright, "User's Guide for NPSOL(Versin 4.0): a Fortran package for nonlinear programming," *Report SOL 86-2*, Systems Optimizatin Laboratory, Stanford University, 1986 Atlanta, GA, September 2002.
- [103] P.E.Gill, W.Murray, M.A.Saunders and M.H.Wright, "Some theoretical properties of an augmented Lagrangian merit function, in P.M.Pardalos(ed.)," *Advances in Optimization and Parallel Computing*, North-Hollan, 101-128, 1992 Atlanta, GA, September 2002.
- [104] Thomas A. Zang and Lawrence L. Green. "Multidisciplinary Design Optimization Technique: Implications and Opportunities for Fluid Dynamics" *30th AIAA Fluid Dynamics Conference*, Norfolk, Virginia, AIAA 99-3798, June 1999
- [105] Jaroslaw Sobieszczanski-Sobieski and Raphael T. Haftka "Multidisciplinary Aerospace Design Optimization: Survey of Recent Developments," *34th AIAA Aerospace Sciences Meeting and Exhibit*, Reno, Nevada, AIAA 96-0711, January 1996.
- [106] J. Martin, J. J. Alonso and J. Reuther "High-Fidelity Aero-Structural Design Optimization of a Supersonic Business Jet," *43rd AIAA/ASME/ASCE/AHS/ASC Structures, Structural Dynamics, and Materials Conference*, AIAA 2002-1483, Denver, CO, April 2002.

- [107] J. Martin and J. J. Alonso "Complete Configuration Aero-Structural Optimization Using a Coupled Sensitivity Analysis Method," *9th AIAA/ISSMO Symposium on Multidisciplinary Analysis and Optimization*, AIAA 2002-5402 Atlanta, GA, September 2002.
- [108] Resit Unal, Roger A. Lepsch, Jr. and Mark L. McMillin "Response Surface Model Building and Multidisciplinary Optimization Using Overdetermined D-Optimal Designs," *7th AIAA/USAF/NASA/ISSMO Symposium on Multidisciplinary Analysis and Optimization*, AIAA 98-4759, September 1998
- [109] J. Sacks, W. J. Welch, T. J. Michell, and H. P. Wynn "Design and Analysis of Computer Experiments," *Statistical Science Vol 4. No.4*, pp. 409-453, 1989
- [110] Anthony A. Giunta and Layne T. Watson "A Comparison of Approximation Modeling Techniques: Polynomial Versus Interpolating Models," *7th AIAA/USAF/NASA/ISSMO Symposium on Multidisciplinary Analysis and Optimization*, St. Louis, Missouri, AIAA 98-4758, September 1998.
- [111] Timothy W. Simpson, Timothy M. Mauery, John J. Korte and Farrokh Mistree "Comparison of Response Surface and Kriging Models in the Multidisciplinary Design of an Aerospike Nozzle," *7th AIAA/USAF/NASA/ISSMO Symposium on Multidisciplinary Analysis and Optimization*, St. Louis, Missouri, AIAA 98-4755, September 1998
- [112] G.M.Robinson and A.J.Keane, "A case for Multi-Level Optimization in Aeronautical Design," *Aeronautical Journal, Vol.103, No. 028, 1999, pp.481-485*.
- [113] A. Ratle, "Kriging as a Surrogate Fitness Landscape in Evolutionary Optimization," *Artificial Intelligence for Engineering Design Analysis and Manufacturing*, Vol.15, No. 1, 2001, pp.37-49.
- [114] Y.Jin, M.Olhofer, and B.Sendhoff, "A Framework for Evolutionary Optimization with Approximate Fitness Functions," *IEEE Transactions on Evolutionary Computation*, Vol.6, No.5,2002,pp.481-494

- [115] K.H.Liang, X.Yao, and C.Newton, "Evolutionary Search of Approximated N-dimensional Landscape," *International Journal of Knowledge-Based Intelligent Engineering Systems* , Vol.4, No.3,2000,pp.172-183.
- [116] J.R.Koehler and A.B.Owen, "Computer experiments, in Design and analysis of experiments," *Handbook of Statistics*,, North-Holland Publishing Company, Amsterdam, 1996, pp.261-308
- [117] A.J.Booker, "DOE for computer output," *Tech. Report BCSTECH-94-052*, Boeing Computer Service, Research and Technology, M/S 7L-68, Seattle, Washington 98124, December 1994
- [118] C.T.Lawrence, and A.L.Tits, "A Computationally Efficient Feasible Sequential Quadratic Programming Algorithm," *SIAM Journal on Optimization* , Vol.11, No.4, 2001, pp.1092-1118
- [119] Y.S.Ong, P.B.Nair, and A.J.Keane, "Evolutionary Optimization of Computationally Expensive Problems via Surrogate Modeling," *AIAA Journal* , Vol.41, No.4, April 2003.
- [120] M.D.McKay, W.J.Conover, and R.J.Beckman, "A comparison of three methods for selecting values of input variables in the analysis of output from a computer code," *Technometrics*, 21 (1979), pp.239-245
- [121] M. D. Buhmann, "Radial Basis Functions," *Cambridge University Press*, 2003
- [122] M.Stein, "Large sample properties of simulations using Lating hypercube sampling," *Technometrics*, 29 (1987), pp.143-151
- [123] R.H.Myers, and D.C. Montgomery, "Response surface methodology: process and product optimization using design experiments," Wiley, New York, 1995
- [124] G.E.P.Box, and N.R.Draper, "Empirical model building and response surfaces," Wiley, New York, 1987

- [125] G.E.P.Box, W.G.Hunter, and J.S.Hunter, "Statistics for experiments: An introduction to design, data analysis, and model building," Wiley, New York, 1978
- [126] A.J.Booker, J.E.Dennis, A.D.Frank, D.B.Serafini, and V.Torczon, "A rigorous framework for optimization of expensive functions by surrogates," *NASA/CR-1998-208735*
- [127] D.B.Serafini, "A Framework for Managing Models in Nonlinear Optimization of Computationally Expensive Functions," Ph.D dissertation, Computational and Applied Mathematics Dept., Rice Univ., Houston, TX, Nov. 1998.
- [128] Ch. M. Bishop, "Neural Networks for pattern recognition," Oxford university press, 1995
- [129] S. Haykin, "Neural Networks: A Comprehensive Foundation," New York, Macmillan Publishing, 1994
- [130] G.H.Golub, and V.Pereyra, "The Differentiation of Pseudo-Inverse and Nonlinear Least Squares Problems Whose Variables Separate," *SIAM J.Numer.Anal.*10:413-432,1973.
- [131] G.H.Golub, and V.Pereyra, "Separable Nonlinear Least Squares: the Variable Projection Method and its Applications," *Inverse Problems* 19:R1-R26, 2003.
- [132] V.Pereyra, G.Scherer, and F.Wong, "Variable Projections Neural Network Training," *Applied Numerical Mathematics*, submitted, July, 2004
- [133] David E. Goldberg, "Genetic Algorithms in Search, Optimization, and Machine Learning," *Addison-Wesley*,1989.
- [134] N. Srinivas and K. Deb, "Multiobjective Optimization Using Nondominated Sorting in Genetic Algorithm," *Evolutionary Computation*,2(3):221-248, 1995.
- [135] K.Deb, S.Agarwal, A.Pratap, and T.Meyarivan "A Fast Elitist Non-Dominated Sorting Genetic Algorithm for Multi-Objective Optimization: NSGA II," *Parallel Problem Solving from Nature VI Conference*, pp.849-858, 2000

- [136] N. Marco and S. Lanteri, "Parallel Genetic Algorithms applied to Optimum Shape Design in Aeronautics," *Euro-Par'97 parallel Processing*, pages 856-863, Passau (Germany), Springer Verlag, 1997
- [137] J. J. Alonso, J. R. R. A. Martins, J. J. Reuther, R. Haimes, and C. A. Crawford "High-Fidelity Aero-Structural Design Using a Parametric CAD-Based Model," *16th AIAA Computational Fluid Dynamics Conference*, AIAA 2003-3429, Orlando, FL., 2003.
- [138] M. Chan, "A Coupled-Adjoint Method for High-Fidelity Aero-Structural Optimization," PhD thesis, Stanford University, Stanford, CA 94305, October 2002.
- [139] J. J. Alonso, P. LeGresley, E. van der Weide, J. J. R. R. Martins "pyMDO: A Framework for High-Fidelity Multi-Disciplinary Optimization," *10th AIAA/ISSMO Multidisciplinary Analysis and Optimization Conference*, AIAA 2004-4480 Albany, NY, September 2004.
- [140] A. Jameson "Advances in Aerodynamic Shape Optimization," *3rd International Conference on Computational Fluid Dynamics (ICCFD3)*, Toronto, Canada, July 12-16, 2004
- [141] J.A.Nelder and R.Mead "A Simplex Method for Function Minimization," *Computer Journal*, 1964, 7, 308-318
- [142] J. C. Lagarias, J. A. Reeds, M. H. Wright, and P. E. Wright "Convergence properties of the Nelder-Mead simplex method in low dimensions," *SIAM Journal on Optimization*, 9(1):112-147, 1998
- [143] K. I. M. McKinnon "Convergence of the Nelder-Mead simplex method to a nonstationary point," *SIAM Journal on Optimization*, 9(1):148-158, 1998
- [144] W. K. Anderson, J.C.Newman, D.L.whitfield, and E.J.Nielsen "Sensitivity analysis for Navier-Stokes equations on unstructured meshes using complex variables," *AIAA Journal*, 39(2001), no. 1, 56-63

- [145] C.G.Broyden, "The Convergence of a Class of Double-Rank Minimization Algorithm 2, The New Algorithm," *J. of the Inst. for Math. and Applications*,6:222-231, 1970
- [146] R.Fletcher "A New Approach to Variable-Metric Algorithms," *Computer Journal*, 13:317-322, 1970
- [147] D.Goldfarb, "A Family of Variable-Metric Algorithms Derived by Variational Means," *Mathematics of Computation*, 24:23-26,1970
- [148] D.F.Shanno, "Conditioning of Quasi-Newton Methods for Function Minimization," *Mathematics of Computation*, 24:647-656, 1970.
- [149] Charles Audet and J. E. Dennis, Jr "A Pattern Search Filter Method for Nonlinear Programming without Derivatives" *SIAM J. Optimization*, Vol. 14, No. 4, pp.980-1010, 2004
- [150] Charles Audet and J. E. Dennis, Jr "Mesh Adaptive Direct Search Algorithms for Constrained Optimization " *Journes de l'optimisation*, 2004
- [151] A. Jameson and J. J. Alonso "Automatic Aerodynamic Optimization on Distributed Memory Architectures" *AIAA Paper 96-0409*, 34th Aerospace Sciences Meeting, January, 1996, Reno, Nevada
- [152] A. Jameson and N. A. Pierce and L. Martinelli "Optimum Aerodynamic Design using the Navier Stokes Equation" *Theoretical and Computational Fluid Dynamics*, vol. 10, pp. 213-237, 1998.
- [153] Alison L.Marsden, "Aerodynamic Noise Control by Optimal Shape Design" Ph.D thesis, Stanford University, 2004
- [154] M. Abramson, C. Audet,J. Dennis, A.J.Booker, and E. Cramer "Optimization Using Surrogates for Engineering Design" West Coast Optimization Meeting, U. Washington, spring 2005.

- [155] Virginia Torczon, "On the Convergence of Pattern Search Algorithms" *SIAM J. Optimization*, Vol. 7, No. 1, pp.1-25, Feb. 1997
- [156] Clarke, F.H. "Optimization and Nonsmooth Analysis" *SIAM Classics in Applied Mathematics*, Vol. 5, Philadelphia
- [157] S. E. Cliff, and S. D. Thomas. Euler/experiment correlations of sonic boom pressure signatures. *AIAA Paper 91-3276*, September 1991.
- [158] Hamies, R. and Follen, G. "Computational Analysis Programming Interface," *Proceedings of the 6th International Conference on Numerical Grid Generation in Computational Field Simulations*, Greenwich, 1998
- [159] National Research Council, High Speed Research Aeronautics and Space Engineering Board *U.S. Supersonic Commercial Aircraft : Assessing NASA's High Speed Research Program* , National Academy Press, Washington, D.C., 1997.
- [160] National Research Council, High Speed Research Aeronautics and Space Engineering Board *Commercial Supersonic Technology : The Way Ahead* , National Academy Press, Washington, D.C., 2002.
- [161] D. Aronstein and K. Schueler "Conceptual Design of a Sonic Boom Constrained Supersonic Business Aircraft," *42nd AIAA Aerospace Sciences Meeting and Exhibit, Reno, Nevada, Jan 2004*, AIAA 2004-0697, Reno, NV, January 2004.
- [162] M.J.Lighthill "Supersonic Flow Past Bodies of Revolution," *Aeronautical Research Commission, Reports and Memoranda* London, No. 2003, 1945
- [163] Thomas, Charles L. "Extrapolation of Wind-Tunnel Sonic Boom Signatures without Use of a Whitham F-function" *NASA SP-255*, pp.205-217, 1970